Molecular Dynamics Simulations of Material Damping and Nonlinear Oscillations in Nanoresonators

Sankha Mukherjee

Department of Mechanical Engineering

McGill University

Montreal, Quebec

January 2016

A thesis submitted to McGill University in partial fulfillment of the requirements for the degree of Doctor of Philosophy

Dedicated to my parents and my wife.

Acknowledgements

I am grateful to Professor Srikar Vengallatore and Professor Jun Song for their support, constant encouragement and focused feedback over the course of last five years. I want to thank them for persuading me into doing molecular dynamics simulations and thus opening an entirely new interesting world for me.

I had the good fortune of collaborating with many talented researchers. I would like to thank Dr. Zahra Nourmohammadi and Ms. Surabhi Joshi for collaborating on various parts of this thesis. I would like to acknowledge the technical assistance received from Dr. Bryan Caron and Dr. Dan Mazur from CLUMEQ supercomputer center.

I would also like to thank past and future students in our research group for their support and all the invigorating discussions. Thank you Guru Prasad Sosale, Kaushik Das, Dorothée Almecija, Denten Neill, Lacey-Lynne Lemaire, Sherman Hung, Ottoleo Kuter-Arnebeck, and Nabil Salabhi. Special thanks to Santosh Nannuru, Sandip Barui, Tapabrata Mukherjee, Saikat Chatterjee, Bikram Konar, Sayani Seal, Arpita Mitra, Amrita Bag, Gogol Ghosal, Tuhin Das, and Rohan Chakrobarty for their friendship, and for making me feel at home.

Special thanks to Santosh Nannuru and Kaushik Das for carefully proof-reading this document. Thanks to Charles Trudeau for helping me write the abstract in French.

Finally, I would like to thank my father (Mr. Dhruba Mukherjee), my mother (Mrs. Mridula Mukherjee) and my loving wife (Mrs. Debika Banerjee) for their unconditional support, endless love and selfless sacrifices.

Abstract

Nanomechanical resonators are tiny, operate at very high frequencies (in the GHz regime), and are ultrasensitive; recent measurements show that these structures can measure mass and force at the atomic level. The sensitivity of these devices can be further improved by reducing damping and enhancing the linear range. Difficulties in studying damping and dynamics in nanoresonators using experiments arise from their small size and the simultaneous existence of several mechanisms. As a result, despite of a lot of research activity a detailed microscopic understanding of the mechanisms of material damping and nonlinear oscillations has not been achieved. To address some of these problems, we use classical molecular dynamics to study damping and nonlinear dynamics in a set of nanoresonators made of nickel and silicon atoms with dimensions in the range of nanometers.

In the last decade several attempts have been made for estimating damping in nanostructures using adiabatic molecular dynamics simulation in which the temperature of the system is not controlled. On the other hand, isothermal simulations are more meaningful for damping simulations because they mimic the operating conditions of actual devices. To bridge this gap, we performed isothermal simulations of damping using Nosé-Hoover thermostat in a nickel nanofilm undergoing longitudinal oscillations at 300 K and established the relationship between different measures of damping and the dynamics. In the subresonant regime, damping was quantified as the loss tangent and the loss factor using steady-state harmonic oscillations and their magnitudes were found to differ by less than 3%. We identified simulation parameters needed to be selected to ensure linearity and convergence. The quality factor was obtained from the spectrum of the

thermomechanical noise and also from the Duffing-like nonlinearity during steady-state harmonic oscillations. In addition, the nonlinear logarithmic decrement was obtained from the Hilbert transform.

Damping in a single-crystal silicon nanofilm and a single-crystal silicon nanowire was simulated to measure loss angle and loss factor for longitudinal oscillations as a function of frequency and temperature. The results of this study showed damping peaks around 300 K and 500 K in the nanofilm which had qualitative resemblance with Akheiser damping. In addition, damping in the nanowire was larger than in the nanofilm at 300 K because of comparatively larger surface to volume ratio. In another study, damping in amorphous silicon was found to be orders of magnitude larger than in single-crystal silicon for longitudinal oscillations. In addition, temperature dependent peaks were observed in the damping of the amorphous silicon.

In the last chapter, nonlinear oscillations is explored for the fundamental bending mode of two doubly-clamped beams (one with square and the other with rectangular cross-section) and the longitudinal mode of a silicon nanofilm. The doubly-clamped beam with rectangular cross-section showed spring hardening behavior in the steady-state harmonic response while the nanofilm showed spring softening behavior. In both cases the response could be captured using the Duffing equation. The doubly-clamped beam with square cross-section showed signatures of 1:1 internal resonance consistent with the theory of two-degree-of-freedom Duffing system with cubic coupled terms.

Sommaire

Les résonateurs nanomécaniques sont des dispositifs minuscules, ultrasensible et fonctionnent à des fréquences très élevées (GHz); des mesures récentes montrent que ces structures peuvent mesurer des masses et des forces au niveau atomique. La sensibilité de ces dispositifs peut être encore améliorée en réduisant l'amortissement et avec l'amélioration de l'intervalle linéaire. L'étude de l'amortissement et des forces dynamiques trouvées a l'intérieure des nanorésonateurs apportent des difficultés qui découlent principalement de leur petite taille. En conséquence, en dépit du grand nombre d'activités de recherche, une compréhension microscopique détaillée des mécanismes d'amortissement et d'oscillations non linéaires n'a pas encore été atteint. Pour répondre à certains de ces problèmes, nous utilisons la dynamique moléculaire classique pour étudier l'amortissement et la dynamique non linéaire dans un ensemble de nano résonateurs faite a partir de nickel et de silicium avec des dimensions de l'ordre de nanomètres.

Dans la dernière décennie, plusieurs tentatives ont été faites pour simuler un amortissement a l'intérieur de nanostructures a l'aide de simulations adiabatiques, dans lesquels la température du système est non contrôlée. De l'autre part, les simulations isothermes sont plus significatives pour les simulations d'amortissement parce qu'ils imitent les conditions de fonctionnement des dispositifs réels. Pour combler cette lacune, nous avons effectué des simulations isothermes d'amortissement utilisant un thermostat Nosé-Hoover dans un nanofilm de nickel subissant des oscillations longitudinales à 300 K et nous avons établi la relation entre les différentes mesures d'amortissement et de la dynamique. Dans le régime sous-résonant, l'amortissement a été quantifiée comme étant la perte tangente et le facteur de perte en utilisant l'état d'équilibre

d'oscillations harmoniques et une différence inférieure à 3% de leurs amplitudes a été trouver. Nous avons identifié les paramètres de simulation nécessaires pour assurer la linéarité et la convergence. Le facteur de qualité a été obtenu à partir du spectre de bruit thermomécanique et aussi de l'aspect non-linéarité Duffing pendant l'état d'équilibre d'oscillations harmoniques. De plus, le décrément logarithmique non linéaire a été obtenue à partir de la Transformée de Hilbert.

L'amortissement dans un nanofilm et nanofil de silicium monocristallin a été simulée pour mesurer l'angle de perte et le facteur de perte pour des oscillations longitudinales en fonction de la fréquence et température. Les résultats de cette étude ont montré des pics d'amortissement a des températures d'environ 300 K et 500 K dans le nanofilm qui avait une ressemblance qualitative avec un amortissement Akheiser. L'amortissement à 300K dans le nanofil était plus grand que dans le nanofilm en raison d'un rapport surface/volume plus grand. Dans une autre étude, l'amortissement dans le silicium amorphe a été trouvé comme étant plusieurs ordres de magnitude plus grande que dans le silicium monocristallin pour les oscillations longitudinales. De plus, des pics dépendant de la température ont été observés dans l'amortissement du silicium amorphe.

Dans le dernier chapitre, les oscillations non linéaires sont explorées pour le mode de flexion fondamental de deux poutres doublement encastrées (une avec une coupe transversale carré l'autre rectangulaire) et le mode longitudinal d'un nanofilm de silicium. La poutre rectangulaire doublement serrée présente un comportement de durcissement de ressort dans la réponse harmonique en régime permanent tandis que le nanofilm montre un comportement d'amortissement. Dans les deux cas, la réponse pourrait être capturée à l'aide de l'équation Duffing. La poutre carrée doublement serrée montre une signatures 1:1 de résonance interne, qui est

conforme à la théorie Duffing de système a deux-degrés-de-liberté avec des termes couplés cubiquement.

Abbreviations

ART	Activation-relaxation
BTE	Boltzmann transport equation
CRN	Continuous random network
EAM	Embedded atom method
FDT	Fluctuation dissipation theorem
FFT	Fast Fourier transform
KE	Kinetic energy
LAMMPS	Large-scale atomic/molecular massively parallel simulator
MD	Molecular dynamics
MPI	Message passing interface
NEMS	Nano electro mechanical system
NPH	Number of atoms (N), pressure (P) and enthalpy (H)
NPT	Number of atoms (N), pressure (P) and temperature (T)
NVE	Number of atoms (N), volume (V) and energy (E)
NVT	Number of atoms (N), volume (V) and temperature (T)
PBC	Periodic boundary condition
PSD	Power spectral density
RDF	Radial distribution function
SDOF	Single degree of freedom

SW	Stillinger-Weber
TAR	Thermally activated relaxation
TED	Thermoelastic damping
TLS	Two level system
NH	Nosé-Hoover
rms	Root mean square

Latin Symbols

A	Amplitude of vibration
A_c	Critical amplitude
A_p	Peak amplitude
a-Si	Amorphous silicon
C	Specific heat per unit volume
c	Coefficient of viscous damping
c-Si	Crystalline silicon
E	Young's modulus
F_0	Force applied on the mass
f	Frequency of oscillation
f_n	Resonance frequency
$g(r)$	Radial distribution function

H	Hamiltonian function
k_B	Boltzmann's constant
k	Thermal conductivity
K_x	Axial stiffness
L	Length of the beam
d_f	Number of internal degrees of freedom
Ni	Nickel
P	Probability distribution function
Q	Quality factor
S	Cross-section
Si	Silicon
SiC	Silicon carbide
CNT	Carbon nanotube
SWCNT	Single walled carbon nanotube
DWCNT	Double walled carbon nanotube
Si_3N_4	Silicon nitride
S_x	Power spectral density of axial displacement noise
t_f	Duration of forced vibration
t_c	Convergence time
U	Embedded atomic potential
W	Total mechanical energy stored in a vibrating structure during each cycle of vibration

x	Displacement
s	Phonon wave vector polarization
$\vec{u}$	Phonon wave vector
v	Phonon wave velocity
F_e	Force field
V_{nr}	Velocity of the nanoresonator
t_{raise}	Simulation time for raising the temperature of the structure in NVT ensemble
t_{eq}	Simulation time for thermal equilibration
G	Equivalent mass of Nosé-Hoover thermostat

Greek Symbols

δ	Logarithmic decrement
Δt	Simulation time step
ΔW	Energy dissipated per cycle of vibration
ϕ	Phase angle
$\phi(t)$	Instantaneous phase signal
η	Loss factor
σ_Q	Standard deviation of Quality factor
$\overline{\sigma}$	Normalized detuning parameter

τ_{NH}	Time constant for the Nosé-Hoover thermostat
τ_p	Phonon-relaxation time
τ_v	Period of mechanical vibration
ω_d	Damped angular resonance frequency
ω_n	Undamped angular resonance frequency
$\tilde{y}(t)$	Hilbert transform of $y(t)$
Θ	Frictional parameter for the Nosé-Hoover thermostat

Table of contents

List of Tables

List of Figures

Chapter 1

Introduction to nanoresonators

Recent advances in microfabrication techniques have enabled manufacturing of resonators with structural dimensions on the order of hundreds of nanometers, these devices are popularly known as nanoresonators. Nanoresonators are mechanical structures such as beams [1], plates [2], membranes [3], wires [4], and discs [5] and are harmonically excited in one of their resonant modes. Depending on the direction of vibration, these structures operate in different mechanical modes, for example flexural [6], longitudinal [7], torsional [8], lamé [9], contour [10], and breathing [11]. Common choice of materials for manufacturing nanoresonators include carbon nanotubes (CNT) [12, 13], graphene [14, 15], single-crystal silicon [16], SiC [17] and Si_3N_4 [18].

Nanoresonators have extraordinary performance capabilities, these devices have natural frequencies in the microwave frequency range [19], making them useful in diverse array of applications such as sensing, detection, and filtering. Carefully designed experimental setups using nanoresonators have been demonstrated to have mass sensitivity to the attogram (10^{-18} g) level at room temperature [20], and yoctogram (10^{-24} g) sensitivity at cryogenic temperatures [21]. These results serve as an inspiration to build spectrometers capable of imaging spatial distribution of mass within individual analyte using nanoresonating structures in a lab-on-a-chip [22, 23]. In addition, these devices are also capable of measuring forces as small as 10^{-19} N [24] and fluctuations on the order of 10^{-12} meters [25] at room temperature.

Applications of nanoresonators in biosensing include detection of biological entities such as viruses [26], marker proteins [27], DNA [28], and enzymatic activity [29]. Furthermore, nanoresonator based experimental setups have been used for exploring applications in quantum-enhanced sensing and quantum information. For example, beam-nanoresonators combined with magnetic resonance imaging have been demonstrated to capture the spin of a single electron [25, 30]. Also, recently researchers have been able to cool nanoresonators down to their quantum mechanical ground state to show macroscopic mechanical objects can obey laws of quantum mechanics [31, 32]. In addition, the use of carbon nanotube and graphene based resonators as switches [33, 34], transmitters [35], filters [36] is actively being pursued for applications in radio-frequency (RF) communication.

As nanoresonators evolve and gain maturity, there is a growing need for developing systematic and rational design methodologies for improving their performance and to make transition from laboratory scale experimental demonstrations to full-fledged commercialization. Two critical operating aspects that determine the performance of resonators in general are damping in the structure and the linearity of oscillations. Section 1.2 and 1.3 discusses the role of damping and nonlinear oscillations in the context of performance of nanoresonators.

1.1 Damping

Mechanical structures dissipate stored energy during vibrations by damping. In general damping is measured in terms of quality factor (Q-factor), logarithmic decrement (δ), loss factor (η), loss angle (ϕ), and loss tangent ($\tan\phi$). For small values of damping ($\phi < 0.01$) these measures are related [37]

$$\frac{1}{\eta} = \frac{1}{\phi} = \frac{1}{\tan\phi} = \frac{\pi}{\delta} = Q \tag{1.1}$$

(This relationship is essential to the damping estimates reported in this thesis, expressions for calculating each of these measures have been discussed in Chapter 2.)

Reducing damping in nanoresonators is important for the following reasons: (a) enhancing sensitivity in sensing applications, (b) improving frequency stability and selectivity in communications applications, and (c) reducing the power consumption of devices used in RF and IC applications. For example the mass sensitivity of nanoresonators is given by [38]

$$\Delta m \approx 2m_0 \left(\frac{\Delta f}{2\pi Q f_0} \right)^{\frac{1}{2}} 10^{-\frac{DR}{20}} \tag{1.2}$$

where m_0 is the mass, f_0 is the natural frequency, DR is the dynamic range of the resonator, Δf is the available frequency range of detection. The dynamic range is defined as the ratio of the maximum amplitude at the onset of nonlinear oscillations and the thermomechanical noise floor. An outcome of Eq. (1.2) is that the sensitivity of a given resonator, i.e. the smallest mass that a resonator can detect for fixed values of m_0, f_0, and Δf increases by reducing damping in the resonator. Therefore reducing damping in nanoresonators is warranted to be able to detect smaller mass.

Damping arises from various sources depending on the operational parameters (frequency, temperature, crystallographic defect, mode, amplitude, chemistry). The mechanisms responsible for damping are broadly classified into material damping and extrinsic damping [39]. Examples of extrinsic damping mechanisms are: support loss resulting from the stress-wave radiation at the

supports, clamping loss due to stick-slip friction at the clamps, and fluid damping due to the frictional forces exerted on the resonator by the surrounding fluid [39]. Material damping mechanisms originate in the resonator itself, these are thermoelastic damping, phonon damping, surface-medicated damping, and internal friction. Details of different material damping mechanisms relevant to the results presented in this thesis are presented in Chapter 2. Progress has been made in developing design strategies to reduce damping from extrinsic mechanisms to insignificant values, for example, operating a resonator in vacuum can reduce fluid damping to negligible values [40]. However, material damping mechanisms are unavoidable, therefore, it is imperative to understand the material damping mechanisms in detail for designing nanoresonators with low damping.

Over the years considerable effort has gone into developing experimental and theoretical strategies for understanding different material damping mechanisms [39, 40]. Studying a particular mechanism using experiments is difficult because the measured damping has contributions from all the damping sources and the identification of contributions from each of the damping sources is not trivial [41]. Furthermore, experimental uncertainties and calibration limitations also influence accuracy of the measurements [42]. In addition, difficulty arises in the measurement of damping in nanoresonators because of: (a) fragility of the intricate architectures, and (b) unavailability of suitable transduction schemes for the measurement of high frequency of oscillations.

On the other hand, in the past century, several phenomenological theoretical models have been formulated to model damping. These are: viscous damping [37], Kimball-Lovell solid [43], and anelastic solid [44, 45]. A limitation of these models is that they incorporate damping in the

equations of motion using ad-hoc assumptions about the governing mechanisms, and do not take into consideration the specifics of the underlying mechanisms. Therefore, despite of considerable efforts, a detailed atomic level understanding of energy dissipation in solids is still elusive.

1.2 Nonlinear oscillations

The motion of linear resonators can be described using the model of harmonic oscillator as long as the restoring force is proportional to the displacement from the equilibrium position [46]. But, this linear assumption does not hold in the nonlinear regime [47]. Recent research shows that the linear regime in nanoresonators is limited because these structures are prone to nonlinear oscillations when excited near the resonance frequencies [48, 49]. This limits the useful dynamic range in nanoresonators.

Unlike linear systems, resonance frequencies in nonlinear systems are amplitude dependent, and for deterministic harmonic excitations their responses can be inconsistent. In continuous systems these irregularities give rise to interesting phenomena such as jump, bifurcations, and modal coupling [50]. For example, in linear multi-degree-of-freedom systems different mechanical modes are independent of each other, therefore it is possible to excite a particular mode without perturbing other resonant modes. However, in nonlinear systems mechanical modes can couple, interact and exchange energy when excited [1, 51-53]. There are practical purposes for which designers want to avoid or control bifurcations, and modal coupling in nanoresonators. Therefore, there is a growing need to study nonlinear oscillations, understand the key mechanisms, develop mathematical models, in order to identify conditions to avoid it when unwanted, and explore it efficiently to open up future possibilities.

In general nonlinearities in mechanical structures can arise from various sources. In nanoresonators these mechanisms can be broadly categorized as material, inertial, geometric and dissipative [54]. For small magnitudes of applied stress the strain in the system is usually proportional. However, for large applied stress the linear relationship between the stress and the strain becomes invalid, this condition is known as material or constitutive nonlinearity. Geometric nonlinearities arise at large oscillation amplitudes giving rise to nonlinear strain-displacement relationships (such as mid-plane stretching, large curvature, and large strain). A concentrated or distributed mass leads to nonlinear velocities/accelerations in the dynamics of resonators known as inertiaI nonlinearity. Mechanisms of dissipative nonlinearity are unclear [55, 56].

Efforts have been made for modelling nonlinear oscillations theoretically by making assumptions about the governing dynamics, and approximating the problem with an equivalent nonlinear system [50, 54]. In the absence of generic principles for the analytical modelling of nonlinear oscillations in nanoresonators, attempts have been made mostly on a case by case basis. For example the Duffing equation for long has served as an important paradigm for a broad class of nonlinear phenomena. The basic assumption of the Duffing model is a cubic restoration force in the equation of motion [47, 50]. This simplifying assumption has been found to capture the nonlinearity of oscillations in several nanoresonators reasonably well [48, 53, 57]. However a blanket use of the Duffing nonlinearity can be grossly incorrect essentially because new phenomena can occur at the nanoscale that can significantly alter the response. For example, the thermal noise is an important aspect in the dynamics of nanoscale resonators. It has been recently shown that the thermal noise itself can drive nanoresonators into nonlinear regimes [58]. However, there have been fewer attempts made to account for this effect into the mathematical treatment of

the nonlinear dynamics [13]. Studying nonlinear dynamics using experiments is also difficult because several mechanisms simultaneously contribute to the observed nonlinearity, making it difficult to identify the underlying mechanisms.

1.3 Use of molecular dynamics simulations

A different approach for studying damping and dynamics in nanoresonators is to tackle the problem from a microscopic point of view. A significant recent progress in this regard is the use of molecular dynamics (MD) simulations. In classical MD simulations atoms are treated as point particles and their motions are tracked by performing numerical computations over long sequence of time steps. Typically MD simulations are performed for systems with $10^2 – 10^9$ atoms [59], over times to the tune of nanoseconds [60]; these numbers match suitably with nanoresonators because of their tiny mass and small period of oscillations (to the tune of nanoseconds).

In general, the following steps are performed in order to perform MD simulations. The first step is to find a potential function, commonly known as the interatomic potential, which describes the mutual interactions between atoms. The potential function is either approximated by an empirical force model, or is fitted using electronic structure calculation data. The second step is to formulate an algorithm for integrating the equations of motion numerically to calculate atomic positions, velocities and forces. The final step is to specify the initial conditions (for example initial atomic positions, velocities) and feed them to the integration scheme for solving the equations of motion. The details of the different aspects of MD simulations are presented in Chapter 3.

In MD simulations, the system is evolved in time under certain macroscopic constraints, and there are infinite number of microstates (microstates are particular configurations of the system with a

given set of positions and momenta) compatible with the imposed constraints. In the context of statistical mechanics ensembles are defined as an assemblage of these microstates, each of which represent a possible macroscopic constraint that the real system experiences. MD simulations are used to estimate the material and structural properties by invoking *ergodicity* which states that given sufficient time a system will attain all possible positions and momentum consistent with the imposed macroscopic conditions [61], in other words, time averages are equal to ensemble averages. This consideration allows the prediction of structural, dynamic and thermodynamic properties using limited computational resources. Typically, the time evolution of a single ensemble is simulated to characterize the system. There are several commonly used ensembles in molecular dynamics simulations, e.g. microcanonical NVE ensemble, in which number of atoms (N), volume (V) and energy remains constant (E); canonical NVT ensemble (NVT) in which number of atoms, volume, and temperature (T) remain unchanged; isothermal-isobaric NPT ensemble in which number of atoms, pressure and temperature (T) is kept constant; and isoenthalpic-isobaric NPH ensemble in which number of atoms, pressure and enthalpy (H) remain statistically invariant.

Using MD simulations researchers have studied different mechanisms of material damping in idealized nanoresonators by eliminating extrinsic damping mechanisms. For example, instead of using an external substrate, clamping conditions have been achieved by freezing motion of few atoms in the structure, thereby eliminating attachment losses [62]. Energy dissipation due to fluid damping has been eliminated by performing simulations with the nanoresonators surrounded by vacuum [63]. The next section presents an exhaustive survey of the literature on material damping and nonlinear oscillations in nanoresonators investigated using MD. The aim is to organize results

from various studies and identify gaps in the knowledge. Subsequently, Section 1.7 outlines the organization of the thesis.

1.4 Literature survey

Till date a small set of materials have been used to study material damping and nonlinear oscillations in nanoresonators. A summary of the range of materials, structural dimensions, vibrational modes, frequency and temperature is presented in Table 1.1. In these studies the simulations have been performed using the NVE and the NVT ensemble.

Table 1.1: Summary of materials and operating parameters for MD simulations.

Materials	Graphene [64-74], Carbon nanotubes [63, 75-80], Silicon [81], Silver [82], Copper [82-84], and Nickel [62, 85]
Structural dimensions	4 nm to 50 nm
Frequency	3 GHz to 1.2 THz
Temperature	0.05 K to 1200 K
Method used for calculating damping	Free decay, loss angle, loss factor
Mode of oscillation	Bending, longitudinal, torsional

- *Damping in CNTs*: Guo *et al.* [79] studied the effect of morphology of carbon nanotubes (CNT) on damping using the free decay method and found that commensurate (armchair/armchair or zigzag/zigzag) CNTs damp more compared to the incommensurate (armchair/zigzag) CNTs. Similar results on damping were obtained for SWCNTs and DWCNTS by Akita *et al.* [78]. Jiang

et al. [63] simulated damping in CNTs using the free decay method, they used the following expression for calculating the Q-factor,

$$E_n = E_{ext}(1-2\pi/Q)^n, \tag{1.3}$$

where E_n is the total energy after n cycles and E_{ext} is the initial energy. Their calculations revealed that the DWCNTs (double walled carbon nanotube) dissipate more energy compared to SWCNTS (single walled carbon nanotube). The excess dissipation was attributed to interlayer interaction present in DWCNTs. Further analysis revealed that the damping in the SWCNT varied with temperature showing $T^{0.36}$ dependence.

Vallabhaneni *et al.* [75, 76] modified the free decay method and used a band pass filter based approach to remove the thermal noise from the overall response for calculating damping in SWCNTs. They reported that Q-factor in SWCNTs was independent of the length and the diameter for longitudinal vibrations, but increased with increasing length and decreased with increasing diameter for the bending vibrations. In addition, damping was found to increase linearly at temperature below 300 K [76], contrary to the trend of $T^{0.36}$ reported by Jiang *et al.* [63]. Vallabhaneni *et al.* concluded that the discrepancy in the temperature dependence of damping in CNT was due to an error in the method for calculating damping used by Jiang *et al.* wherein the authors did not separate the external and internal energies in Eq. (1.3) which lead to an over estimation of Q-factors.

Zhou *et al.* [80] calculated damping in SWCNTS and DWCNTs in terms of ϕ and observed that damping is inversely related to the tube radius. In addition, significant increase in damping was

reported at frequencies in the vicinity of the resonance frequency. The excess energy dissipation close to the resonance frequency was attributed to the excitation of additional phonon modes.

- *Damping in graphene membranes*: In a series of papers, Kim *et al.* [69] reported that for flexural mode oscillations in the absence of extrinsic damping mechanisms Q-factor in graphene membranes is limited. In addition, they investigated into the effect of edge effects and grain boundaries on damping and observed that without the application of any external stress, additional vibrational modes appear because of free edges and contribute to the energy loss in graphene [70, 72]. Passivating the free edges with hydrogen atoms was found to be ineffective in reducing the damping, whereas externally applied strain of 1% reduced damping as a function of temperature below 300 K. Similar results related to the edge effects on damping in graphene membranes have been reported by Jiang *et al.* [66, 67]. Kim *et al.* [72] found that damping in graphene with grain boundaries is orders of magnitude larger than its pristine counterpart.

- *Damping in MoS_2 membranes*: MD simulations of damping in single layered MoS_2 membranes revealed that material damping in MoS_2 is smaller than in graphene at temperatures below 300 K [86]. The reduction in damping was attributed to the energy gap in its phonon dispersion, which helps to prevent the resonant oscillation from being interrupted by other vibrational modes. This study also demonstrated that nonlinear oscillations lead to larger damping in MoS_2 compared to graphene due to the existence of additional ripples in MoS_2.

- *Damping in ZnO nanowires*: Jiang *et al.* [87] simulated damping in ZnO nanowires with: (a) reduced surface charges on the polar surfaces, and (b) free polar surfaces. They reported that damping in ZnO with free polar surface is one order of magnitude smaller than the structure with

reduced surface charges. Further analysis revealed that low damping is due to shell like surface reconstruction in the free polar surface that prevents the resonant oscillations in the free nanowires from being dissipated through the torsional motion.

- *Damping in Ag nanowires*: The effect of tensile strain on the damping in Ag nanowires was studied by Kim and Park [71]. They reported that the application of tensile strain effectively mitigates both the intrinsic surface and thermal losses, with improvements in Q-factor by a factor of 3–10 across a range of operating temperatures. In addition, the damping was found to be independent of the surface area to volume ratio, but varied with the aspect ratios. Furthermore, irrespective of the applied strain the damping showed a $T^{0.7}$ dependence.

- *Damping in $Si_xGe_{1\_x}$ and $Si/Si_xGe_{1\_x}$ nanowires*: Georgakaki *et al.* [81] investigated damping in doubly-clamped $Si_xGe_{1\_x}$ and $Si/Si_xGe_{1\_x}$ nanowires from free oscillations. The atomic interactions were calculated using the Tersoff potential [88]. They found that Q-factor in all the structures were to the tune of 10^3 at 300 K at frequencies in the range 180 GHz and 260 GHz. In addition, below 300 K the Q-factor was found to follow power law ($Q \sim T^{-\Gamma}$, $0.7<\Gamma<1$), with the composite structures $Si_{0.5}Ge_{0.5}$ and $Si/Si_{0.5}Ge_{0.5}$ exhibiting higher Q-factor than pristine Si at 300 K. Furthermore, a passivation of the free surfaces with atomic hydrogen enhanced the Q-factor from 10^4 to 10^5 at 23 K. The authors however did not explicitly identify the dominant mechanism responsible for the observed damping.

During the oscillations of a damped resonator the stored mechanical energy is converted into heat. Under isothermal conditions the heat energy is dissipated into the environment and the resonator

maintains its initial temperature. However, in NVE ensemble the energy of the structure is kept constant, this condition prohibits energy exchange between the structure and any heat reservoir. Under such conditions a constant increase of temperature in the structure is inevitable.

- *Damping in nickel nanofilm and graphene nanoribbon*: The damping results discussed above were obtained by evolving the resonators in NVE ensemble. Recently Kunal and Aluru [62, 73, 74, 85] have introduced a method for MD simulations of damping in nanoresonators under isothermal conditions using the canonical NVT ensemble. In this method, the resonator is made to undergo harmonic oscillations and the velocity and the displacement of the structure is recorded. The dissipation in the structure is estimated using the loss factor (η). Kunal *et al.* calculated frequency dependent damping in nickel nanoresonators and nanoribbons. Their analysis revealed phonon mediated damping to be the dominant source of energy dissipation in nickel nanoresonators and graphene nanoribbons.

- *Nonlinear oscillations in CNT and graphene nanoresonators*: Recently Koh *et al.* [89] studied the thermal fluctuation induced nonlinear oscillations in cantilevered and suspended SWNTs and observed spectral broadening and multiple peaks in the frequency spectra. From Poincaré maps of SWNT tip trajectories, they detected repeated occurrence of planar and nonplanar (whirling) motion. Koh *et al.* proposed approximate solutions of nonlinear beam equations which were able to capture the alternation of the patterns of motion in both the structures reasonably well. By using this analytical approach, they found that multiple peaks in the frequency spectra are due to the coupling of the two degenerate modes, caused by nonlinear effects. Midtvedt *et al.* [90] studied the thermal equilibration dynamics in graphene nanodrums and found that nonlinear modal

coupling leads to spectral broadening and redistribution of initially localized energy from the fundamental vibrational mode to other vibrational modes.

1.5 Open questions

The literature survey identified several open questions regarding the use of MD simulations in studying material damping and nonlinear oscillation in nanoresonators. These considerations motivate the work presented in this thesis.

- *What are the methods for simulating damping in nanoresonators under isothermal conditions?*

As outlined in the previous section, majority of the MD simulation studies concerning material damping in nanoresonators utilized the adiabatic microcanonical ensemble. The constant increase in temperature of a damped resonator in NVE ensemble may influence estimates of damping when the underlying dissipation mechanism is temperature dependent. This effect can be avoided by evolving the resonator under isothermal conditions using NVT ensemble. In addition, isothermal simulations are important because they mimic the typical operating conditions of nanoresonators. However, the technique for simulating damping is NVT ensemble is still at an early stage of development, and many basic aspects of estimating damping still remain to be addressed.

- *What are the mechanisms of material damping in single-crystal silicon and amorphous Silicon nanoresonators?*

Single-crystal Si is a common choice for manufacturing mechanical resonators because they are lowly damped. For example, resonators made of single-crystal Si have been measured to have Q -factors to the tune of 10^6 at 300 K [41, 91]. However, several studies have shown that the Q-factor of nanoresonators made of single-crystal silicon diminishes by several orders of magnitude

while oscillating at high frequencies (few hundred MHz to GHz range) [32, 92]. Literature suggest the presence of several damping mechanisms at play, however the dominant damping mechanism is still not known.

The long range order of the crystalline materials is broken in its amorphous form. This atomic disorder results in anomalous behavior in the acoustic and thermal properties of amorphous materials compared to their crystalline counterparts [93]. For example, despite a lot of activity our understanding of damping in amorphous silicon is not clear. Isothermal molecular dynamics simulations of damping in single-crystal Si and amorphous Si for understanding the underlying mechanisms is therefore an open field.

- *Can MD simulations be used to understand the nature of nonlinear oscillations and the governing mechanisms?*

A handful of articles [89, 90] have tried to explore nonlinear oscillations in nanoresonators using molecular dynamics simulations. All of these studies have primarily focused on thermal noise mediated nonlinear oscillations and modal coupling. There are several other features of nonlinear oscillations which occur during harmonic oscillations remain unexplored, such as internal resonance, subharmonics, super harmonics, bifurcations etc. Methods need to be developed and compared with existing models to demonstrate the utility of MD simulations for exploring the rich science at the nanoscale.

1.6 Objectives of the thesis

(1) Establish methods for isothermal molecular dynamics simulations of damping using single-crystal Ni as a model material.

(2) Use the technique to study mechanisms of material damping in two materials, technologically important single-crystal Si and amorphous Si.

(3) Establish protocols for studying nonlinear oscillations in nanoresonators using MD simulations.

1.7 Organization of the thesis

Considerations in the previous sections motivate the work presented in this thesis. The organization of the chapters are described below. A schematic categorization of the literature on damping and nonlinear oscillations in nanoresonators studied using MD simulations and the results reported in this thesis is presented in Figure 1-1.

Chapter 2 critically reviews different mechanisms of material damping relevant in single-crystal and amorphous materials. Also presented are the relationships between different measures of damping and the governing dynamics. These relationships are subsequently used in the following chapters for calculating damping using molecular dynamic simulations. The chapter ends with discussions on Duffing nonlinearity. Chapter 3 presents a brief introduction to different aspects of molecular dynamics simulations, such as numerical integration schemes, interatomic potentials, thermostat, and other relevant boundary conditions.

Chapter 4 establishes the methods for estimating damping in a single-crystal Ni nanoresonator using isothermal MD simulations. The nanoresonator was evolved in NVT ensemble and the thermally relaxed structure was then used for damping simulations in the subresonant and the resonant regime. The chapter starts with the details of the structural dimensions of the resonator, thermal equilibration steps (thermostat time constant, thermal equilibration duration), axial

stiffness, modeshape and natural frequency. Choices of the simulation parameters needed to ensure precision of the damping estimates have been discussed. In the resonant regime, damping in the nanofilm showed signatures of nonlinear oscillations. The methodology adopted for tackling nonlinearities to estimate precise values of damping has been discussed.

Chapter 5 reports the results from MD simulations of damping in a single-crystal Si nanofilm and single-crystal Si nanowire as a function of frequency and temperature. Details of the thermal relaxation steps have been discussed. Damping was evaluated in the subresonant regime as loss tangent and loss factor. A comparison of the simulated results with relevant sources of material damping has been presented.

Chapter 6 present the estimates of damping in an amorphous nanofilm as functions of frequency and temperature. The details of the method used for the preparation and characterization of the amorphous structure have been discussed. Damping in the amorphous nanofilm is compared with that of the single-crystal nanofilm mentioned in Chapter 5. The chapter ends with a discussion on possible sources of material damping in amorphous Si.

Chapter 7 presents simulations of nonlinear oscillations in two doubly-clamped nanobeams for the flexural mode oscillations and for the longitudinal mode oscillations in a nanofilm made of single-crystal Si. A protocol is presented to obtain the steady-state harmonic oscillations in the nanoresonators in the vicinity of their resonance frequencies. The harmonic response of the doubly-clamped nanobeam and the nanofilm is compared with the Duffing equation. The doubly-clamped nanowire displayed signatures of internal resonance, qualitative comparison of which with cubic coupled Duffing equation has been presented.

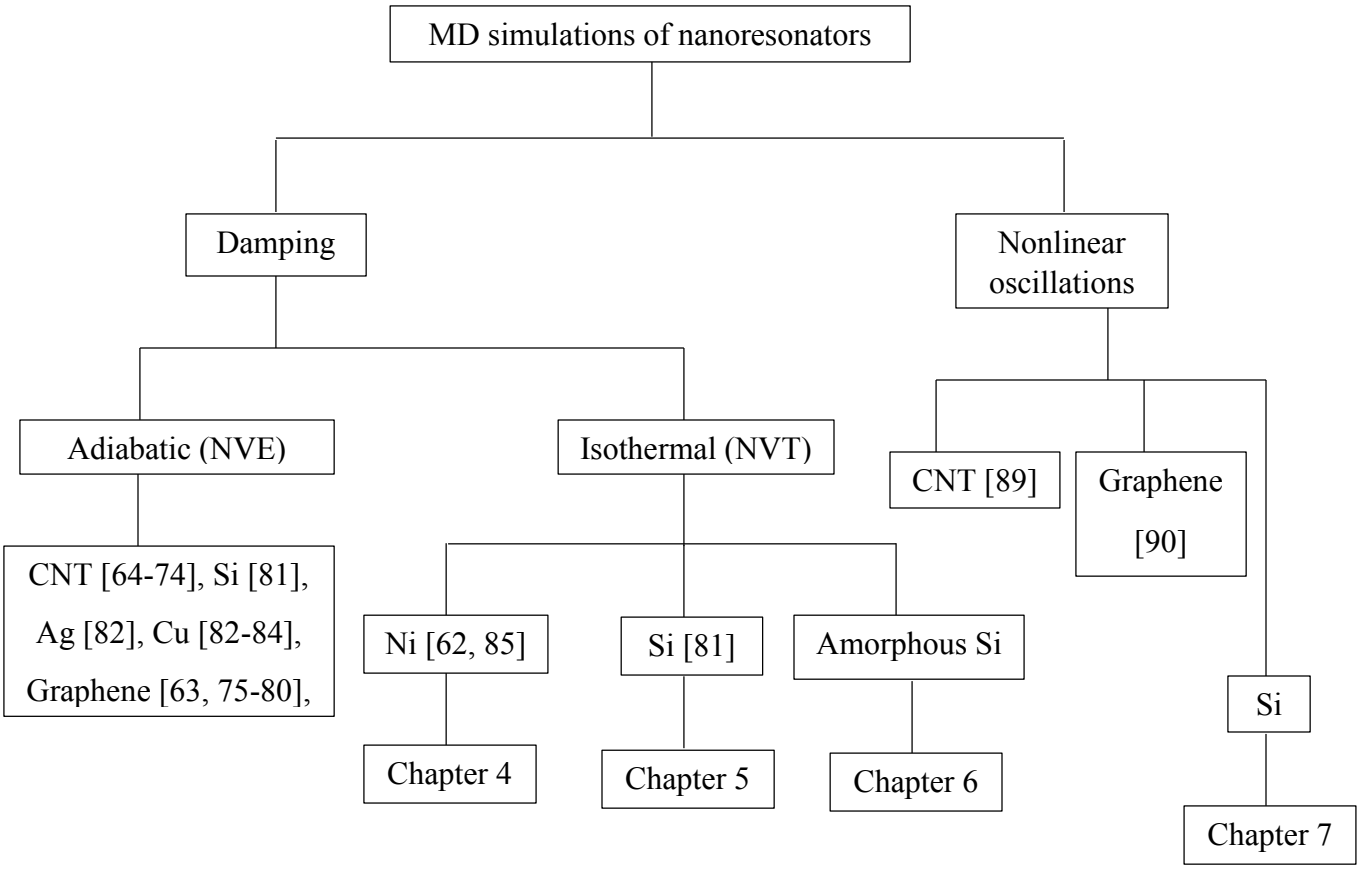

Figure 1-1: Schematic categorization of the literature on damping and nonlinear oscillations in nanoresonators.

Chapter 2

Review of material damping and nonlinear oscillations

Damping is the dissipation of energy stored in vibrating structures. The magnitude of dissipation depends on the physical mechanisms operating in the structure. The mathematical equations describing the nature of damping are generalizations and approximations of the actual physical processes operating in the material. Nonlinearities, in general, arise in systems which have products of dependent variables and their derivatives in the equations of motion. The sheer quantity of articles published in these two fields makes it difficult to report all of them. Exhaustive reviews on different aspects of material damping and nonlinear oscillations can be found in the books by Norwick & Berry [37] and Nayfeh & Mook [50].

The sources of material damping focusing on the ones relevant in single-crystal Si and amorphous Si are presented in Section 2.1. The discussions include different aspects of thermoelastic damping, phonon-phonon interactions, two level systems and surface damping. Section 2.2 summarizes various measures of damping and establishes their relationships with the dynamics. These relationships have been used for the estimation of damping in different parts of this thesis. Nanoresonators show nonlinear phenomenon, which includes the Duffing nonlinearity. Section 2.3 presents a brief summary of the different aspects of the Duffing nonlinearity. In Section 2.4, we discuss a specific mechanism of nonlinear modal coupling known as internal resonance.

2.1 Mechanisms of material damping

Mechanisms of material damping originate inside the resonator material and at the free surfaces. Depending on the nature of the mechanism, material damping can be broadly classified into two categories: (a) fundamental damping mechanisms, and (b) internal friction. Fundamental damping mechanisms are unavoidable and therefore set the lower limit on damping in resonators. These mechanisms are thermoelastic damping, phonon-phonon damping etc. Internal friction refers to damping mechanisms which arise from the activity of different crystallographic defects (for example, vacancies, interstitial atoms, substitutional atoms, surface adatoms, dislocations, grain boundaries etc.). Each type of defect can give rise to several mechanisms of dissipation, for example damping from two level systems in amorphous materials, surface damping from free surfaces etc.

2.1.1 Thermoelastic damping (TED)

The thermoelastic damping (TED) is one of the main sources of energy dissipation in small mechanical structures [94]. TED arises from the irreversible heat transfer between different regions in an oscillating solid [95]. To understand the origins of the temperature gradient, let us consider the case of a structure under the influence of a travelling wave. As the wave passes through the structure, different portions in the structure expand and contract. Depending on the magnitude of the thermal expansion coefficient this periodic shape change results in a stress field. Under adiabatic conditions, the compressed regions heat up whereas the regions in tension cool down creating thermal gradient throughout the body [96]. The heat transfer from the hot spots to the cold spots of the structure leads to entropy generation thereby leading to damping.

TED is generally large in flexural mode resonators. But, uniform spatial strain gradients caused by longitudinal vibrations produce very small TED [9, 62]. TED in a structure oscillating in the longitudinal mode is given by [97]

$$\frac{1}{Q_{TED}} = \frac{2\pi f k T \alpha^2 \rho}{9 C_V^2} \tag{2.1}$$

where k is the thermal conductivity, T is the equilibrium temperature, α is the coefficient of thermal expansion, ρ is the density, and C_V is the specific heat at constant volume of the material.

2.1.2 Phonon mediated damping

Phonons are vibrational states of matter. In the absence of lattice impurities, imperfections and electrons, phonons can scatter in two ways, (a) Normal process, and (b) Umklapp process [98]. In case of normal scattering the momentum of the phonons is conserved, unlike the Umklapp processes [99, 100]. The nature of the phonon damping depends on two time scales: the period of mechanical vibration, τ_v (where $\tau_v = 2\pi/f$) and the mean phonon relaxation time (τ_p) [100]. The relaxation time τ_p is the time required for restoration of thermal equilibrium between different phonon branches and is dependent on both the Normal and Umklapp processes. At temperatures comparable to the Debye temperature, τ_p is dominated by the Umklapp processes and can be related to the thermal conductivity by

$$\tau_p = \frac{3k}{C_V V_s^2}, \tag{2.2}$$

where the velocity of sound (V_S) is given by

$$V_s = \sqrt{\frac{E}{\rho}}, \tag{2.3}$$

where E is the elasticity constant of the material in the direction of the propagating wave. The probability of the occurrence of the Umklapp processes diminish rapidly at low temperatures and therefore, under such conditions the relation between τ_p and the thermal conductivity mentioned in Eq. (2.2) is no longer valid [37, 101].

2.1.2.1 Phonon relaxation (Akheiser damping)

The nature of the phonon-phonon scattering process in the regime $2\pi f\tau_p < 1$ was first modelled by Akheiser in 1937 [102]. At thermal equilibrium the distribution of phonon population obeys Planck distribution law. Akheiser suggested that the ultrasonic wave travelling through a crystal causes anisotropic temperature changes of different phonon branches. This temperature change arises from the frequency modulation of each phonon branch because of the modulation of the elastic properties of the medium. The mode dependent Grüneisen parameter (γ) which describes the vibrational properties of solids, determines the extent of the coupling between the strain field and the phonon modes. The modulated phonons attain thermal equilibrium by phonon-phonon scattering leading to modulation of equilibrium population of each phonon mode. The delay in readjusting to the new equilibrium population, results in phase lagging behind the driving wave causing dissipation of energy.

Akheiser used time independent Boltzmann transport equation (BTE) to analyze the kinetics of the phonon scattering process. In its most general form, the BTE can be written as [99]

$$\left(\frac{\partial n(\vec{u},s)}{\partial t}\right)_{coll} = \frac{\partial n(\vec{u},s)}{\partial t} + v.\nabla_r n(\vec{u},s) + \frac{F_e}{\hbar}.\nabla_k n(\vec{u},s), \tag{2.4}$$

where $n(\vec{u},s)$ is the distribution function of phonons with wave vector $\vec{u}$, and polarization s, v is the phonon group velocity, and F_e is the force field. $\left(\frac{\partial n(\vec{u},s)}{\partial t}\right)_{coll}$ is the rate of change in phonon population in different phonon branches due to the phonon-phonon collisions. For small strain gradients in bulk solids the second and the third term in the right hand side of Eq. (2.4) can be ignored. The magnitude of energy dissipation was calculated by multiplying the rate of change of entropy with temperature.

There have been several theoretical modifications proposed to the derivation of Akheiser. Woodruff and Ehrenreich [103] suggested two major modifications: (a) they calculated the collision term in Eq. (2.3) by considering specific contributions from normal phonon-phonon processes and Umklapp processes, and (b) the magnitude of the dissipated energy was calculated as the amount of energy the phonons give away to the thermal bath. In the simplest form the expression for Akheiser damping derived by Woodruff and Ehrenreich is given by

$$Q_{AKE}^{-1} = \frac{4\pi f \tau_p C_V T \gamma^2}{3\rho V_s^2}, \tag{2.5}$$

Mason and Bateman [104] derived expression for Akheiser damping considering the effect of time dependent strain caused by the travelling wave on the phonon branches in different directions in the crystal. They introduced a nonlinearity parameter as a function of second the order and the third order elastic constants of crystals. Their calculations produced good agreement with experimental measurements of Akheiser damping in single-crystal Si and Ge. However, it was

later pointed out by Barrett and Holland [105] that the derivation was not correct and the match with experimental results was accidental.

A different set of corrections to the Akheiser's damping model was brought about by Bömmel and Dransfeld [106], which were later modified by Maris [107]. The assumptions used by Bömmel and Dransfeld are: (a) dispersion can be neglected under the assumption that the Grüneisen parameter (γ) for a given phonon branch is independent of frequency, where dispersion is described as the relationship between the frequency and the wavelength of a phonon mode, (b) only two phonon modes are present, longitudinal and transverse, (c) all phonon modes have the same heat capacity, and (d) entropy is generated because of energy exchange between different phonon modes. The expression for Akheiser damping from the work of Maris is given by [107]

$$Q_{AKE}^{-1} = \frac{C_V T \gamma^2}{\rho V_s^2} \frac{\omega \tau_p}{1 + (\omega \tau_p)^2}. \tag{2.6}$$

where ω is the angular frequency of oscillation.

2.1.2.2 Phonon collisions (Landau-Rumer damping)

Akheiser's theory of phonon damping is invalid when $2\pi f \tau_p > 1$. Such situations are observed at very high oscillation frequencies and low temperatures. Under such circumstances the phonon mean free path is larger than the wavelength of the external harmonic force. Landau and Rumer suggested that for $2\pi f \tau_p > 1$ the phonons are scattered from the travelling wave to different phonon modes by interactions with other individual phonons of the resonator. This results in frequency

independent energy dissipation. The expression for damping in the Landau and Rumer regime is given by [108]

$$\frac{1}{Q_{L-R}} = \frac{\pi^5 \gamma^2 k_B^4 T^4}{15 \rho V_s^5 h^3}, \tag{2.7}$$

where k_B is the Boltzmann's constant, and h is the Planck's constant.

2.1.3 Two level systems (TLS)

Experimental investigations of thermal and acoustic properties of amorphous materials have revealed striking differences with their crystalline counterparts [93]. For example, according to Debye theory, thermal conductivity (k) and specific heat (C) of crystalline insulators are proportional to T^3 below 1 K. However, in amorphous materials in the same temperature range k is proportional to T^2 and C is proportional to T. Similarly, unexpected trends have been observed in the experimental measurements of damping as functions of temperature and frequency in majority of amorphous materials. For example, irrespective of chemical composition and processing route, damping in majority of amorphous materials is qualitatively similar below 10 K, this is known as the glassy range. Below 10 K damping approaches a temperature independent plateau, the fall away at the lowest temperature depends on the frequency of oscillation, occurring at lower temperatures with decreasing frequencies [93]. Several theories have been proposed in order to explain these anomalies, the most successful one being the model of two level systems (TLS), introduced simultaneously by Phillips [109] and Anderson *et al.* [110]. This model was later named as the Standard Tunneling Model (STM).

The basic tenet of the TLS model is the assumption that groups of atoms in amorphous materials have more than one potential minimum. This assumption is invalid in crystalline materials where atoms have single potential minimum. To further elucidate the point, let us consider the arrangement of atoms in vitreous silica shown in Figure 2-1 (a), in which the number of atoms per ring and the binding angles are different from cristobalite. As a result different atoms or group of atoms can move between two preferable configurations [111].

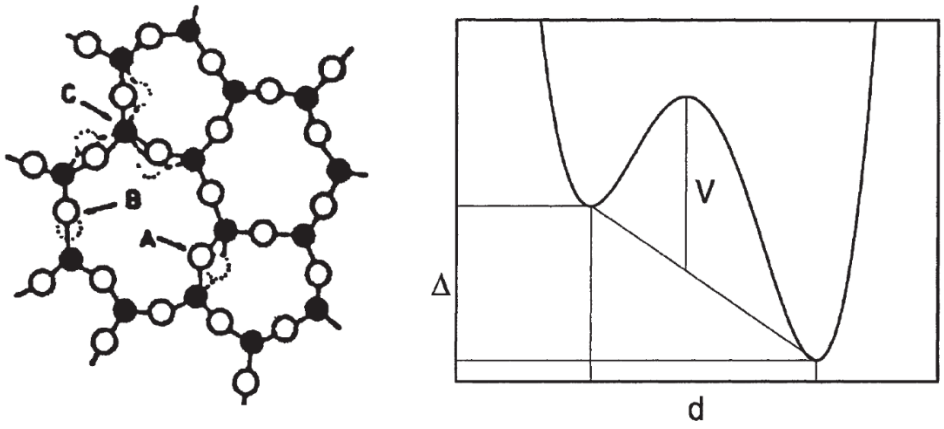

Figure 2-1: (a) Atomic configuration in vitreous silica, arrows indicate three possible defects states (Figure taken from Ref. [111], (b) Schematic illustration of a two-level system (TLS) with barrier height V, asymmetry energy Δ, well separation d (Figure taken from Ref. [112]).

A double well potential model can be applied to amorphous materials where an atom or group of atoms can occupy any one of the two possible energy minima. This situation is schematically shown in Figure 2-1 (b). Because of lack of crystal symmetry the potential wells are separated by an energy barrier height V, d is the separation between the two potential wells along the configurational coordinate and Δ is called the asymmetry energy. At low temperatures, the atoms cannot switch between different wells classically by overcoming the potential difference, instead quantum tunneling facilitated by coupling with the phonons (in case of insulators) gives rise to the

atomic activities. During harmonic oscillations the motions of the atoms produce strain which couples the tunneling atoms and the phonons.

2.1.4 Surface damping

Studying surface damping and the factors that promote it is difficult. As a result a clear understanding of the underlying mechanisms is not available. Experiments show that damping in resonators linearly increase with an increase in the surface to volume ratio. This behavior has been attributed to surface damping mechanisms [113]. In single-crystal materials surface damping could transpire from: (a) poorly terminated bonds in the surface states, (b) due to a thin layer of surface contamination, and (c) rearrangement or motion of surface dangling bonds between metastable positions [114]. For structures with very small surface to volume ratios, the damping caused by the surface related phenomenon is relatively small compared to the contribution of atoms in the bulk and therefore can be neglected. But as the surface to volume ratio increases the surface related damping becomes significant. Experimental results suggest that the surface related losses are negligible when the structural dimensions are larger than few millimeters [41]. However, it becomes significant as the surface to volume ratio increases [113]. Several studies indicate that surface damping can be significantly reduced by surface treatments such as annealing [94], removal of contaminants from the surface [115], and passivation of dangling bonds in the surface [116].

2.2 Measures of damping

A structure under the application of a periodic force, moves back and forth across an equilibrium position because of a periodic restoring force. In linear oscillators, the restoring force is

proportional to the displacement of the body from the equilibrium position. For damped linear systems the equation of motion under the application of sinusoidal harmonic force is given by

$$m_0\ddot{x} + c\dot{x} + Kx = F_0 \sin(2\pi ft), \tag{2.8}$$

where x is the displacement, c is the coefficient of viscous damping, K is the stiffness, F_0 is the magnitude of the harmonic force, and f is the frequency of oscillation. For such systems, damping is defined by the ratio of $\frac{\Delta W}{W}$, where ΔW is the amount of energy dissipated per cycle of vibration, and W is the total mechanical energy stored in the structure. Additionally damping is measured by monitoring the dynamics of the oscillations. The common measures of damping are: the loss factor (η), the loss tangent ($\tan\phi$), loss angle (ϕ), logarithmic decrement (δ), and the quality factor (Q). For small values of damping ($\phi < 0.01$) $\tan\phi$ and ϕ are equivalent. The loss angle and the loss factor are calculated from the dynamics of the structure from the steady-state forced harmonic oscillations. The logarithmic decrement is calculated by taking the logarithm of two consecutive amplitudes of the structure during its free decay. The Q-factor is calculated from the frequency response of the structure during harmonic oscillations near the resonance frequency. Alternatively, the Q-factor can also be calculated by fitting a Lorentzian curve to the PSD (Power Spectral Density) of the thermal noise in the vicinity of the resonance frequency. It is important to mention that the logarithmic decrement and the Q-factor give estimates of damping only at the resonance frequencies of the structure whereas the loss angle and the loss factor are valid at any frequency. For small values of damping ($\phi < 0.01$) the different measures are related by Eq. (1.1). This section will present a brief overview of the different measures of damping and their relationship with the dynamics.

2.2.1 Loss factor, η

The loss factor is defined as

$$\eta = \frac{\Delta W}{2\pi W} \tag{2.9}$$

ΔW is given by

$$\Delta W = \frac{1}{ft_f} \int_0^{t_f} F_0 \sin(2\pi ft).V_{nr} dt, \tag{2.10}$$

where V_{nr} is the velocity of the structure, and t_f is the duration of forced vibration.

The stored energy, W is given by [13]

$$W = \frac{1}{2} \int_0^l SE\left(\frac{\partial u_{nr}}{\partial x}\right)^2 dx, \tag{2.11}$$

where S is the cross section of the beam, and u_{nr} represents the displacement profile along the beam. For linear displacements, the stored energy is given by

$$W = \frac{1}{2} KA^2 \tag{2.12}$$

where A is the amplitude of vibration.

2.2.2 Loss tangent, $\tan\phi$

This measure of damping denotes the tangent of the angle by which the response of a structure lags behind the harmonic force. The situation is depicted in Figure 2-2 in which the curve with blue color represents the trace of the harmonic force and the black curve represents the displacement of the oscillating structure. The phase lag, ϕ, is the difference in phase between the

applied harmonic force and the displacement. Therefore, the displacement response of a damped resonator to a harmonic applied force is given by [7]

$$x = A\sin(2\pi f - \phi) \tag{2.13}$$

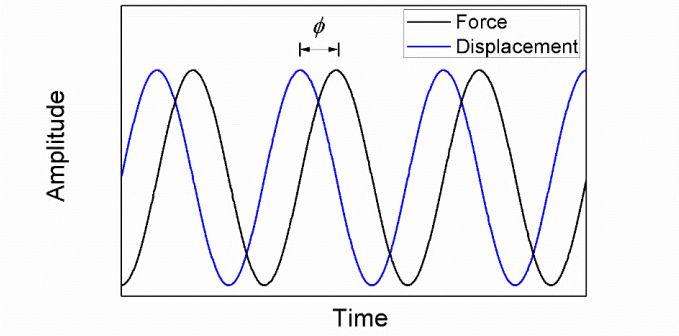

Figure 2-2: Schematic illustration of the loss angle, ϕ. The black line represents the harmonic force and the blue line is the displacement of the structure.

2.2.3 Logarithmic decrement, δ

The logarithmic decrement, δ, is measured from the response of freely decaying structures. In order to calculate δ, initially, the structure is excited at the resonance frequency followed by the removal of the excitation. The structure vibrates at the resonance frequency with decaying amplitudes as it continues to dissipate energy. The vibration eventually ceases to zero once all the stored energy is spent. For an underdamped system, δ is defined as the natural logarithm of the ratio of the amplitudes of any two successive oscillations. Therefore, δ can be expressed as

$$\delta = \frac{1}{n}\ln\left(\frac{A_{\tau_v}}{A_{\tau_v + n\tau_v}}\right), \tag{2.14}$$

where A_{τ_v} and $A_{\tau_v + n\tau_v}$ are the peak amplitudes n period away. Alternatively, the logarithmic decrement of a freely decaying signal can be calculated by computing the Hilbert transform of the

time series of vibration [41]. The Hilbert transform of the signal $y(t)$, is defined as the convolution integral

$$\tilde{y}(t) = H[y(t)] = \int_{-\infty}^{\infty} \frac{y(u)}{\pi(t-u)} du. \tag{2.15}$$

Hilbert transform can also be defined as a 90˚ phase shift system, i.e., $\tilde{y}(t)$ is equal to $y(t)$ shifted by 90˚. For a viscously damped system, the equation of motion is expressed as

$$y(t) = e^{-\zeta\omega_n t} \cos(\omega_d t + \theta_d), \tag{2.16}$$

where ω_n is the undamped angular natural frequency, ω_d is the damped natural frequency and θ_d is a constant. The Hilbert transform of $y(t)$ shifted by 90˚ and is given by

$$\tilde{y}(t) = e^{-\zeta\omega_n t} \sin(\omega_d t + \theta_d). \tag{2.17}$$

Now, we define an analytical signal $B(t)$

$$B(t) = y(t) + j.\tilde{y}(t), \tag{2.18}$$

The phasor form of $B(t)$ is given by

$$B(t) = E(t)e^{j\varphi(t)}, \tag{2.19}$$

where $\varphi(t)$ is the instantaneous phase signal and is equal to $\omega_n t$. $E(t)$ is known as the envelope signal and can be expressed as

$$E(t) = \sqrt{y^2(t) + \tilde{y}^2(t)}. \tag{2.20}$$

A line can be fit to the logarithm of the envelope signal using the technique of least mean squares. The slope of this line, *m*, is equal to δf_0. Assuming low damping, we can relate the slope, *m*, to the logarithmic decrement, δ, by

$$\delta = \frac{m}{f_0} = -\frac{1}{f_0}\frac{d(\log(E(t)))}{dt}, \tag{2.21}$$

The logarithmic decrement is a measure of damping at the resonance frequency.

2.2.4 Q - factor from harmonic oscillations

The Q-factor can be extracted from the steady state harmonic response of the structure. This is achieved by applying harmonic forces with frequencies in the vicinity of the resonance frequency. The frequency response curves of the system for different harmonic forces are symmetric across the resonance frequency and the resonance frequency is independent of the amplitude of oscillation. The Q-factor of the structure at the resonance frequency can be calculated from the half power points of the frequency response of the amplitude curve and the resonance frequency. If f_1 and f_2 correspond to the frequencies where the amplitude of forced response takes the value of $\frac{1}{\sqrt{2}}$ the amplitude at resonance, then Q at f_0 can be calculated using the expression [46]

$$Q = \frac{f_0}{|f_2 - f_1|} \tag{2.22}$$

2.2.5 Q - factor from thermal noise

Thermal noise is defined as the spontaneous, random fluctuation of atoms that manifest at temperatures above absolute zero. The power spectral density (PSD) of thermomechanical noise

exhibits prominent peaks at the natural frequencies of vibration. This observation can be explained using the Equipartion theorem, which states that the kinetic energy is distributed equally among all energetically possible degrees of freedom of a system. The kinetic energy of atoms couple with the resonators normal modes resulting in multiple peaks in the PSD. The Fluctuation-Dissipation theorem (FDT) is combined with the Equipartition Theorem to link the spectrum of the thermomechanical noise and the dissipation of a system [117-119]. FDT dictates that in the presence of a dissipative process, there will always be a reverse process present. This consideration leads to spontaneous fluctuations. The first peak (corresponding to the fundamental natural frequency) in the Power Spectral Density (PSD) is symmetric and well-approximated by a simple Lorentzian function given by

$$S_x(f) = \frac{k_B T}{\pi k} \frac{\frac{f_0}{2Q}}{(f - f_0)^2 + \left(\frac{f_0}{2Q}\right)^2} \tag{2.23}$$

where S_x denotes the PSD of the time series of the displacement noise. Therefore the Q-factor at the natural frequency can be estimated by fitting Eq. (2.23) to the PSD of the thermal noise.

To obtain accurate estimation of damping the noise should be captured for extended periods of time. However, in experiments or simulations the noise can only be captured for a brief period of time, resulting in an unwanted sampling noise in the PSD. As a consequence, the estimations of Q-factor are associated with uncertainties. Standard deviation in the fitted Q-factor obtained from least squares analysis, due to the presence of the sampling noise is given by [120]

$$\sigma_Q = \sqrt{\frac{6Q_0^3}{\pi f_0 \tau}}, \tag{2.24}$$

where τ is the duration for which the noise is captured and Q_0 is the mean value of the quality factor.

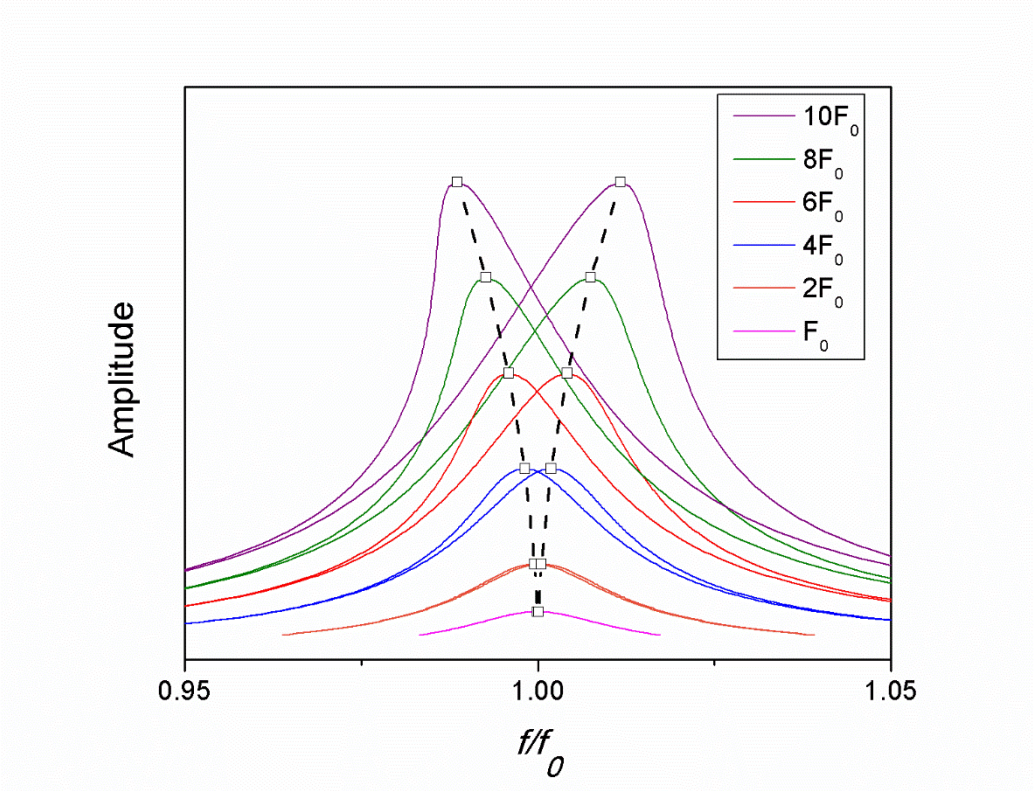

Figure 2-3: Schematic representation of steady-state amplitude response of a Duffing oscillator as a function of forcing frequency (f), showing a shift in the peak frequency depending on arbitrary magnitudes of harmonic force F_0. The shift in the peak frequency is dependent on the nonlinear spring constant K_2 and the magnitude of the force. The assumed Q-factor of the oscillator is 50 and its natural frequency is f_0.

2.3 The Duffing oscillator

The discussion in the previous section was limited to the linear oscillatory systems. However, in a realistic system various type of nonlinearities can exist and for such cases the Hookian type linear

restoring force assumption is not valid. In a number of publications, the Duffing equation has been found to capture the nonlinear oscillations in nanoresonators. In this section we discuss the basic tenets of the Duffing equation in relation to mechanical oscillations. Also discussed are the relations between the dynamics of a Duffing oscillator and the Q-factor. The section ends with discussion on an interesting property of nonlinear oscillations known as internal resonance.

2.3.1 Dynamics

The cubic Duffing nonlinearity is introduced in the Eq. (2.8) by including cubic nonlinear restoring forces equal to $-K_1x - K_2x^3$, where K_1 is a linear elastic constant, and K_2 is a nonlinear elastic constant. The governing equation is given by [50]

$$m\ddot{x} + c\dot{x} + K_1x + K_2x^3 = F_0 \sin(2\pi ft), \tag{2.25}$$

Schematic representation of steady-state frequency response of amplitude for different magnitudes of harmonic forces (arbitrary) for two different Duffing oscillators with Q-factor 50 (arbitrary) is shown in Figure 2-3. The following observations can be made from the figure.

a) For small magnitudes of applied force (F_0, and $2F_0$), the responses of the oscillators show characteristic peak at the natural frequency (f_0). Similar to linear oscillations, an increase in the magnitude of the harmonic force increases the amplitude of oscillation.

b) An increase in the magnitude of the force (e.g., $4F_0$, $6F_0$, ..) causes a shift in the frequency corresponding to the peak amplitude towards higher or lower frequencies, depending on the sign of the nonlinear elastic constant K_2. For positive values of K_2, the response is said to be hardening type. On the other hand, the response is said to be softening type for negative values of [121].

c) The dotted lines in the figure are obtained by joining the peak amplitudes for different forces and is called the back-bone curve.

d) If one traces the amplitude of oscillation as a function frequency for any force magnitude, there would be frequencies at which multiple solutions exist. As a consequence, at these frequencies the oscillators can oscillate with different amplitudes, making the response unstable. The transition from stable to unstable or unstable to stable oscillations occur at these frequencies with an associated tangent of infinity. This behavior is called jump phenomenon [50].

2.3.2 Q -factor

The quality factor, Q, for a Duffing oscillator can be extracted from the equation [42]

$$\frac{2Q(f-f_n)}{f_n} = \frac{2}{\sqrt{3}}\frac{A^2}{A_c^2} \pm \sqrt{\frac{A_p^2}{A^2}-1}, \quad \{n = 0,1,2,3..\} \tag{2.26}$$

where f_n is the resonance frequencies of the structure and n is the mode number, A_c is called the critical amplitude and is defined as the first amplitude which displays infinite slope in the frequency response curve, and A_p is the peak amplitude of the curve. It can be shown that the ratio of A_c over A_p at the onset of nonlinearity is equal to $\frac{2}{\sqrt{3}}$ [50]. In general, the critical amplitude at the onset of nonlinearity is given by

$$A_c = 2f_n \frac{l_x^2}{\pi}\sqrt{\frac{\rho\sqrt{3}}{EQ}}, \tag{2.27}$$

where l_x is the length of the oscillator. For a doubly-clamped beam with rectangular cross-section, the expression for A_c is given by

$$A_c = \frac{2}{\sqrt[4]{3}} \sqrt{\frac{1}{Q}\left(\frac{{w_y}^2}{3} + \frac{T_0 l_x^2}{\pi^2 E w_y t_z} \right)}, \tag{2.28}$$

where T_0 is the tension in the beam and w_y and t_z are the width and the thickness of the structure. The backbone curve of a Duffing oscillator joins the peak amplitudes of the frequency response curves and is given by

$$\frac{2Q(f - f_n)}{f_n} = \frac{2A_p^2}{\sqrt{3}A_c^2}. \tag{2.29}$$

2.4 Internal resonance

Unlike a single-degree-of-freedom system, a continuous mechanical system can be considered to have finite degrees of freedom. As a consequence, these systems have finite number of resonance frequencies and normal modes [46]. In a linear continuous system, when a particular normal mode is being excited, the other modes remain dormant. Therefore, any interaction between different mechanical modes is prohibited in linear theory. But, this linearized idealization of mechanical motion is not valid in case of nonlinear oscillations. As a consequence, different modes constantly interact and exchange energy during oscillations. A particular case of interest is internal resonance, that exists when the resonance frequencies of different modes are commensurable, that is there exists integers $m_1, m_2, m_3, \ldots, m_n$, such that $m_1 f_1 + m_2 f_2 + m_3 f_3 + \ldots + m_n f_n \approx 0$, where $f_1, f_2, f_3, \ldots, f_n$ are the resonance frequencies of different modes [50].

In mechanical systems, internal resonance are the cause of most of the strongly nonlinear phenomenon, such as bifurcations. Internal resonance is named as the ratio of the frequencies of the modes being coupled through the internal resonance, for example if the coupled modes have resonance frequencies $5f_n$ and, f_n then the internal resonance would be called 5:1 type. The first instance of 3:1 internal resonance in a doubly-clamped quartz microresonators was reported in 2012 [122]. Very recently, internal resonance has been observed in MoS_2 nanomembranes as well [51].

2.5 Summary

Material damping can arise from various sources depending on the type of material and the nature and the configuration of the defects. A brief review of the different mechanisms of material damping relevant in single-crystal and amorphous materials is presented in Section 2.1. Several measures exist for the estimation of damping in linear resonators. Relationships between these measures and the dynamics of oscillation are presented in Section 2.2. Logarithmic decrement, and the Q-factor provide damping estimates only at the resonance frequency, however the loss tangent and the loss factor can be used to measure damping over the entire frequency spectrum. Section 2.3 gave a discussion on different aspect of Duffing nonlinearity, which included a comparison with linear oscillations, and a method for estimating Q-factor from the steady-state time harmonic response. In section 2.4 we provided a brief discussion on a specific mechanism of modal coupling in multi-degree-of-freedom nonlinear oscillators, namely the internal resonance. These discussions serve as foundations for the interpretations of simulated results of damping and

nonlinear oscillations in single-crystal Ni, Si and amorphous Si presented in different parts of this thesis.

Chapter 3

Foundations of MD simulations

MD simulations reported in this thesis were run on the CLUMEQ (Consortium Laval, Université du Québec, McGill and Eastern Quebec) supercomputer nodes, using LAMMPS (Large-scale Atomic/Molecular Massively Parallel Simulator) software developed by Sandia National Laboratory [123]. LAMMPS makes use of Message Passing Interface (MPI) for parallel communication and is a free, open-source software, distributed under the terms of the GNU General Public License. In this chapter, we describe different aspects of the implementation technique for MD simulation which include brief introduction to the algorithms used for numerical integration of the equations of motion, choice of simulation timestep, interatomic potentials, initial boundary conditions such as periodic boundary condition, and basics of thermostats.

3.1 Algorithms for solving equations of motion

For a system with N particles, the Newton's second law is given by

$$F_i = m_i a_i, \tag{3.1}$$

where m_i, x_i $(i = 1,..N)$ are the mass and the position of the i-th atom and F_i denotes the magnitude of the force acting on it. Alternately, the equation of motion can also be found using Hamiltonian dynamics. The Hamiltonian of an isolated system is constant and expressed as

$$H = \sum_{i=1}^{N} \frac{p_i^2}{2m_i} + U(x_i), \tag{3.2}$$

where p_i is the momentum of atom i, U is the potential energy of the system, which is a function of the atomic positions. The force field for individual atoms can be derived using the expression

$$F_i = \frac{\partial H}{\partial x_i}. \tag{3.3}$$

To solve for the atomic positions, and velocities, the equations of motion are discretized in time and integrated consequently using the method of finite difference. Several algorithms have been proposed over the past few decades to solve these equations numerically in a computationally effective manner, e.g. Gear algorithm [124], leap-frog algorithm [125], Verlet algorithm [126], and the velocity-Verlet algorithm [127]. LAMMPS uses the velocity-Verlet algorithm to solve the equations of motion of individual atoms.

The key idea of the Verlet algorithm is to calculate the position $\vec{x}(t+\Delta t)$ of a particle at time $t+\Delta t$ using the third order Taylor series expansion of its position at time t, and $t-\Delta t$. Denoting $\vec{V}_i$ as the velocity, $\vec{a}_i$ as the acceleration, and $\vec{b}_i$ as the third derivative of position with respect to t for the $i-$th particle, one can express positions of the particle i at time $t+\Delta t$, and $t-\Delta t$ as

$$\vec{x}_i(t+\Delta t) = \vec{x}_i(t) + \vec{V}_i(t)\Delta t + \frac{\vec{a}_i(t)\Delta t^2}{2} + \frac{\vec{b}_i(t)\Delta t^3}{6} + O(\Delta t^4), \tag{3.4}$$

$$\vec{x}_i(t-\Delta t) = \vec{x}_i(t) - \vec{V}_i(t)\Delta t + \frac{\vec{a}_i(t)\Delta t^2}{2} - \frac{\vec{b}_i(t)\Delta t^3}{6} + O(\Delta t^4). \tag{3.5}$$

Eq. (3.4) and (3.5) can be combined as

$$\vec{x}_i(t+\Delta t) = 2\vec{x}_i(t) - \vec{x}_i(t-\Delta t) + \vec{a}_i(t)\Delta t^2 + O(\Delta t^4). \tag{3.6}$$

Further, Eq. (3.1) and (3.6) can be combined and expressed as

$$\vec{x}_i(t+\Delta t) = 2\vec{x}_i(t) - \vec{x}_i(t-\Delta t) + \frac{F_i}{m_i}\Delta t^2 + O(\Delta t^4). \tag{3.7}$$

The term F_i for individual atoms is obtained from the interatomic potential. Also, subtracting Eq. (3.6) from Eq. (3.5) and doing some elementary operations we get

$$\vec{V}_i(t) = \frac{\vec{x}_i(t+\Delta t) - \vec{x}_i(t-\Delta t)}{2\Delta t} + O(\Delta t^2) \tag{3.8}$$

Eq. (3.7) is correct except for errors of order $O(\Delta t^4)$ (local truncation errors) and velocities from Eq. (3.8) are susceptible to errors of the order $O(\Delta t^2)$. However, for the calculation of $\vec{x}_i(t+\Delta t)$, it is necessary to know the position of the atoms in the previous step $\vec{x}_i(t-\Delta t)$, which is estimated as: $\vec{x}_i(-\Delta t) = \vec{x}_i(0) - \vec{V}_i(0)\Delta t$. This leads to a numeric error when $\vec{a}(t)\Delta t^2$ is added to larger $\vec{x}_i(t)$ and $\vec{x}_i(t-\Delta t)$. The advantages of the Verlet algorithm are: (a) it is straightforward, and (b) the storage requirements are moderate.

Considering this shortage, the velocity-Verlet algorithm was proposed which is included in the LAMMPS [123] package and has been used for simulations presented in this thesis. The velocity-Verlet algorithm adopts half-step velocity calculation and calculates position, velocity, and acceleration all at the same time and minimizes round-off errors. In addition, the velocity-Verlet algorithm requires lesser computing resources compared to the Verlet algorithm, and takes the form

$$\vec{x}_i(t+\Delta t) = \vec{x}_i(t) + \vec{V}_i(t)\Delta t + \frac{\vec{a}_i(t)\Delta t^2}{2}, \tag{3.9}$$

$$\vec{V}_i(t+\Delta t) = \vec{V}_i(t) + \frac{\vec{a}_i(t) + \vec{a}_i(t+\Delta t)}{2}\Delta t. \tag{3.10}$$

3.2 Simulation timestep (Δt)

The computational cost of MD simulations is directly proportional to the magnitude of the timestep. The accuracy of the numerical calculations improves with the use of smaller Δt. It is however, desirable to use larger time steps to sample longer trajectories. Therefore, the choice of Δt is a trade-off between accuracy and computational feasibility.

For numerical stability and accuracy in conserving the energy, one typically needs to pick a time step Δt which is at least an order of magnitude smaller than the fastest time scale in the system. Too large a time step can lead to an unstable MD simulation because of irregular atomic collisions. These atomic collisions transpire because of large timestep resulting in nearly coinciding atomic positions for two or more atoms. This results in repulsive interactions between atoms, thereby generating strong forces and destroying inherent atomic arrangement. Typically, the magnitudes of Δt used in MD simulations are on the order of femtoseconds. A timestep of 1 fs have been used for the MD simulations of damping in single-crystal Ni [62, 85] and single-crystal Si [128].

3.3 Interatomic potential

In order to run MD simulations it is necessary to describe the rules that govern the interactions between a pair of atoms or the interaction of an atom with a cluster of atoms. Starting from Born-Oppenheimer approximation, treating atoms as classical particles, it can be shown that the Hamiltonian of a N particle system can be expressed by describing the effect of the electrons using a single potential energy function dependent on individual atomic coordinates, $U(r_1, r_2, ...r_N)$. This

potential function can then be used for developing equations for predicting the evolution of the system as a function of time by solving forces and torques acting on individual atoms.

In general there are three methods for obtaining the potential function. The most accurate method is to perform electronic structure calculations of forces using ab-initio simulations. However, these calculations are computationally expensive [129]. Alternatively, one can assume a functional form for the potential and select parameters that fit experimental data. These potentials (e.g. Lennard-Jones [130], Morse [131]), commonly known as pair potentials, are computationally less demanding, but are ineffective in capturing complex interactions of atoms in metallic bonds. The last method for producing potentials for metals, and semiconductors is to calculate the electronic wave function for limited atomic positions and apply several approximations derived from quantum-mechanical understandings (e.g. Embedded Atom Method (EAM) by Foiles *et al.* [132], Glue Model by Ercolessi *et al.* [133], bondorder potentials by Brenner *et al.* [128] etc.).

3.3.1 Embedded atom method (EAM) Potential

The damping simulations for single-crystal Ni reported in this thesis were performed using the EAM potential. The idea for generating EAM potential was developed by Foils and Baskes [132], but the particular potential used here was created by Angelo *et al*. [134]. The key idea of EAM method is that atoms in metallic systems are embedded into a gas made of electrons created by the rest of the atoms. The electron gas experienced by atoms at the surface of the metal is different from the atoms in the bulk. The functional form for the EAM potential is given by

$$U = \frac{1}{2}\sum_{j \neq i} \mathrm{O}_{ij}(r_{ij}) + F_i(\rho_i), \tag{3.11}$$

where r_{ij} is the distance between atoms i and j, $O_{ij}(r_{ij})$ is the pair energy dependent on the distance r_{ij}, F_i is the energy needed for placing an atom i into an electron gas with a density ρ_i resulting from the electrons associated with neighboring atoms. The functional form is fit to the cohesive energy, cubic elastic constants, equilibrium lattice constant, bond length and bond strength to obtain different parameters.

3.3.2 Stillinger-Weber (SW) Potential

In 1985, Stillinger and Weber proposed an interatomic potential for Si with two and three-body parts [135]. Silicon forms 4-coordinated tetrahedral bonded structures. The Stillinger-Weber (SW) potential, enforces the tetrahedral bond angle (109.47°) among triplets of bonded atoms by means of the three body component. Therefore, directional bonding is introduced in the Stillinger-Weber potential through an explicit three-body term of the potential energy expansion

$$U(\vec{r}_1,\vec{r}_2,..,\vec{r}_N)=\frac{1}{2}\sum_{i=1}^{N-1}\sum_{j=2}^{N}U_{i,j}^{(2)}+\frac{1}{6}\sum_{i=1}^{N-2}\sum_{j=2}^{N-1}\sum_{k=3}^{N}U_{i,j,k}^{(3)} \tag{3.12}$$

where $U_{i,j}^{(2)}$ is the two-body term and $U_{i,j,k}^{(3)}$ is the three-body term contribution to the total potential energy U. The two-body term is given by

$$U_{i,j}^{(2)}=\varepsilon A\left(B\left(\frac{r_{ij}}{\sigma}\right)^{-p}-1\right)e^{\left(\frac{1}{r_{ij}/\sigma-a}\right)}, \tag{3.13}$$

The three body term is:

$$U_{i,j,k}^{(3)} = \varepsilon\lambda e^{\left(\frac{\beta}{r_{ij}/\sigma - a} + \frac{\beta}{r_{ik}/\sigma - a}\right)} \left(\cos(\theta_{ijk}) + \frac{1}{3}\right)^2, \tag{3.14}$$

where $r_{ij} = |\vec{r}_i - \vec{r}_j| = \sqrt{(x_i - x_j)^2 + (y_i - y_j)^2 + (z_i - z_j)^2}$. The cutoff of this potential is determined by $r_c = \sigma a$. θ_{ijk} is the angle centered on atom i and is given by $\cos\ \theta_{ijk} = \vec{r}_j . \vec{r}_k / (r_j r_k)$. The values of the parameters $\varepsilon, \lambda, \sigma, \beta, A, B, p$ and a is presented in Table 3.1.

Table 3.1: Parameters used for Si in the Stillinger-Weber potential.

ε	β	σ	a	λ	A	B	p
2.16826 eV	1.2	2.0951 Å	1.8	21	7.049955627	0.6022245584	4

3.4 Thermostat

In NVT ensembles a thermostat facilitates energy transfer between the system and the heat bath, thereby maintaining its temperature. The use of a thermostat can be motivated by one of the following reasons: (i) to emulate experimental conditions, (ii) to study temperature dependent processes, and (iii) to evacuate the heat in dissipative non-equilibrium MD simulations. Several thermostats are used in NVT ensemble to maintain the temperature of the system, e.g. Anderson [136, 137], Langevin [127], and Nosé-Hoover thermostat [138]. Nosé-Hoover (NH) thermostat has been used for the results reported in this thesis.

The use of the NH thermostat requires the definition of an instantaneous temperature. To enable energy transfer between the system and the thermal bath, the equations of motion are modified

when a NH thermostat is used for the simulation. A frictional parameter Θ is introduced and the modified equation of motion is rewritten as

$$a_i = \frac{F_i}{m_i} - \Theta x_i, \tag{3.15}$$

$$\dot{\Theta} = -\frac{k_B d_f}{G} T(t) \left(\frac{T_0}{T(t)} - 1 \right). \tag{3.16}$$

where d_f is the number of internal degrees of freedom of the system, $T(t)$ and T_0 are the current and the reference temperature respectively. G is the equivalent mass of the thermostat and is given by $\tau_{NH} T_0 k_B d_f$; τ_{NH} is the specified time constant for temperature fluctuations and is given by

$$\tau_{NH}^2 = \frac{G}{d_f k_B T_0}. \tag{3.17}$$

The choice of the time constant (τ_{NH}) is crucial from the point of view of the requirement of computational resources. It is apparent from Eq. (3.16) that the friction coefficient, Θ, controls the rate of energy transfer in such a way that the current temperature of the system $T(t)$ is close to the desired temperature, T_0. It aids energy flow from the system to the thermal bath and results in fluctuations in temperature around T_0. A large τ_{NH} allows the system to attain T_0 faster, but generates rapid temperature fluctuations; a small value of τ_{NH} results in a sluggish response resulting in delayed attainment of thermal equilibrium.

3.5 Periodic Boundary Condition (PBC)

MD simulations become computationally demanding as the size of the structure increases, making it difficult to simulate properties for large bulky systems. As a consequence, the structures studied using MD are in general small in size with large surface to volume to ratios. Therefore, in order to

simulate the properties for bulk systems it is necessary to employ boundary conditions that remove free surfaces from the system thereby replicating the environment of infinite bulk surroundings for any atom inside. This is achieved by using periodic boundary condition (PBC) as shown in Figure 3-1. The simulation box is treated as the primitive cell of an infinite structure with duplicate units. Therefore, a particle will not only interact with its neighbors in the original simulation cell, but it will also interact with atoms residing in the periodic images of the original cell. The consequence of this condition are the following: (a) atoms leaving one face of the simulation cell straightaway appear from the opposing face with identical momentum, and (b) atoms within the cut-off distance of a simulation box boundary interact with atoms near the opposing faces of the simulation box.

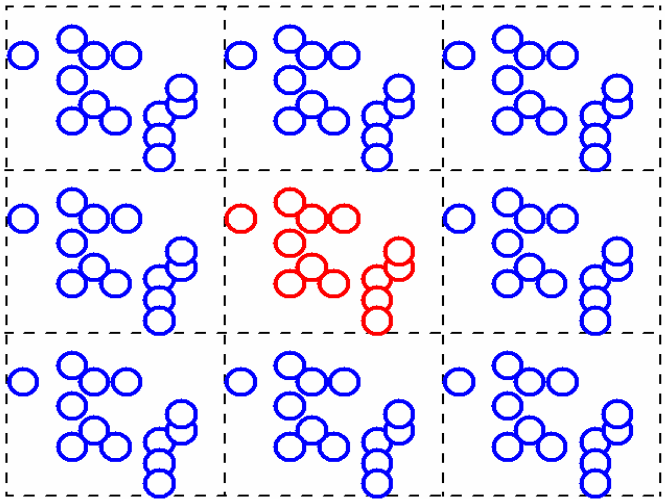

Figure 3.1: Illustration of periodic boundary condition. Atoms in the original simulation box are colored red, and their mirror images are colored blue; atoms interact across the boundaries of the simulation box.

3.6 Summary

In this section, we have introduced different aspects of MD simulations. The foundations of the velocity-Verlet algorithm implemented in LAMMPS for calculating the positions and velocities of individual atoms by integrating Newton's equation of motion is presented in Section 3.1 The value of the simulation timestep is critical to the stability of MD simulations. Section 3.2 briefly touches upon the factors which determine the choice of the timestep. The quality of the interatomic potential is central to the accuracy of the simulated results. In Section 3.3 we discussed the EAM potential and the SW potential which have been used for the simulations reported in this thesis. Details of the NH thermostat and periodic boundary conditions have been discussed in Section 3.4 and Section 3.5.

Chapter 4[1]

Simulations of linear and non-linear damping in single-crystal nickel nanoresonators

As a step towards developing methods for calculating damping using classical MD, we present a comparative study of five different methods for computing damping in a single-crystal Ni nanoresonator using an NVT ensemble. In Section 4.1 we discuss the details of the simulation methodology. The discussions include details of the structural dimensions, thermal relaxation steps, thermostat time constant, estimates of natural frequency and axial stiffness. The section ends with describing a protocol used for selecting simulation parameters such as frequency of oscillation, magnitude of harmonic force, and duration of force application to ensure precise estimates of damping in the subresonant regime. Section 4.2 is divided into two parts. In the first part we report the convergence and linearity of $\tan\phi$ and η for oscillations at 10 GHz and 30 GHz. The second half discusses the details of damping simulations in the resonant regime which includes calculations of nonlinear logarithmic decrement from the free oscillations, Q-factor from the Duffing analysis of the nonlinear amplitude- frequency response during steady-state harmonic oscillations, and also the Q-factor from the spectrum of the thermal noise.

[1] This chapter is an expanded version of the work presented in the following publication: Z. Nourmohammadi, S. Mukherjee, S. Joshi, J. Song, and S. Vengallatore (2015), "Methods for atomistic simulation of linear and nonlinear damping in nanomechanical resonators," *Journal of Microelectromechanical Systems,* vol. 24, pp. 1462-1470, 2015.

4.1 Simulation Methodology

A simulation timestep of 1 fs was chosen for the simulations. The following steps were implemented for simulating damping in a single-crystal nickel nanofilm resonator. The first step was to create the structure in LAMMPS environment. Structural dimensions were chosen considering computational constraints. Next, the atoms were equilibrated at 300 K. The NH thermostat was used for the thermal equilibration of the structure. Appropriate boundary conditions were employed depending on the method for measuring damping. This procedure was followed for all the damping simulations reported in this thesis.

4.1.1 Structural details

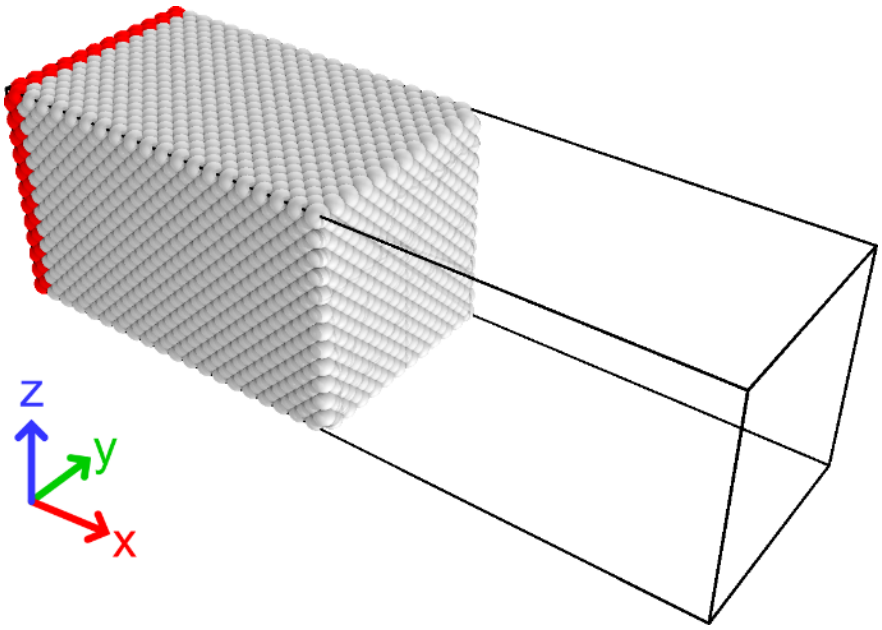

Figure 4-1: Schematic illustration of the nickel nanofilm. Clamping condition is employed by freezing the motion of the atoms colored in red.

A single-crystal Ni nanofilm was constructed by arranging atoms on a face centered cubic (fcc) lattice with a lattice parameter of 3.53 Å. A Cartesian coordinate system was attached to the structure with the *x*, *y*, and *z* axes oriented along the [1 0 0], [0 1 0], and [0 0 1] directions respectively. The dimension of the *y*-*z* cross-section was 4.2 nm × 4.2 nm and the length (l_x) along the [1 0 0]-direction was 6.75 nm. In the axial direction, the structure was clamped at one end by freezing the motion of atoms, the rest of the atoms were free to move (shown in Figure 4-1). In the lateral (*y* and *z*) directions, the boundaries were periodic.

4.1.2 Thermal equilibration

Thermal equilibration of the nanofilm was carried out using the following steps. To begin with, a random velocity was assigned to the initial configuration of the atoms and the starting temperature was chosen to be 1 K. Thereafter, the structure was equilibrated at 300 K in two stages. First the temperature of the structure was slowly increased to 300 K. This step was followed by thermal equilibration for a certain duration at 300 K.

Generally, the starting configuration of the atoms are significantly different from the equilibrated state. It is therefore necessary to perform thermalisation steps for extended lengths of time to ensure averaged quantities, such as temperature and potential energy. There is no definite rule for finding the equilibration time because it depends on several variables such as the target temperature, the type of the interatomic potential, the thermostat being used and the time constant. In general, quantities such as temperature and potential energy are monitored during the thermal relaxation process. The thermal relaxation is said to have been achieved once there are no large fluctuations in the time traces of these quantities.

The structure was evolved in time in NVT ensemble using the Nosé-Hoover (NH) thermostat. Generally, three parameters need to be selected to perform thermal equilibration, these are: (a) the time constant of the thermostat (τ_{NH}), (b) simulation time (t_{raise}) during which temperature is increased from 1 K to 300 K, and (c) the simulation time (t_{eq}) for the thermal equilibration at 300 K. Let us see, how these parameters were chosen for the nickel nanofilm. Kunal and Aluru [62] found that a τ_{NH} of 0.1 ps was suitable for simulations of damping in single-crystal Ni. We begin by examining the suitability of this selection and record the average potential energy and the average temperature as a function of simulation time.

A t_{raise} of 4 ns was selected by trial and error. The time traces of the temperature and the potential energy were monitored to ensure gradual increase in the temperature. A t_{eq} of 2 ns was also selected by trial and error to avoid fluctuations in the traces of temperature and potential energy. Figure 4-2 shows the time trace of the temperature and the potential energy in the nanofilm during the entire thermal equilibration process.

For any system evolved using an NVT ensemble, at steady-state, the kinetic energy (KE) of the atoms follow the Maxwell-Boltzmann distribution. Figure 4-3 shows the comparison of the kinetic energy distribution ($f(KE)$) for the nanofilm at steady state with the Maxwell Boltzmann distribution. The Maxwell-Boltzmann distribution of kinetic energy is given by

$$f(KE) = 2\sqrt{\frac{KE}{\pi}}\left(\frac{1}{kT}\right)^{\frac{3}{2}} \exp\left(\frac{-KE}{kT}\right) \tag{4.1}$$

The variance of the temperature fluctuations is given by

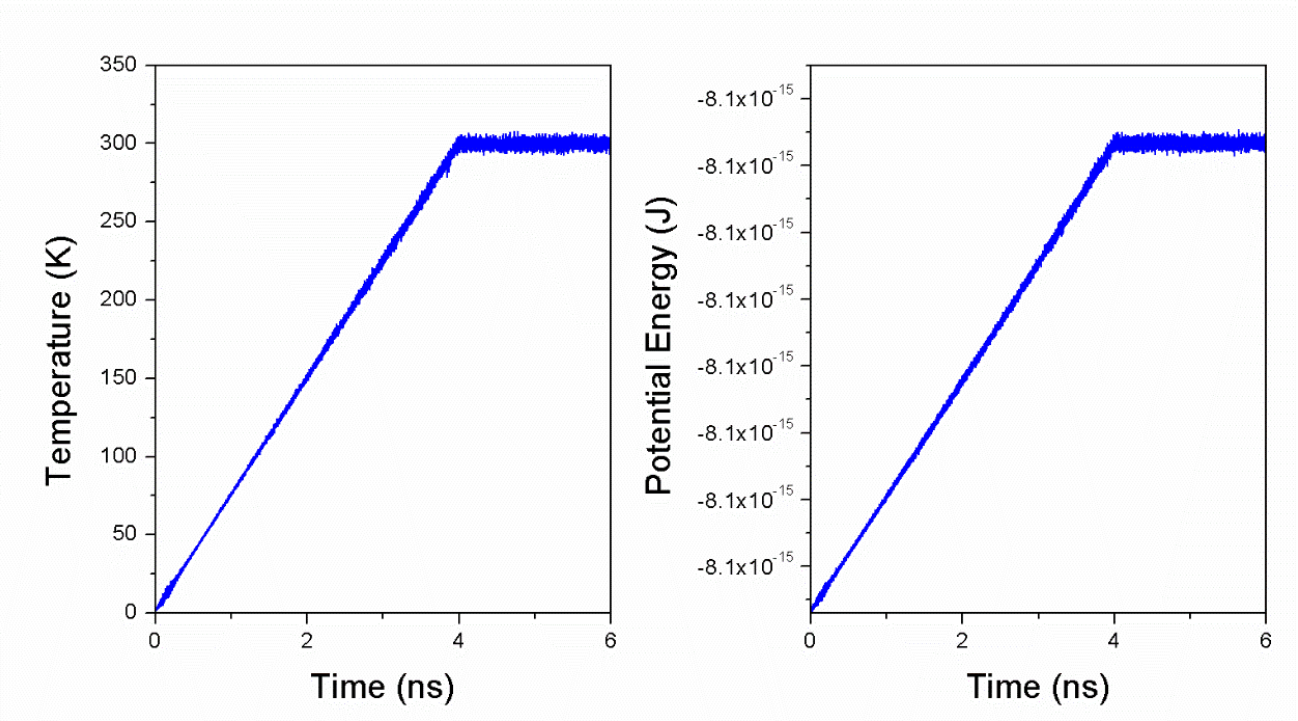

Figure 4-2: Time traces of (a) temperature, and (b) potential energy in the nickel nanofilm obtained using the NH thermostat during thermal equilibration process.

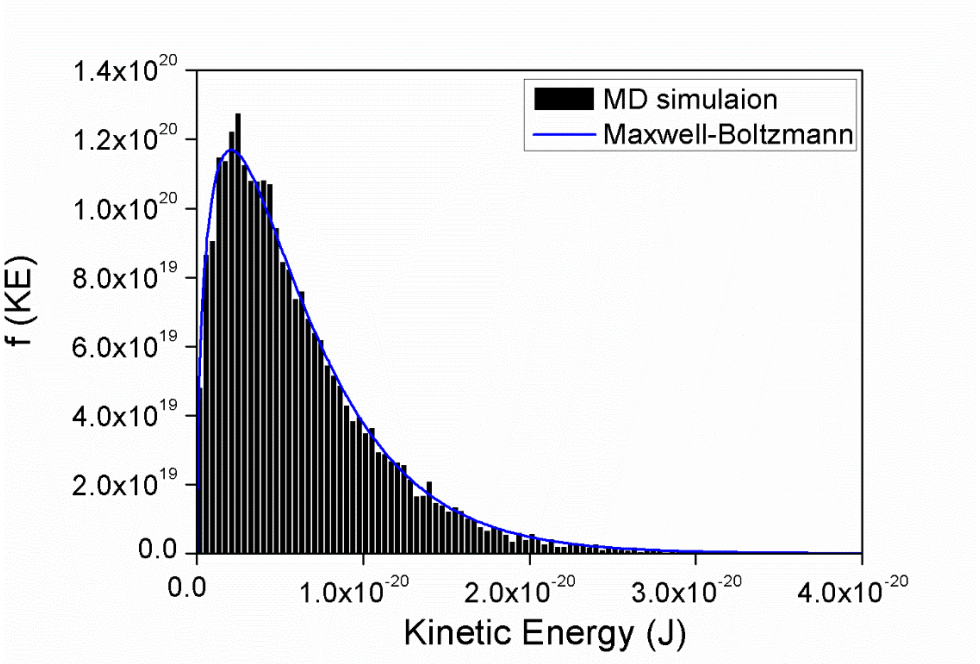

Figure 4-3: Comparison of the distribution of kinetic energy of the atoms in the nanofilm at 300 K and the Maxwell-Boltzmann distribution of kinetic energy.

$$\langle \Delta T \rangle = \sqrt{\frac{2}{d_f} \frac{\langle T \rangle^2}{N}}, \tag{4.2}$$

where $\langle T \rangle = T_0$, N is the number of particles in the system. A ΔT = 2.4 K is obtained for the nanofilm by using Eq. (4.2), which is in good agreement with a ΔT of 2.35 K obtained from the simulations.

4.1.3 Natural frequency (f_0) and mode shape

Simulations were performed to find out the fundamental natural frequency and the mode shape of the nanofilm. In NVT ensemble the system exhibits spontaneous random movements around its equilibrium position due to an injection of energy from the reservoir. These movements manifest as thermal noise. The thermal noise was acquired by recording the spontaneous axial displacements of the atomic layer at the free end ($x = l_x$). The time series of the thermomechanical noise (shown in Figure 4-4) was analyzed in the frequency domain using the Fast Fourier transform (FFT) method. The corresponding FFT plot (shown in Figure 4-5) exhibited Lorentzian peak at the natural frequency of the structure. The frequency corresponding to the first peak was 183 GHz. Since periodic boundary condition restricted the motion of the atoms in the out-of-plane directions; the first peak in the FFT therefore presented the fundamental longitudinal mode of the structure.

The mode shape for the first longitudinal mode was evaluated by applying harmonic force of 0.0001 nN with frequency 10 GHz on the free end of the structure. The motion of the atoms in different atomic layers along the length of the nanofilm were traced. Figure 4-6 shows the mode shape of the nanofilm obtained by plotting the displacement of each atomic layer from their respective equilibrium positions as a function of their positions along the length of the structure.

4.1.4 Estimation of axial stiffness (K_x)

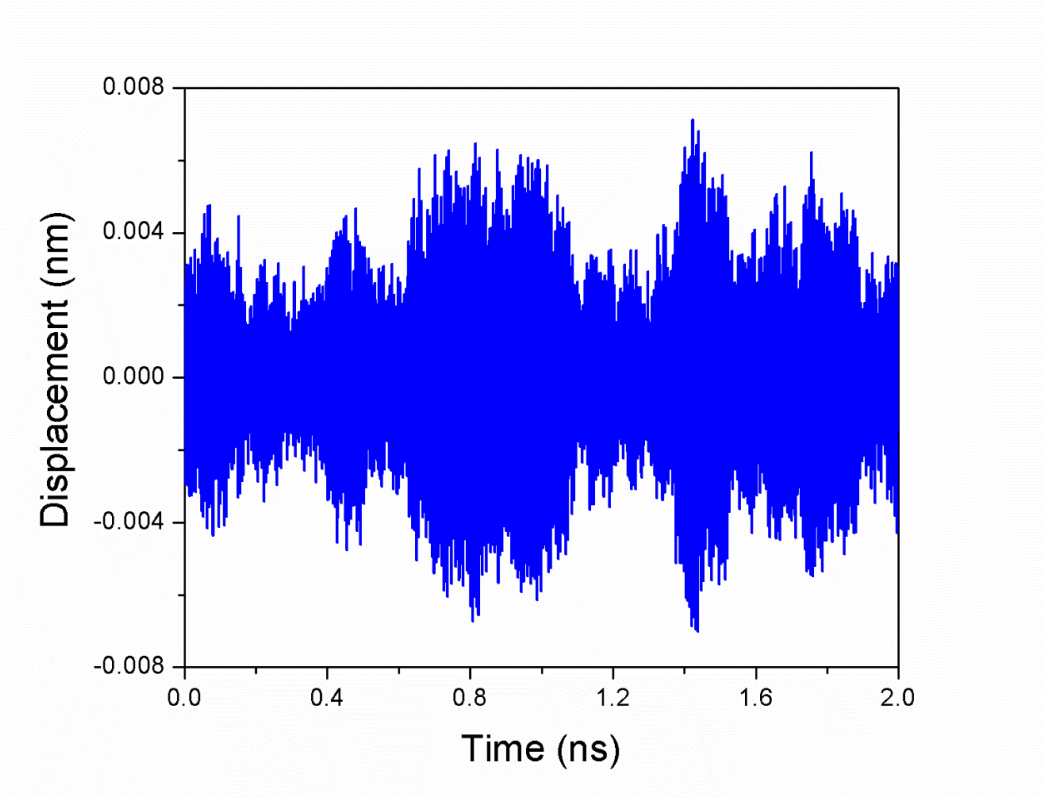

Figure 4-4: Time trace of the thermal noise captured by recording the motion of the free layer.

In the elastic domain, stiffness is defined as the resistance exerted by a mechanical structure to an external force. The axial stiffness (K_x) of the nanofilm was evaluated by performing simple tensile tests. Static forces of varying magnitudes were applied on the atoms in the end layer ($x = l_x$) and the motion of the forced atoms were monitored. Figure 4-7 (a) shows the force-displacement relationship in the nanofilm. The corresponding stress-strain data is plotted in Figure 4-7 (b). It can be seen that the nanofilm behaved linearly till a stress of 5 GPa which corresponds to a force of 92 nN. A straight line was fit to the linear part of the response using the least square algorithm.

The slope of the line is the stiffness of the structure, which in the case of the nanofilm was 555.2 N/m. The coefficient of regression exceeded 0.99.

For a beam stretched by pure axial load, the axial stiffness is given by [62],

$$K_x = \frac{ES}{l_x}. \tag{4.3}$$

Eq. (4.3) gives a stiffness of 535 N/m for the nanofilm which is in agreement with our estimates of stiffness using MD simulations.

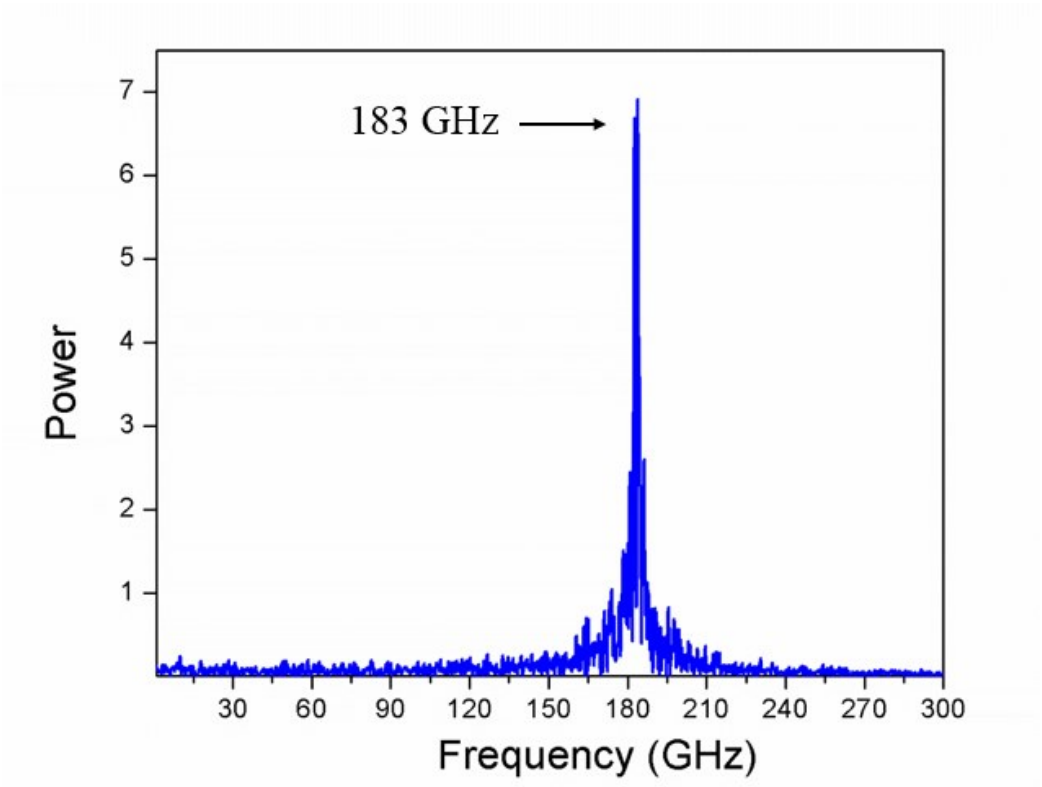

Figure 4-5: FFT of the displacement noise in the nanofilm. The peak at 183 GHz represents the fundamental longitudinal mode.

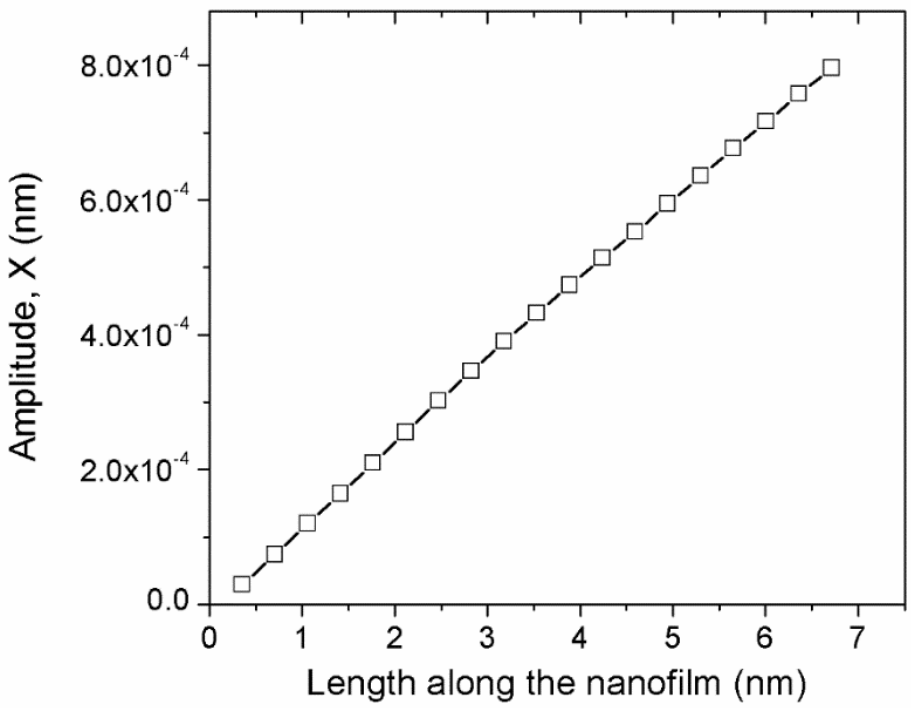

Figure 4-6: Mode shape of the nanofilm during harmonic longitudinal oscillations for applied force 0.0001 nN and frequency 10 GHz.

4.1.5 Protocol for estimating damping in the subresonant regime

In the subresonant regime damping was estimated using the loss factor (η) and the loss tangent ($\tan\phi$). An axial harmonic force, $F_0 \sin(2\pi ft)$, was applied at the free end of the nanofilm at $x = l_x$ to excite longitudinal oscillations at frequencies less than the resonance frequency. The velocity and the displacement of the forced atoms were recorded after each simulation time step. The magnitude of $\tan\phi$ was estimated by calculating the phase of the applied force and the response using the FFT algorithm distributed with MATLAB. The magnitude of η was calculated using Eq. (2.9). ΔW was calculated by numerically integrating the velocity and the applied force using

Eq. (2.10). W was calculated by plugging in the values of K_x and the amplitude of oscillation into (Eq. 2.12). The amplitude of oscillation was given by

$$A_x(f) = 2 \times \left(\frac{FFT(x_{data})}{n_{data}} \right), \tag{4.4}$$

where x_{data} is the time-series of the average displacement of atoms at the free end, and n_{data} is the number of data points used for calculating the FFT.

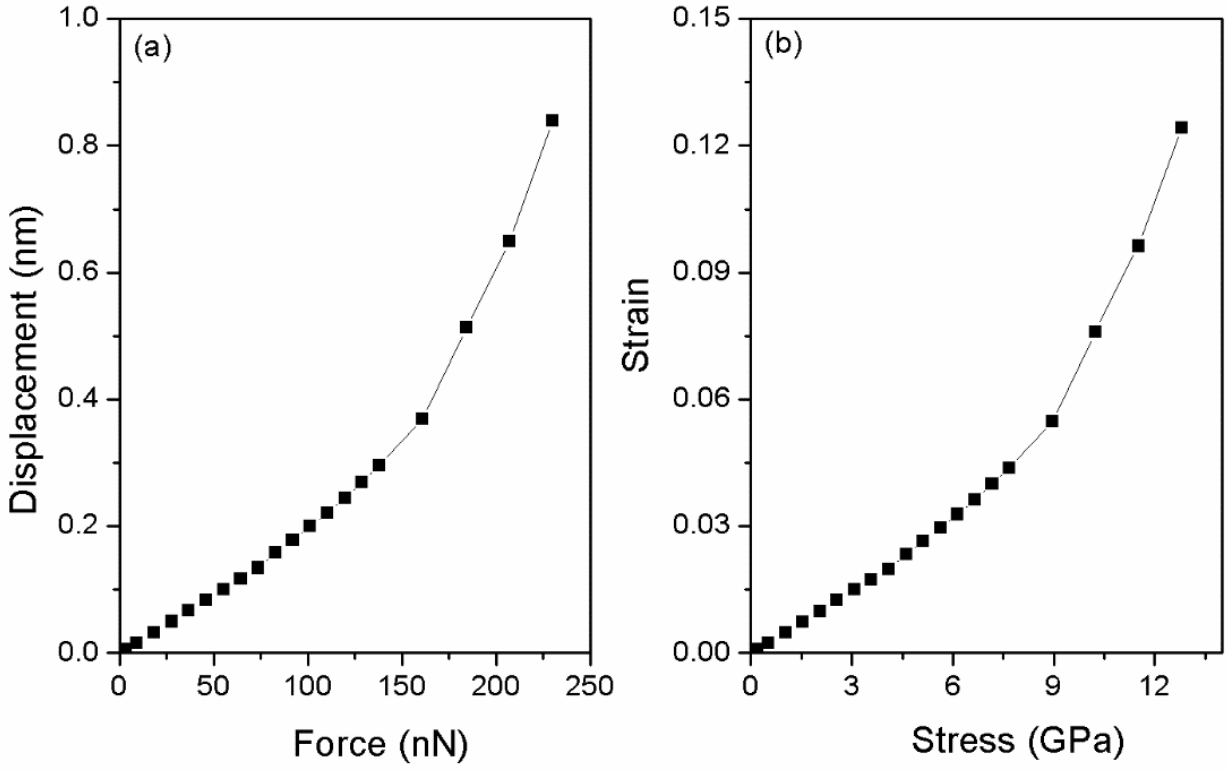

Figure 4-7: (a) Force-displacement, and (b) stress-strain curves for the nanofilm used for estimating the axial stiffness and Young's modulus using a linear least-squares analysis. The coefficient of regression exceeded 0.99.

In the beginning, the application of the harmonic force caused an impulse response in the nanofilm. This behavior necessitated identification of the steady state response regime. Data from the transient regime was discarded and $\tan\phi$ and η were calculated using the steady-state oscillation data. In order to find out the onset of steady state vibration, the motion of the free end of the structure was analyzed as a function of time. Figure 4-8 shows this behavior in the nanofilm while the structure was undergoing forced harmonic oscillations at 10 GHz for various magnitudes of F_0. An initial transient duration of 2 ns was discarded as transient vibration.

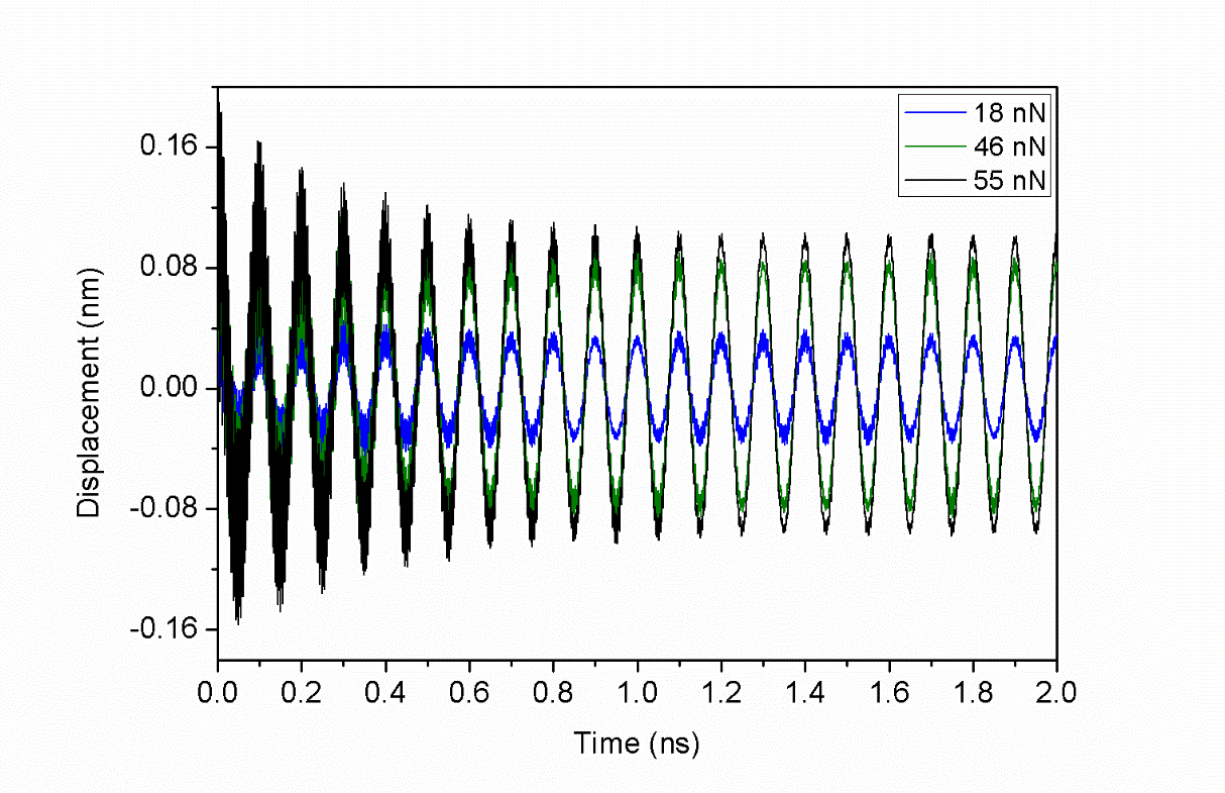

Figure 4-8: Axial displacement of the free end of the nanofilm as a function of time while oscillating at 10 GHz. The black green, blue colors correspond to force amplitudes of 55 nN, 46 nN, and 18 nN respectively.

For precise evaluation of $\tan\phi$ and η, three simulation inputs needed to be selected. These are: (a) frequency of oscillation (f), (b) magnitude of the applied harmonic force (F_0), and (c) the duration of the time harmonic oscillations (t_f). In the next section, we discuss the rationale behind the selection of these inputs. The optimal values of the simulation parameters were identified by devising a protocol consisting of the following four steps.

Step 1: Selection of the frequency

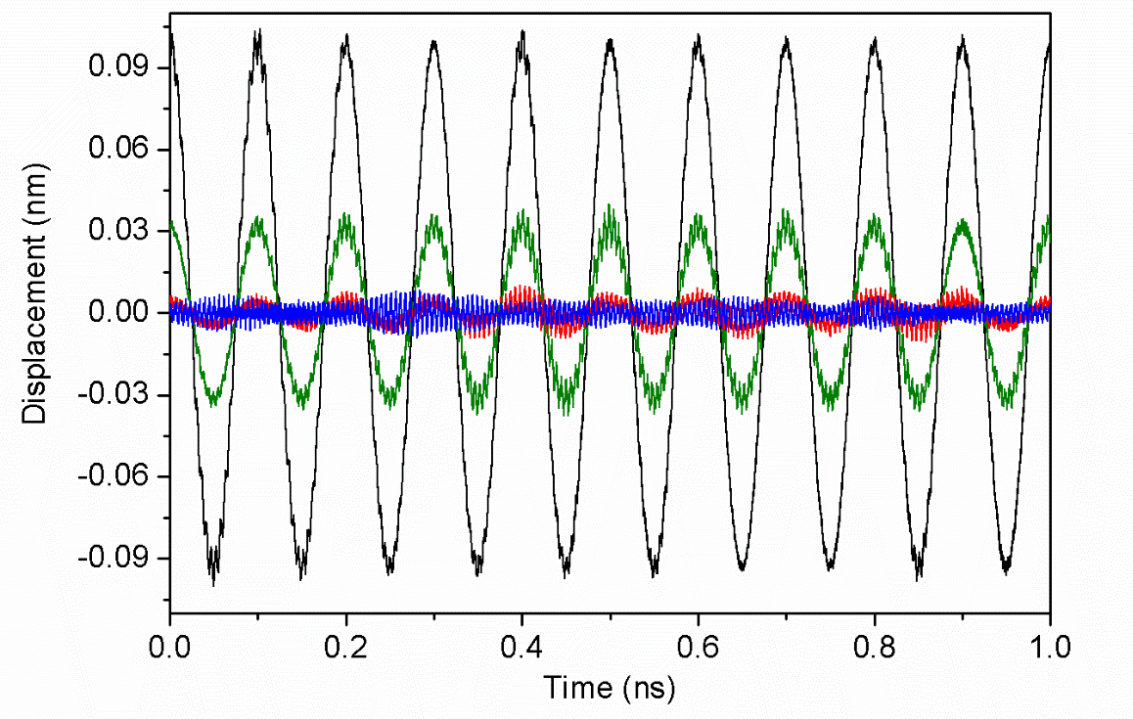

Figure 4-9: Axial displacement as a function of time at the free end of the nickel nanofilm at 10 GHz. The blue curve shows the thermomechanical noise. The red, green, and black curves show the response when the structure is driven harmonically with force amplitudes of 2 nN, 18 nN, and 55 nN, respectively.

The first step was to decide the frequency range over which the damping simulations were to be performed. The lower bound of frequencies depended on the limitations of computational

resources. For all the simulations, the lower limit of the frequency of operation was selected to be 1 GHz. On the other hand, the upper limit of frequency was dictated by the response of the structure close to the resonance frequency. The upper bound of frequency was selected to be 30 GHz to ensure linear response of the structure.

Step 2: Finding the magnitude of the harmonic force (F_0)

The magnitude of the harmonic force was selected by considering the linearity of oscillations and the magnitude of the thermomechanical noise floor. The selected magnitude of F_0 was small to ensure linear oscillations, but sufficiently large so that the harmonic response was significantly larger than the thermal noise floor.

Figure 4-9 illustrates the response of the nanofilm undergoing harmonic oscillations in the steady state at 10 GHz for varying loads. In the absence of the harmonic force, the response was entirely due to thermomechanical noise with a root mean square (rms) value of $\sqrt{k_B T / K_x} = 3.12 \times 10^{-3}$ nm. A F_0 of 2 nN was selected as the lower limit of the force as it produced harmonic response larger than the thermal noise floor.

The magnitude of the harmonic force was chosen such that the material behaved in the linear regime. This was ensured by studying the stress-strain response of the nanofilm obtained from the simple tensile tests mentioned in Section 4.1.4. For a linear material response the stress-strain plot should produce a straight line. The stress-strain behavior in the nanofilm for a range of static loads is presented in Figure 4-7 (b). Linear material behavior was observed for forces below 92 nN.

Step 3: Confirm convergence

Displacement of a structure oscillating at subresonant frequencies can be classified into three regimes: fluctuation-dominated response, linear mechanical response, and non-linear mechanical response. These regimes can be observed in the response of the sample in Figure 4-9. For large forces, the harmonic amplitude surpasses the thermomechanical fluctuations and the displacement is dominated by the mechanical response. For comparatively small forces (F_0 = 2 nN), the harmonic response is comparable to the thermomechanical noise. And in the absence of harmonic force (F_0 = 0 nN), the response is completely due to thermal noise. As a consequence of this behavior thermal fluctuations have profound effect on the magnitude of damping in the subresonant regime.

The fluctuation theorem dictates that for responses comparable to the fluctuation dominated region, the analysis of damping must account for fluctuations in thermodynamic quantities such as entropy, work done, heat, internal energy, and dissipation. The steady-state Work Fluctuation theorem for harmonically oscillating structures is expressed as [139]

$$\frac{1}{\Sigma_\tau}\frac{p(\Delta W_\tau)}{p(-\Delta W_\tau)} = \exp\left(\frac{\Delta W_\tau}{k_B T}\right), \tag{4.5}$$

Where p is the probability distribution function, τ is the time interval over which the work is calculated, and Σ_τ is a dimensionless parameter that takes care of finite-time effects.

Following implications can be derived from Eq. (4.5). For example, based on the statistical properties of the work distribution, there is a finite probability of observing trajectories for which the work done is negative. Therefore, from the viewpoint of estimating damping using classical

MD, it is best to avoid the fluctuation-dominated regime and focus on the mechanical regime. Therefore, for obtaining precise estimates of damping, convergence of $\tan\phi$ and η was considered as a function of simulation time.

To this end, a series of harmonic forces were applied on the atoms in the end atomic layer with frequencies of 10 GHz and 30 GHz. Convergence data was obtained by calculating $\tan\phi$ and η for every nanosecond of forced oscillation. We defined convergence time, t_c, as the forced oscillation duration after which $\tan\phi$ and η reached a value that did not vary by more than 3%. Damping is estimated by calculating the average of the values of $\tan\phi$ and η over the time from t_c to t_f.

Step 4: Check for linearity

The final step was to check for the linearity of the estimated damping. According to Eq. (1.1) for small magnitude of damping, in the absence of material nonlinearities $\tan\phi$ and η are equivalent. Taking into consideration the propensity of numerical errors inherent to the MD algorithm, uncertainties in the simulated estimates of axial stiffness (K_x), and the influence of thermal fluctuations on the dynamics of oscillations, the estimated damping values were said to be linear when $\tan\phi$ and η differed by less than 5%.

4.2 Results

This section presents damping estimates for the Ni nanofilm at subresonant and resonance frequencies obtained using different measures of damping.

4.2.1 Damping in the subresonant regime

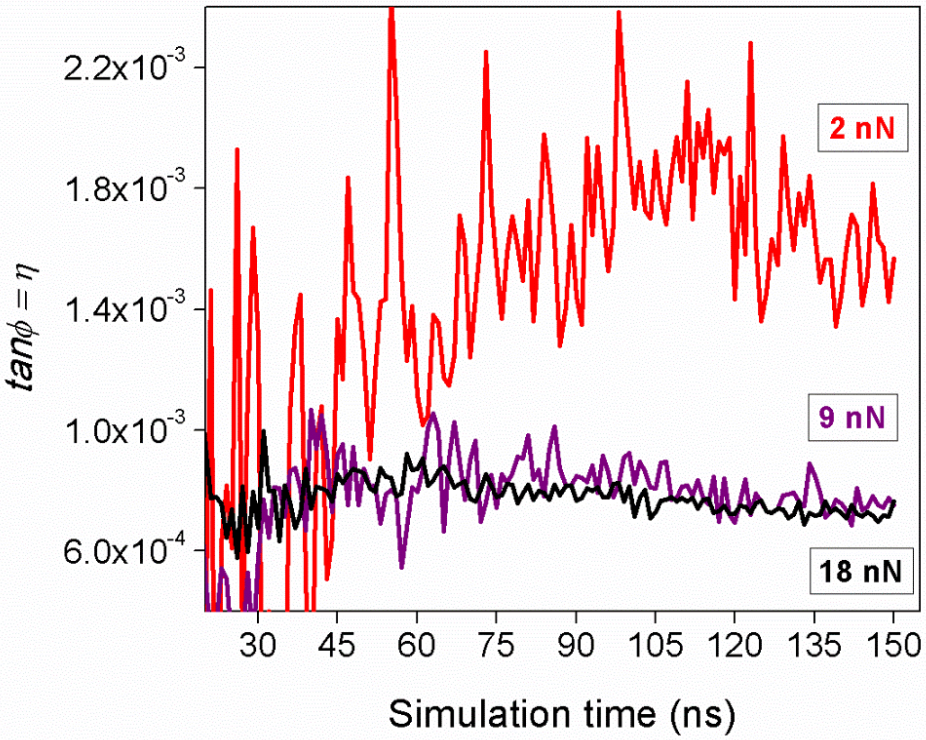

Figure 4-10: Convergence behavior of damping for longitudinal-mode oscillations at 10 GHz in the nickel nanofilm. Different curves represent damping computed after every nanosecond for: F_0 = 2 nN, (red), F_0 = 9 nN (violet), and F_0 = 18 nN (black). The maximum difference between $\tan\phi$ and η was less than 5%.

Damping in the nanofilm in the subresonant regime was estimated by calculating $\tan\phi$ and η over the frequency range of 10 GHz and 30 GHz. At each frequency, the convergence behavior and linearity of $\tan\phi$ and η were considered for a series of harmonic forces. The convergence behavior of damping values varied significantly depending on the relative strength of oscillation amplitude and the thermal fluctuations. For very small forces, when the harmonic response is

comparable to the rms value of thermal noise, the damping measures converged sluggishly. Further, as the magnitude of force was increased, $\tan\phi$ and η converged faster, in the linear regime to an average value. For very large values of harmonic force, material nonlinearities gradually became significant, and $\tan\phi$ and η ceased to become equivalent. The results were interpreted using the fluctuation theorem and nonlinear material behavior. Simulation parameters were identified for accurate estimation of damping.

4.2.1.1 Response at 10 GHz

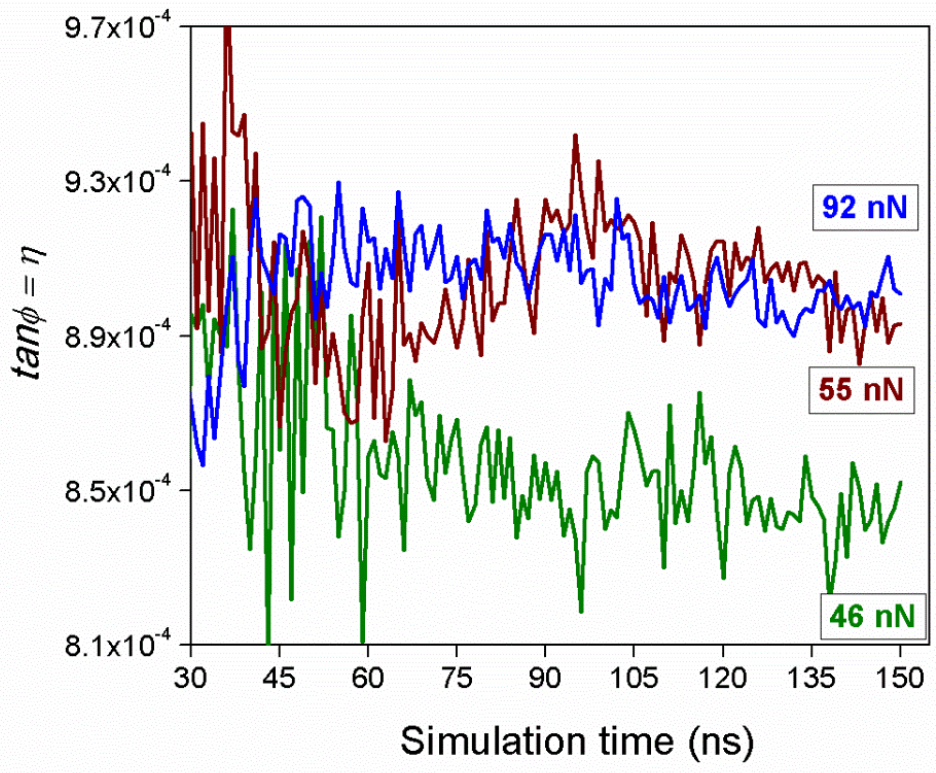

Figure 4-11: Trend of $\tan\phi$ and η in the nickel nanofilm while oscillating in the longitudinal-mode at 10 GHz. Different colors represent the damping computed after every nanosecond of oscillations for: $F_0 = 46$ nN (green), $F_0 = 55$ nN (brown), and $F_0 = 92$ nN (blue). The maximum difference between $\tan\phi$ and η was less than 5%.

Harmonic forces of magnitude in the range 2 nN and 230 nN and frequency 10 GHz were applied at the free end of the nanofilm. This range of the harmonic force covered both the linear and the nonlinear material behavior regime (see Figure 4-7).

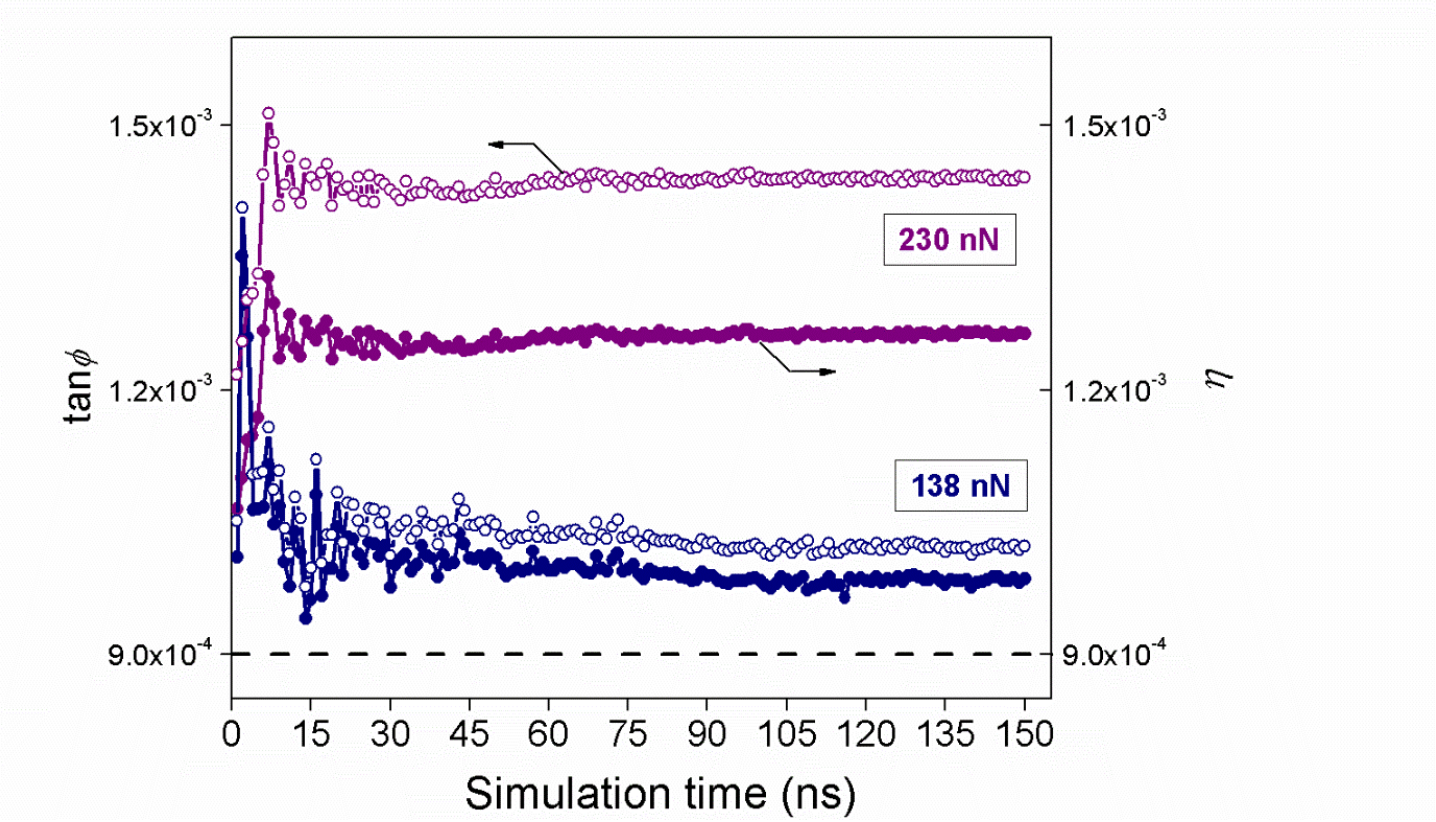

Figure 4-12: Trend of $\tan\phi$ and η in the nickel nanofilm while oscillating in the longitudinal-mode at 10 GHz. Different colors represent the damping computed after every nanosecond of oscillation for: $F_0 = 138$ nN (blue), $F_0 = 230$ nN (violet). The dashed line represents the represents the converged limit for linear damping.

Fig. 4-10 and 4-11 demonstrate the difference in the behavior of $\tan\phi$ and η between the fluctuation dominated regime and the linear mechanical regime. For small harmonic forces (2 nN and 18 nN), the time series of $\tan\phi$ and η showed wild fluctuations and did not converge after forced oscillations for 150 ns. These forces were excluded from further analysis. As the magnitude

of the force was increased (Figure 4-11), i.e. forces in the range 46 nN and 92 nN, the trend of $\tan\phi$ and η converged faster. For the harmonic force of 55 nN, $\tan\phi$ and η converged to a value of 9×10^{-4}.

As the magnitude of the force was further increased beyond 92 nN till 230 nN, the material was driven into nonlinear regime. As a consequence, the equivalence of $\tan\phi$ and η was no longer observed (the difference between $\tan\phi$ and η became 14%). However both $\tan\phi$ and η converged faster to values larger than 9×10^{-4}. This behavior is illustrated in Figure 4-12.

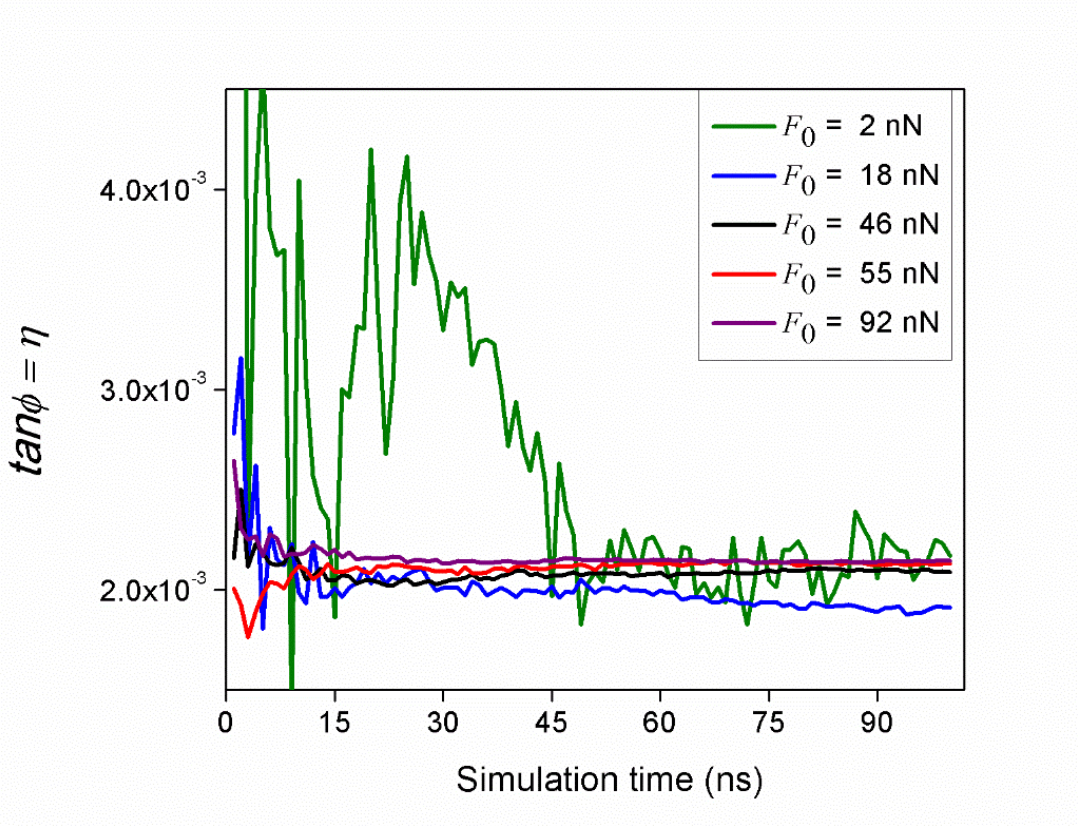

Figure 4-13: Trend of $\tan\phi$ and η in the nickel nanofilm while oscillating in longitudinal-mode at 30 GHz for five different harmonic forces. The maximum difference between $\tan\phi$ and η was less than 5%.

4.2.1.2 Response at 30 GHz

Figure 4-13 shows damping in the nanofilm for oscillations at 30 GHz calculated after each nanosecond for a total of 100 ns. For further elucidation, this plot is separately shown in Figure 4-14 and 4-15. Figure 4-14 shows the convergence results for $\tan\phi$ during oscillations at 30 GHz corresponding to small forces (2 nN and 18 nN). It can be seen that similar to the damping at 10 GHz, $\tan\phi$ is sluggish in converging towards a mean value. Therefore these forces were discarded from further analysis. As the magnitude of the force was increased further (see Figure 4-15) e.g., 55 nN, $\tan\phi$ and η converged to a value of 2.1×10^{-3}, meeting the criteria for linear damping described earlier.

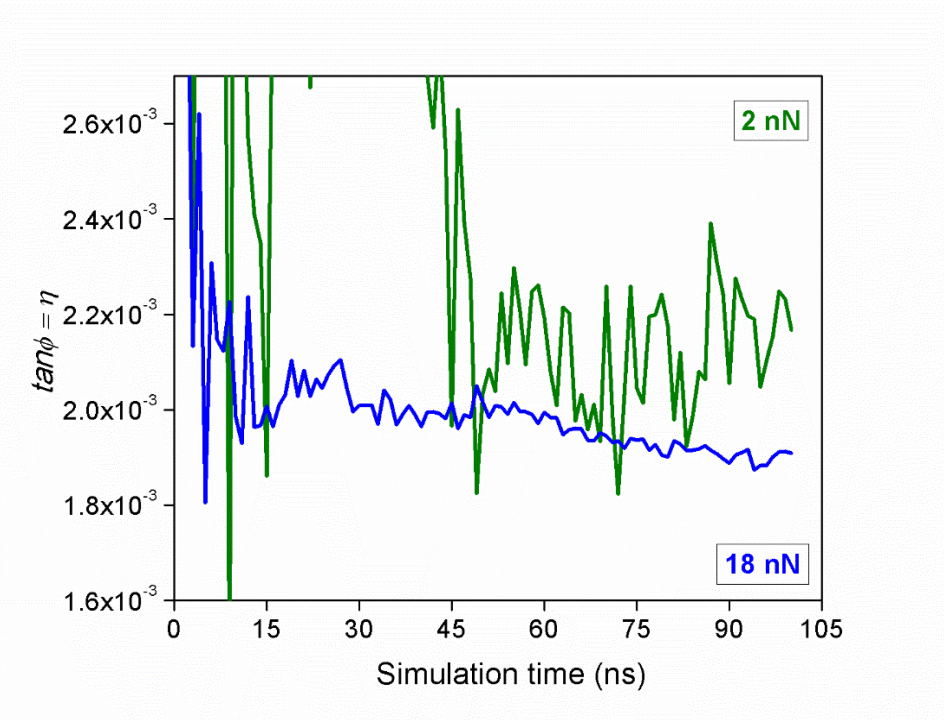

Figure 4-14: Trend of $\tan\phi$ and η in the nickel nanofilm while oscillating in longitudinal-mode at 30 GHz. Different colors represent damping computed after every nanosecond of oscillation for $F_0 = 2$ nN (green), $F_0 = 18$ nN (blue). The maximum difference between $\tan\phi$ and η was less than 5%.

4.2.1.3 Summary of converged results of damping in the subresonant regime

Table 4.1 lists the full set of results for linear damping at room temperature for the longitudinal-mode oscillations of the nickel nanofilm in the frequency range of 10 GHz to 30 GHz. The magnitude of the harmonic force was chosen to be 55 nN for calculating damping at all the frequencies.

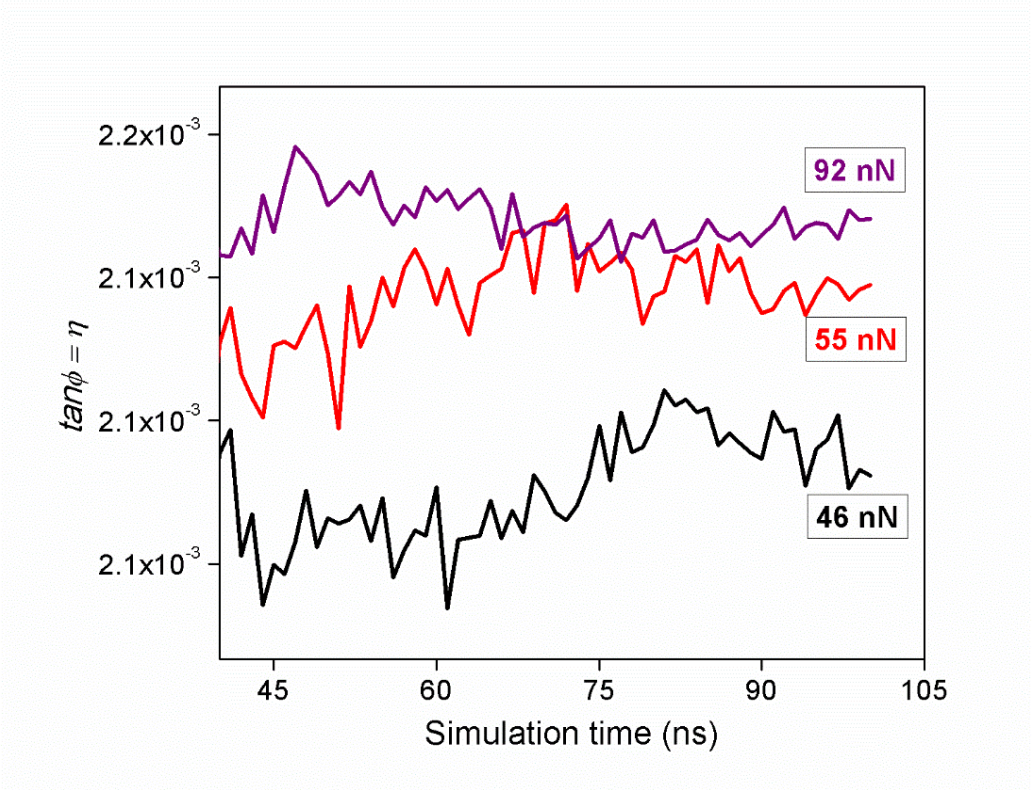

Figure 4-15: Trend of $\tan\phi$ and η in the nickel nanofilm while oscillating in longitudinal-mode at 30 GHz. Different colors represent the damping computed after every nanosecond of oscillation for: $F_0 = 46$ nN (black) , $F_0 = 55$ nN (red), and $F_0 = 92$ nN (violet). The maximum difference $\tan\phi$ and η was less than 5%.

4.2.2 Damping in the resonant regime

Linear, continuous systems, undergoing steady-state harmonic oscillations show peaks at the resonant frequencies in the frequency-amplitude curves. The Q-factor at the resonance frequency

can be obtained by fitting the spectrum of amplitude to a Lorentzian function. Similarly, in case of thermal noise, the peak corresponding to the fundamental natural frequency can be fit to a Lorentzian function to obtain the Q-factor. Additionally, the system can be excited harmonically to reach steady-state and the free vibrations can be studied in the time domain to obtain the logarithmic decrement, δ at the resonance frequency. In this section we discuss how damping in the nanofilm was estimated at the resonance frequency using the above-mentioned damping measures.

Our simulations showed that the nanofilm behaved nonlinearly when harmonic forces were applied at frequencies in the vicinity of the resonance frequency. This behavior in the presence of the thermomechanical noise made it difficult to assess the linear range. Furthermore, the frequency response displayed the characteristic signatures of Duffing-like nonlinearity, as also observed in experimental studies of nonlinear damping in nanomechanical resonators [1].

Table 4.1: Damping in the Ni nanofilm at 300 K for the longitudinal mode oscillations.

Frequency (GHz)	Force, F_0 (nN)	Convergence time, t_c (ns)	$\tan\phi$	η	$\frac{\tan\phi-\eta}{\tan\phi}\times 100$
10	55	107	8.55×10^{-4}	8.95×10^{-4}	4.6
15		44	12.03×10^{-4}	12.56×10^{-4}	4.4
20		35	14.91×10^{-4}	15.51×10^{-4}	4.0
25		15	18.14×10^{-4}	18.76×10^{-4}	3.4
30		15	20.34×10^{-4}	20.88×10^{-4}	2.6

4.2.2.1 Logarithmic decrement, δ

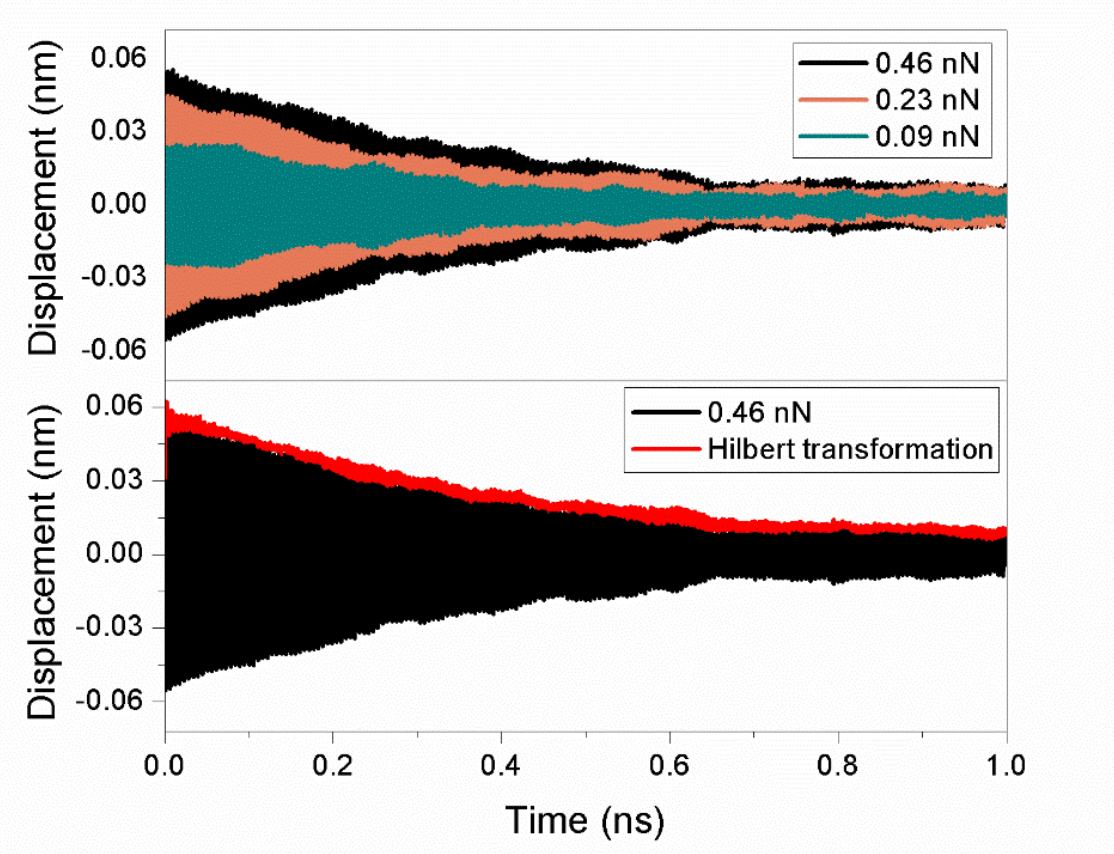

Figure 4-16: (a) Free decay plots for the nanofilm for a range of harmonic excitations. The black, yellow and green color represent free decays obtained using harmonic excitation of forces 0.46 nN, 0.23 nN, and 0.09 nN respectively. (b) Hilbert transformation represented by the red line, superimposed on the free decay obtained using harmonic force of 0.46 nN.

Linear freely decaying structures vibrate at the resonance frequency, and reduce amplitude by dissipating useful mechanical energy as heat. The decay envelop can be fit to Eq. (2.21) to calculate δ. The following steps were implemented to obtain the free decay of the nanofilm and calculate δ from the envelop function.

(1) First the thermally equilibrated structure was oscillated harmonically at the resonance frequency (i.e. 183 GHz). The harmonic force was chosen such a way that the steady-state

response surpassed the thermal noise floor, but was smaller than the elastic limit of the structure.

(2) Once the structure started oscillating at the steady-state, the harmonic force was removed, and the structure was allowed to decay freely.

(3) The motion of the end atomic layer ($x = l_x$) of the nanofilm was recorded during the free vibration.

Figure 4.16 (a) represents the decay envelop of the nanofilm obtained using harmonic forces of magnitude 0.46 nN (black), 0.23 nN (yellow), 0.09 nN (green). As a check to assess linearity, the instantaneous decay frequency and δ were calculated for different segments of the decay in the time domain, each of 0.03 ns in duration, using FFT and Hilbert transformation. Figure 4-16 (b) represents the Hilbert transformation of the decay envelop corresponding to an initial excitation of 0.46 nN obtained using Eq. (2.20), also super imposed in the same plot is the time trace of the actual decay.

As shown in Figure 4-17 (a), the instantaneous decay frequencies in the nanofilm were not identical for different decay segments for all the harmonic excitations. This behavior is a signature of the underlying nonlinear dynamics. The range of the decay frequency was between 180 GHz and 186 GHz. Also, as shown in Figure 4-17 (b) the magnitude of δ also varied for different decay segments depending on the amplitude of initial excitation. For the full decay duration of 1 ns, the average log decrement was found to be 0.015, which is equivalent to a Q-factor of 210 obtained using Eq. (1.1).

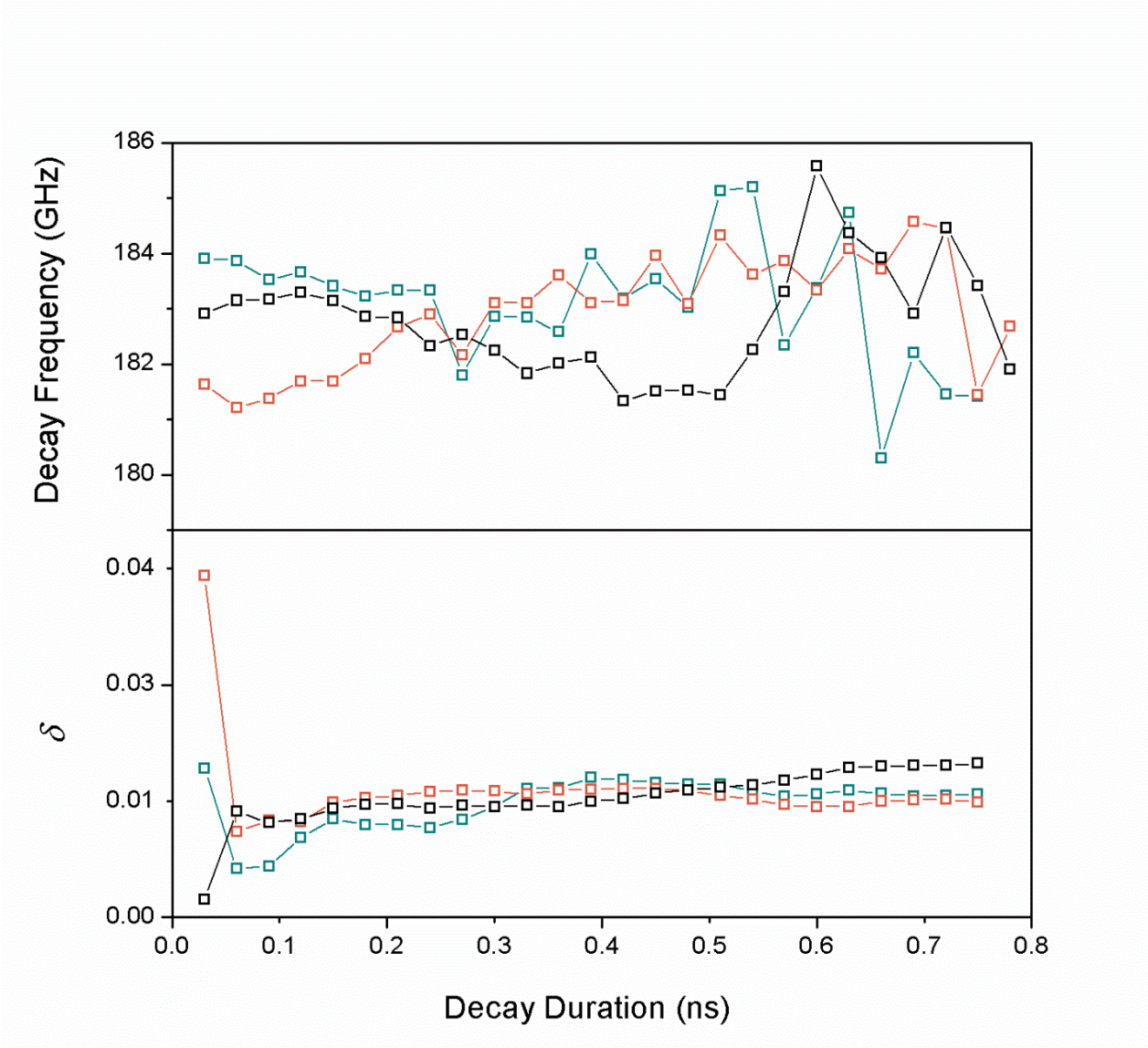

Figure 4-17: Plots of instantaneous decay frequency and δ obtained using the FFT method and the Hilbert transformation of the decay envelops corresponding to harmonic excitations of 0.46 nN (black), 0.23 nN (orange) and 0.09 nN (green).

4.2.2.2 Q-factor from harmonic oscillations

In order to calculate the Q-factor, first, the thermally relaxed structure was harmonically oscillated at frequencies around the first longitudinal resonance frequency by applying forces at its free end.

The magnitude of the harmonic forces were selected smaller than 92 nN, in order to avoid material nonlinearities (see Figure 4-7). The amplitude of the steady-state oscillations was calculated using Eq. (4.4).

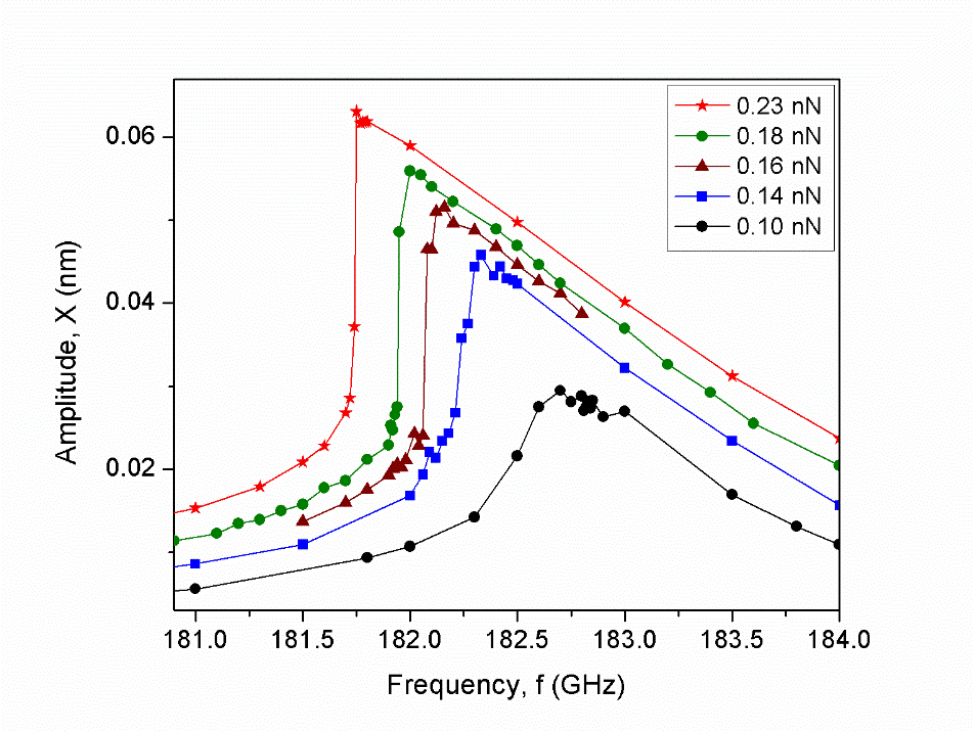

Figure 4-18: Frequency response curves of the nanofilm during steady-state longitudinal oscillations for varying magnitudes of harmonic forces.

Figure 4-18 shows the steady-state harmonic amplitudes of the nanofilm for a range of harmonic forces around the natural frequency. It can be seen that the frequency corresponding to the maximum amplitude is not constant and as the magnitude of the force is increased the peak shifts towards lower frequencies showing signatures of nonlinear spring softening. Consequently, Eq. (2.22) is not valid for calculating the Q-factor.

Therefore, in order to calculate the Q-factor, we checked whether the nonlinear behavior showed signatures of Duffing-like oscillators. In order to confirm this behavior we identified critical amplitude, A_c, defined as the first amplitude among the set of nonlinear curves that displays infinite slope as 0.04 nm. This observation quantitatively agreed with a magnitude of 0.033 nm for A_c obtained using Eq. (2.27). The back-bone curve shown in Figure 4-19 was fit to Eq. (2.29) to obtain, $Q = 215$, and $f_0 = 183$ GHz.

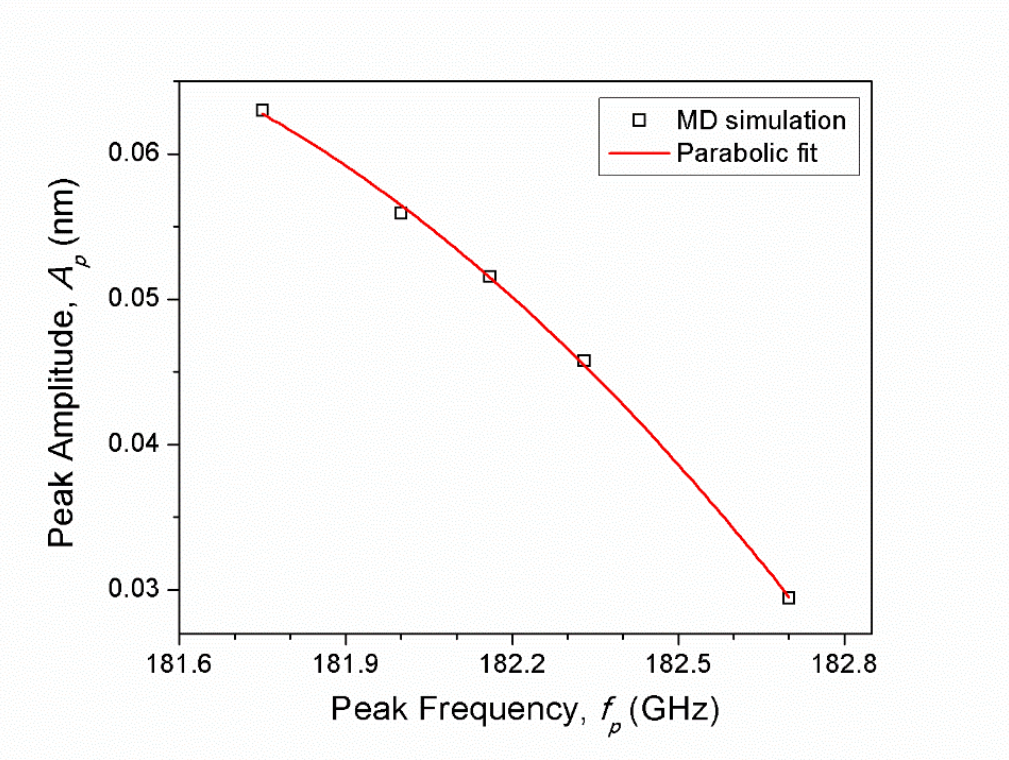

Figure 4-19: Fit to the backbone curve using Eq. (2.29). The fit gives $f_0 = 183$ GHz and $Q = 215$.

Figure 4-20 shows the amplitude frequency curve obtained directly from MD simulations and superimposed in the same plot is the simulated amplitude-frequency curve obtained using Eq. (2.26) for $Q = 215$, and $f_0 = 183$ GHz.

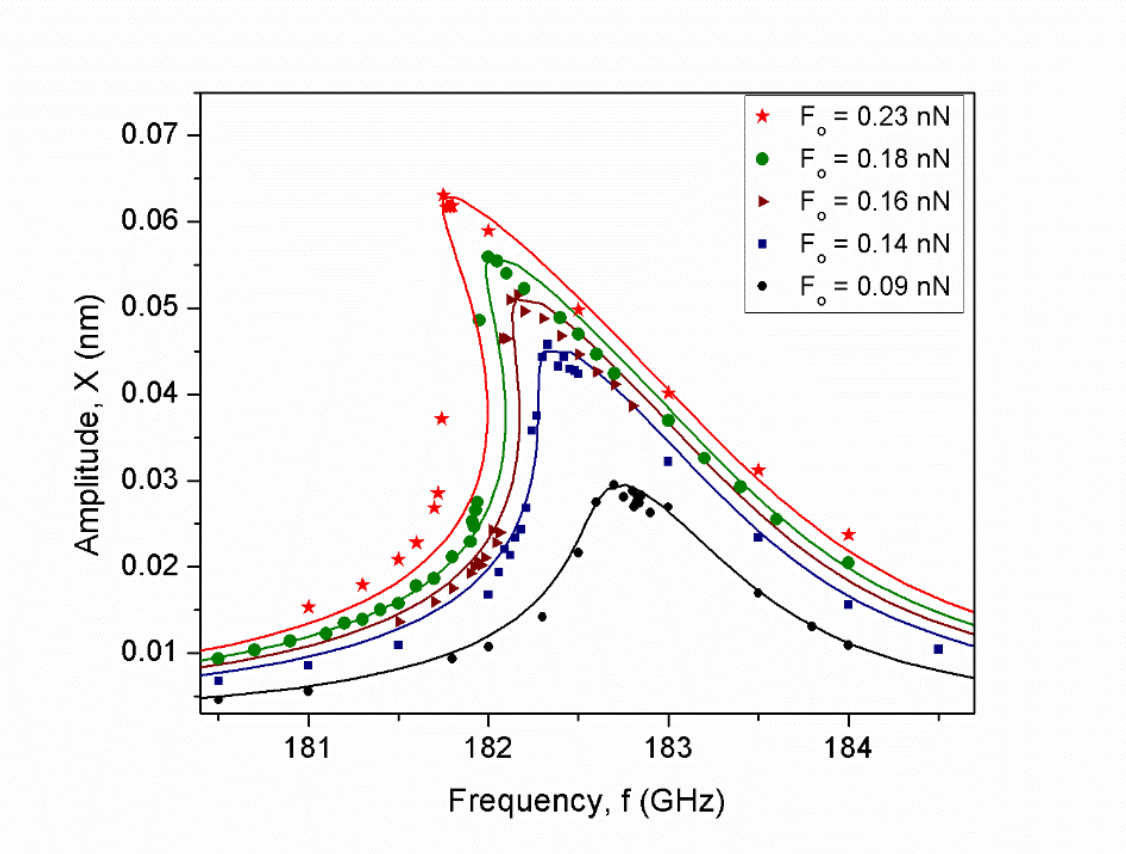

Figure 4-20: Nonlinear frequency response for the nickel nanofilm. The symbols are the results of simulations and the curves were computed using Eq. (2.26) with $A_c = 0.04$ nm, $Q = 215$, and $f_0 = 183$ GHz.

4.2.2.3 Q-factor from thermal noise

Figure 4-21 shows the PSD of the thermomechanical noise of the atoms at $x = l_x$ captured for a total simulation time of 154 ns. The simulation time step of 1 fs correspond to a Nyquist frequency (that is, one-half of the sampling frequency) of 5×10^5 GHz which is significantly larger than the fundamental natural frequency of the structure. The PSD of the displacement noise was computed using the Welch's methodology built-into MATLAB [140]. The first resonance peak located at 183

GHz corresponded to the first longitudinal mode. The remaining peaks were from the resonance frequencies of the higher modes.

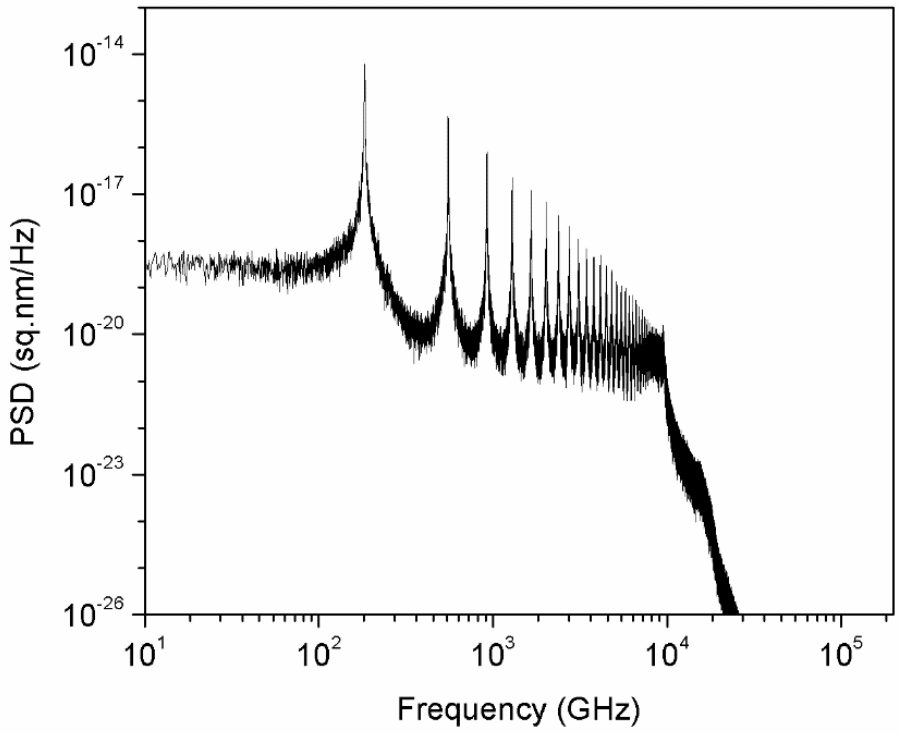

Figure 4-21: Power spectral density (PSD) of the displacement noise captured for 154 ns for the nickel nanofilm calculated using the Welch method. The peaks in the PSD represent resonant modes in the longitudinal modes in the longitudinal direction.

In order to calculate the Q-factor, the entire noise data was divided into 5 equal segments, each 29 ns in duration. The peak at 183 GHz was fit to the Lorentzian function given by Eq. (2.23). A zoomed in view of the peak at 183 GHz is shown in Figure 4-22, also shown in red color is the Lorentzian fit to the PSD. The fit was performed by using the least squares algorithm. The frequency band width for the fit was guessed by trial and error by looking at the shape of the peak. A weighted fit was performed using the Levenberg-Marquardt algorithm [141], built into the

software ORIGINLAB. This was done to ensure that all the points in the PSD had equal contribution. It can be seen that the fitted Lorentzian captured the PSD spectrum of the thermomechanical noise which is a signature of linear vibration. Therefore, the Q-factor was computed by plugging in computed fit parameters into Eq. (2.22).

The estimates of Q-factor and the resonance frequency of the fundamental longitudinal mode at 183 GHz, obtained using the five noise segments are summarized in Table 4.2. The mean value of Q-factor, and σ_Q were found to be 183 and 25. The latter is in good agreement with Eq. (2.24) which predicted a standard deviation of 20.3 (i.e., 11% of the mean).

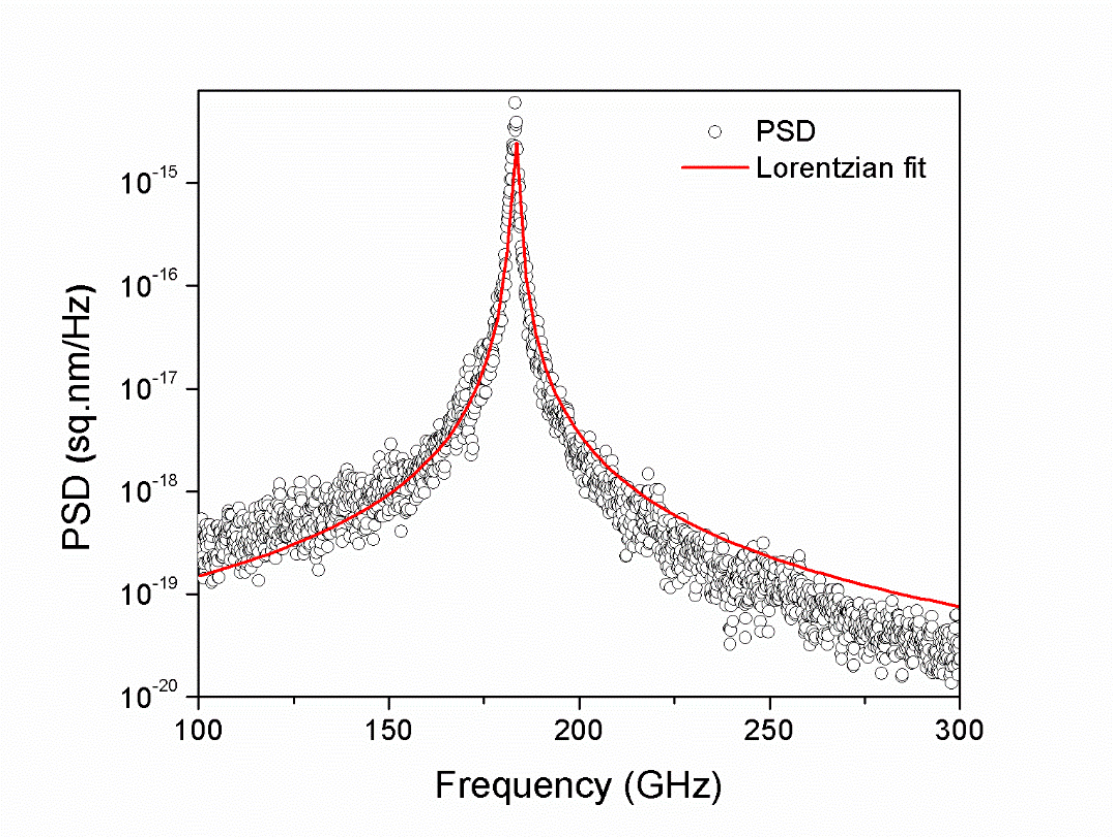

Figure 4-22: Illustration of the Lorentzian fit to PSD of the thermal noise around the primary peak corresponding to the fundamental longitudinal vibration mode. The black circles represent the calculated PSD and the red color represent the Lorentzian fit.

Table 4.2: Estimates of Q-factor and f_0 from the Lorentzian fit of thermal noise for different segments of the thermomechanical noise.

Run	Q	f_0
1	187	183.2
2	174	183.2
3	148	183.3
4	219	183.1
5	186	183.3

4.3 Discussion

In this chapter, we focused on five techniques of estimating damping in a nickel nanofilm using MD simulations. The various factors involved in extracting the dynamics of the structure have been discussed in detail. The interactions of the Ni atoms were captured using the EAM potential. The nickel nanofilm was evolved in an NVT ensemble using the NH thermostat. This ensured that the thermal environment of the system resembled a realistic scenario of constant temperature. The details of the thermal equilibrium process, and the selection scheme for the choice of the thermostat time constant have been discussed.

Damping in the nanofilm was estimated at two different frequency regimes. In the subresonant regime, damping was estimated in terms of loss factor (η) and loss tangent ($\tan\phi$) by harmonically oscillating the nanofilm in the longitudinal mode. Harmonic forces were applied on the free end of the structure and the displacement and the velocity of the end layer was recorded. The loss angle method provided

a computational advantage over the loss factor approach since the stiffness and the amplitude of vibration were not required for computing the loss tangent, unlike the loss factor. As a check on our simulations, the loss factors in Table 4.1 for the Ni nanofilm were compared with the results in Ref. [62], and the results are shown in Table 4.3. The structural dimensions and several simulation parameters (including the EAM potential, integration time step, and the thermostat time constant) are the same in both studies. But the simulation times are significantly different at certain frequencies, as noted in the table. The results are in good agreement with differences ranging from 9% to 24%.

Table 4.3: Loss factors of the Ni nanofilm at 300 K. The simulation time is noted in parentheses.

Frequency	Loss factor		
	This work	Ref. [62]	Difference
10 GHz	9.06×10^{-4} (80 ns)	6.90×10^{-4} (30 ns)	23.8%
15 GHz	1.27×10^{-3} (42 ns)	1.08×10^{-3} (30 ns)	14.9%
20 GHz	1.56×10^{-3} (30 ns)	1.37×10^{-3} (30 ns)	12.1%
25 GHz	1.87×10^{-3} (11 ns)	1.67×10^{-3} (30 ns)	10.7%
30 GHz	2.11×10^{-3} (14 ns)	1.92×10^{-3} (30 ns)	9.0%

Two aspects which affected the precision of our calculations in the subresonant regime were convergence and linearity of damping. The magnitude and the convergence behavior of the loss angle and loss factor was found to depend on the magnitude of the harmonic force. For very small forces the response of the system was in the fluctuation dominated regime and the loss angle and the loss factor were very slow to converge, an increase in the magnitude of the harmonic force drove the system into

mechanical regime and faster convergence of damping was observed, further increase in the force magnitude resulted in nonlinear damping. This interplay between thermal noise and its effect on the dynamics was found to determine the precision of the damping estimates.

While controlling the linear behavior of the structure is not always possible, it is desirable to verify the linearity of extracted measurements to ensure the selection of the simulation parameters and the subsequent analysis (which usually assumes linearity) is reasonable. We have proposed a rational selection of the simulation parameters and their linearity assessment using convergence.

In the resonant regime, damping was estimated using three methods. Analysis of the free decay in the longitudinal mode revealed that the damping and the decay frequency varied depending on the amplitude of vibration, which is a signature of nonlinearity. The frequency response of amplitude from steady-state harmonic vibrations around the longitudinal resonance frequency showed that the system was driven into nonlinear regime showing characteristics of Duffing nonlinearity. Finally, a Lorentzian fit to the PSD of displacement noise gave a Q-factor of 183, which matched closely with Q-factor of 210 from free decay analysis, and Q-factor of 215 from the nonlinear Duffing analysis.

For all the methods, the damping was estimated without invoking any assumptions of macroscale (or continuum-based) concepts. In addition the methods were also insensitive to the underlying mechanisms of dissipation. The choices of the dynamic model was guided by the response observed in the simulations, and by following the dictum of selecting the simplest model that can provide the required level of detail and insight. Therefore, the proposed methodology can be applied to study any material, structure, mode, and temperature, using the appropriate potentials, boundary conditions, and thermal equilibration. For instance, the equations used for estimating the loss tangent and the loss factor were selected after observing the linear force displacement curve and steady-state time-

harmonic oscillations in the sub-resonant regime. Similarly, the use of the Duffing model was guided by the nonlinearity observed at resonance.

In the sub-resonant regime, damping can be estimated as functions of frequency and temperature using the loss tangent and loss factor. No assumptions are made about the nature, magnitude, or mechanisms of dissipation. Further, both measures can be computed using the same set of simulations with little incremental cost. It is useful to do so because the relative values of $\tan\phi$ and η can be used to assess linearity. In general, however, simulating damping in the sub-resonant regime is expensive because of the cost associated with assessing convergence and linearity.

4.4 Summary

Isothermal MD simulations have been performed to estimate damping in a nickel nanofilm using four different measures of damping. Thermomechanical noise and amplitude dependent material nonlinearities were found to influence the precision of the loss factor and loss tangent in the subresonant regime. We devised guidelines for a cost effective selection of the simulations parameters to ensure precision of the damping estimation by considering linearity and convergence of the damping measures. In the resonant regime damping was estimated using the logarithmic decrement, the Q-factor from the steady-state harmonic oscillation in the vicinity of the resonance frequency and the Q-factor from the spectrum of the thermomechanical noise. The oscillations in the nanofilm during free and forced vibration in the vicinity of the resonance frequency was of nonlinear nature. However, the spectrum of the thermal noise technique which does not necessitate the use of external stimuli showed linear Lorentzian peaks at fundamental frequency. Damping

estimated using nonlinear analysis of the free decay and the steady-state harmonic oscillations showed good agreement with damping calculated from the PSD of the thermal noise.

Chapter 5

Damping in single-crystal silicon nanoresonators

This chapter presents results from the isothermal molecular dynamics simulations of damping in a single-crystal Si nanofilm and a single-crystal Si nanowire. The SW potential and the NH thermostat were used to account for the atomic interactions and perform thermal equilibration of the structures. Damping was evaluated as a function of frequency and temperature in the subresonant regime in terms of $\tan\phi$ and η.

Section 4.1 discusses the structural details of the Si nanostructures, and the thermal equilibration steps. The section ends with the estimates of natural frequencies of both the structures obtained from the FFT of the thermal noise and rationale behind the choice of the harmonic force and simulation time to ensure the convergence and linearity of $\tan\phi$ and η in the subresonant regime. Section 4.2 presents the results of damping in the nanofilm as a function of temperature and frequency. A comparison of damping in the nanofilm and the nanowire as a function of frequency at 300 K is also reported. In Section 4.3, we present an analysis of different mechanisms of material damping using the method of elimination to identify phonon related mechanisms as the dominant source of damping in Si nanostructures. Quantitative comparisons of $\tan\phi$ with different models of phonon mediated damping are presented.

5.1 Simulation methodology

This section presents the details of the simulation parameters such as structural dimensions, interatomic potential, and thermal equilibration steps. Surface reconstruction was observed in the free surfaces of both the structures as they were heated up to the desired temperatures. We have discussed different aspects of the surface reconstruction process. The section ends with the estimates of natural frequencies calculated from the thermal noise, values of axial stiffness obtained from the tensile tests, and the choice of simulation parameters used for the estimation of $\tan\phi$ and η in the subresonant regime for both the nanoresonators.

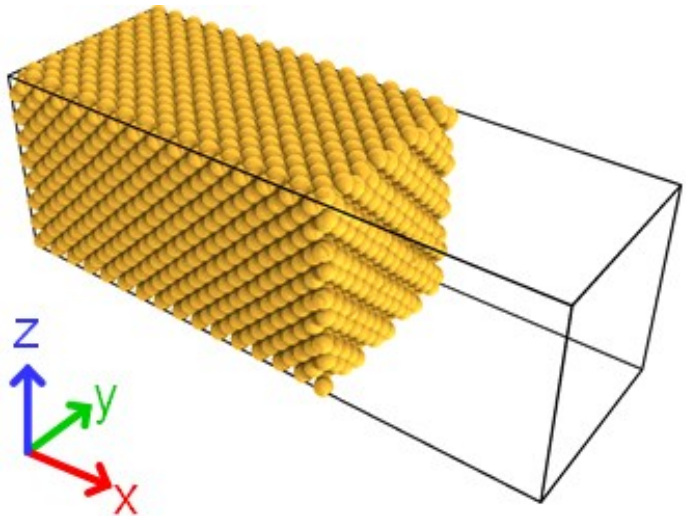

Figure 5-1: A schematic illustration of the single-crystal Si nanofilm.

5.1.1 Structural details

A nanofilm and a nanowire of single-crystal Si were constructed by placing atoms in body centered tetragonal (bct) lattice positions with a lattice parameter of 5.43 Å. A schematic of the nanofilm is shown in Figure 5-1. The structures were clamped at one end. The dimensions of the *y*-*z* cross-

sections were 4.3 nm × 4.3 nm, and the lengths (l_x) along the [1 0 0]-direction were 7.6 nm in both the structures. Periodic boundary condition was applied in the lateral (y and z) directions and free surface condition was applied in the axial direction for the nanofilm. The nanowire was built using free surface condition in all the directions.

5.1.2 Thermal equilibration

The thermal equilibration of the nanostructures were performed using the methodology discussed in Section 4.1. The starting temperature of the Si atoms was 1 K which was further raised to the desired temperatures in 4 ns using the NH thermostat. Four different thermostat time constants (0.01 ps, 0.1 ps, 1 ps and 10 ps) were selected for the thermal equilibration steps. The potential energies and the temperatures of the structures were monitored while they evolved in the NVT ensemble for each of the above-mentioned values of τ_{NH}.

Figure 5-2 shows the time trace of the potential energy in the nanofilm captured for a total duration of 84 ns for all four values of τ_{NH}. It can be observed that the structure attained an equilibrium potential energy of -5.3005 × 10^{-15} Jules using a τ_{NH} -value of 0.01 ps, the lowest compared to the rest of the values of τ_{NH}. Time trace of temperature in the nanofilm using τ_{NH} of 0.01 ps is shown in Figure 5-3. No large fluctuations were observed in the potential energy and the temperature profiles of the nanofilm for the entire duration. The structure was thermally equilibrated after 84 ns. Similar steps were followed for the thermal equilibration of the nanowire using a τ_{NH} of 0.01 ps.

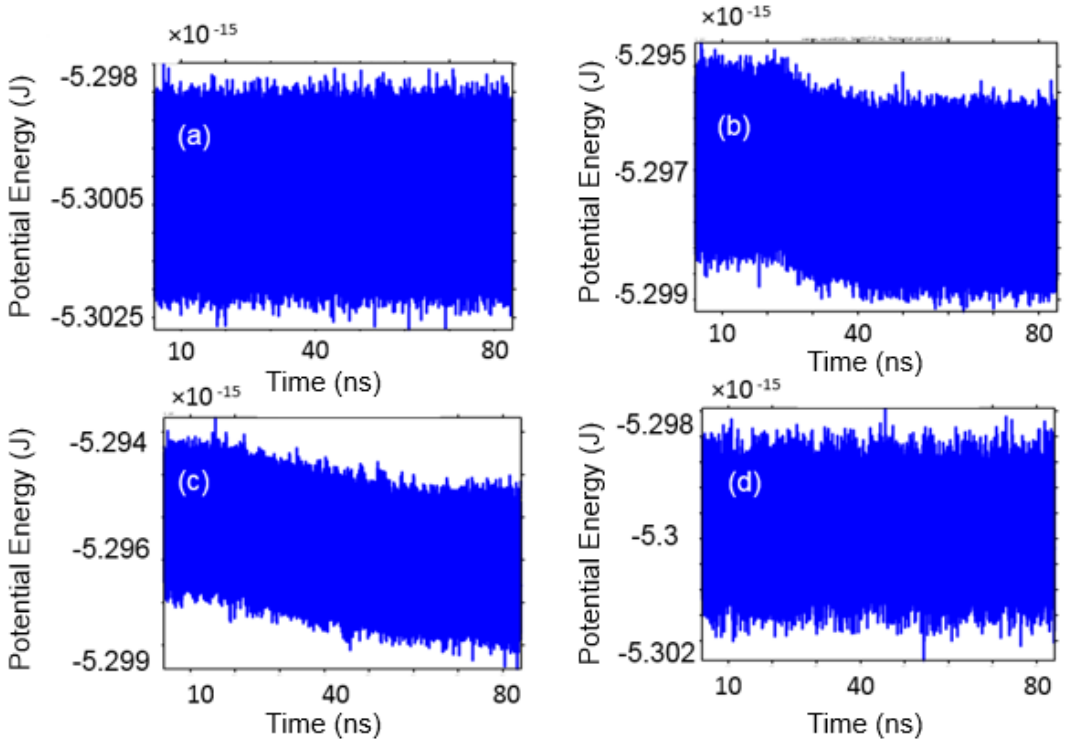

Figure 5-2: Time traces of potential energy in the nanofilm at 300 K simulated using a Nosé-Hoover thermostat for τ_{NH} : (a) 0.01 ps, (b) 0.1 ps, (c) 1 ps, and (d) 10 ps captured for 84 ns.

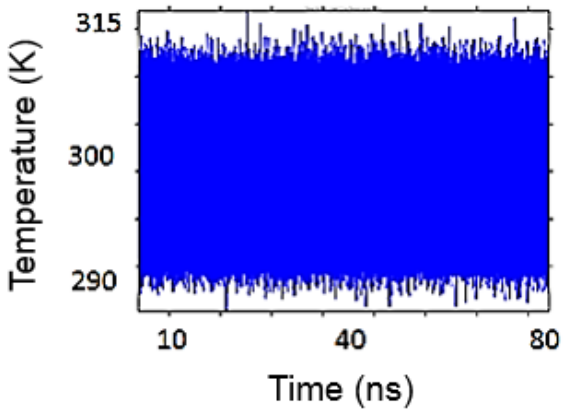

Figure 5-3: Temperature profile of the nanofilm during the thermal equilibration at 300 K using τ_{NH} = 0.01 ps. No major fluctuations in the temperature profile could be observed for the entire duration.

5.1.3 Surface reconstruction

Surface reconstruction was observed in the free surfaces of the nanofilm and the nanowire. When free surfaces are imposed on nanostructures, at least one bond per atom is cut upon cleavage. These bonds are called the dangling bonds. These unsaturated dangling bonds make the surface unstable and are responsible for an increase in the surface energy. A reduction in the number of dangling bonds minimizes the surface energy and is the driving force behind the reconstruction. The reconstruction of surfaces involve changes in the surface unit cells compared to the bulk, leading to changes in the periodicity and symmetry of the atoms at the surface.

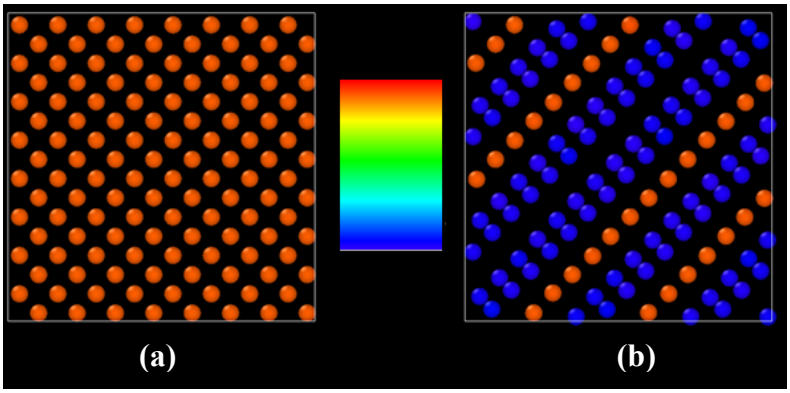

Figure 5-4: Potential energy of the individual atoms in the (1 0 0) surface in the nanofilm: (a) initial configuration, and (b) after surface reconstruction. Color chart represents different levels of potential energy, red being the highest potential energy and blue is the lowest potential energy.

We observed that as the temperature of the structures were increased, atoms in the free surfaces in both the structures broke away from the initial diamond cubic network and created dangling bonds, forming 2×1 surface dimers. This observation is consistent with previous work on surface reconstruction in SW Si [142]. Figure 5-4 (a) shows the (100) surface of the nanofilm at 1 K, and Figure 5-4 (b) is the reconstructed surface. Once the surface reconstruction was over, the configuration of the surface atoms were different from the bulk atoms.

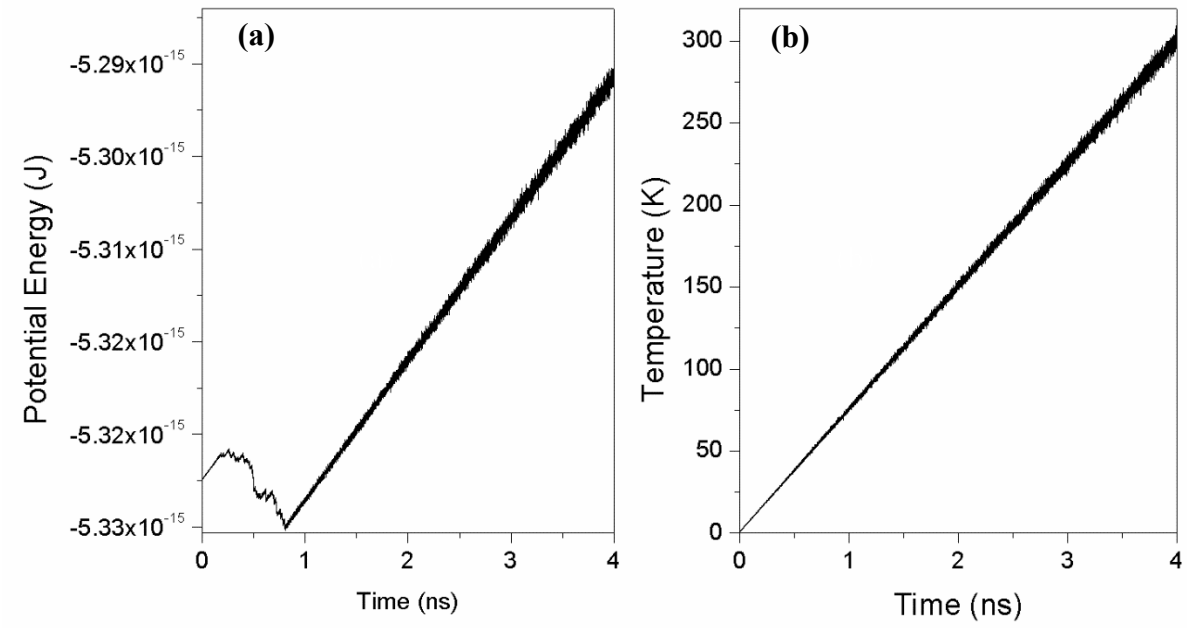

Figure 5-5: Time trace of (a) potential energy, and (b) temperature in the nanofilm during heating from 1 K to 300 K.

Figure 5-5 (a) and (b) represent the time traces of the potential energy and the temperature in the nanofilm as it was gradually heated up to 300 K. It can be observed from Figure 5-5 (a) that till about 0.2 ns the potential energy in the nanofilm increased monotonically. After 0.2 ns and till 0.8 ns the potential energy dropped and reached a minimum of -5.332×10^{-15} Joules. During this time the reconstruction was completed. After 0.8 ns the potential energy again increased monotonically. This behavior is absent in the temperature profile (Figure 5-5 (b)) and for the entire duration the temperature in the nanofilm increased monotonically. The potential energy of individual atoms in the free (1 0 0) surface of nanofilm at 0 K and after 0.8 ns of heating is shown in Figure 5-4 (a) and (b) using color gradient. It can be seen that during heating the structure some of the atoms in the free surface move and form 2×1 dimers and in the process reduce their potential energy.

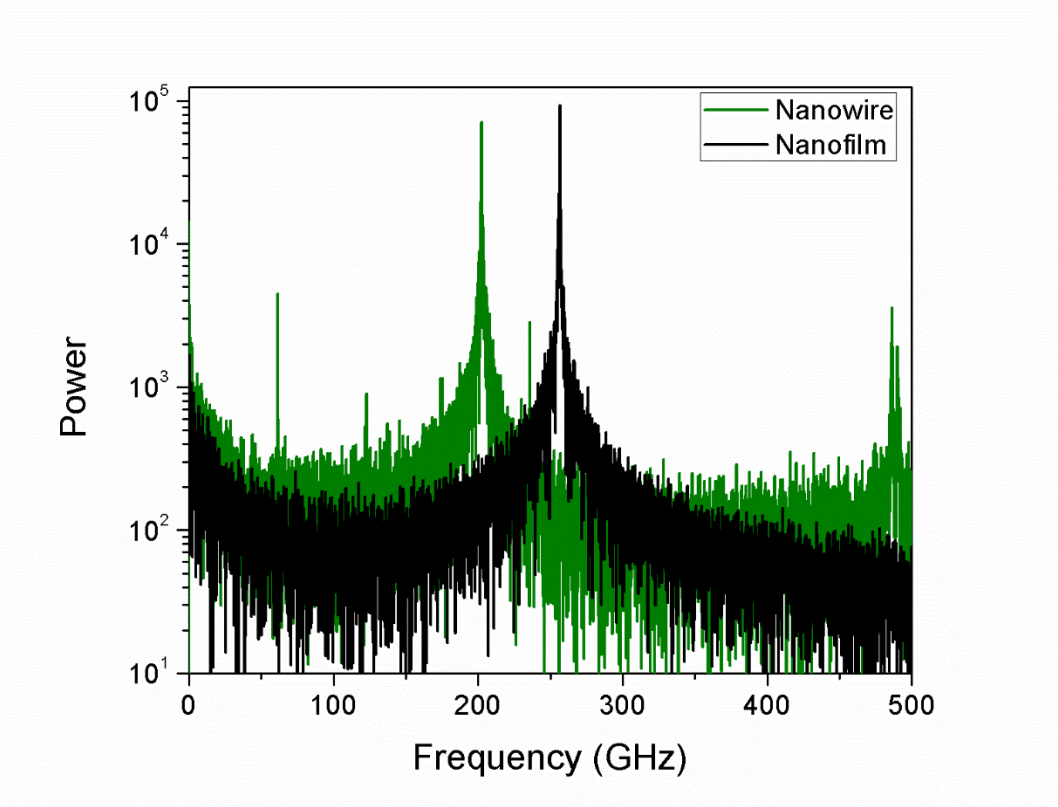

Figure 5-6: Fast Fourier transform (FFT) of the thermomechanical noise for the nanowire and the nanofilm. The peaks at 256.5 GHz for the nanofilm and 202 GHz for the nanowire correspond to the fundamental longitudinal natural frequencies.

5.1.4 Natural frequency (f_0) and axial stiffness (K_x)

The FFT of the thermal noise of the atoms at $x = l_x$ was analyzed to obtain the estimates of natural frequencies of the nanofilm and the nanowire. Figure 5-6 shows the FFT spectrum for both the structures showing characteristic peaks at their natural frequencies. The fundamental longitudinal frequency of the nanofilm and nanowire were 256.5 GHz and 202 GHz, respectively. Tensile tests were performed by applying static forces on the atoms in the end layer at $x = l_x$ to estimate the values of the longitudinal stiffness. As shown in Figure 5-7 (a), the force-displacement curves exhibited linear response till a force magnitude of 73 nN for the nanofilm and 61 nN for the

nanowire. Corresponding stress-strain plots are shown in Figure 5-7 (b). The magnitude of the axial stiffness for the nanofilm and the nanowire at 300 K were estimated to be 352 N/m and 210 N/m. Similar tests were performed to obtain estimates of K_x at other temperatures. These results indicate that for identical dimensions and material properties, the resonance frequency and the axial stiffness of the nanowire is smaller than the nanofilm. Also, the Young's modulus for the nanowire dropped to 87 GPa compared to 143 GPa in the nanofilm. This behavior is in agreement with experimental findings [143].

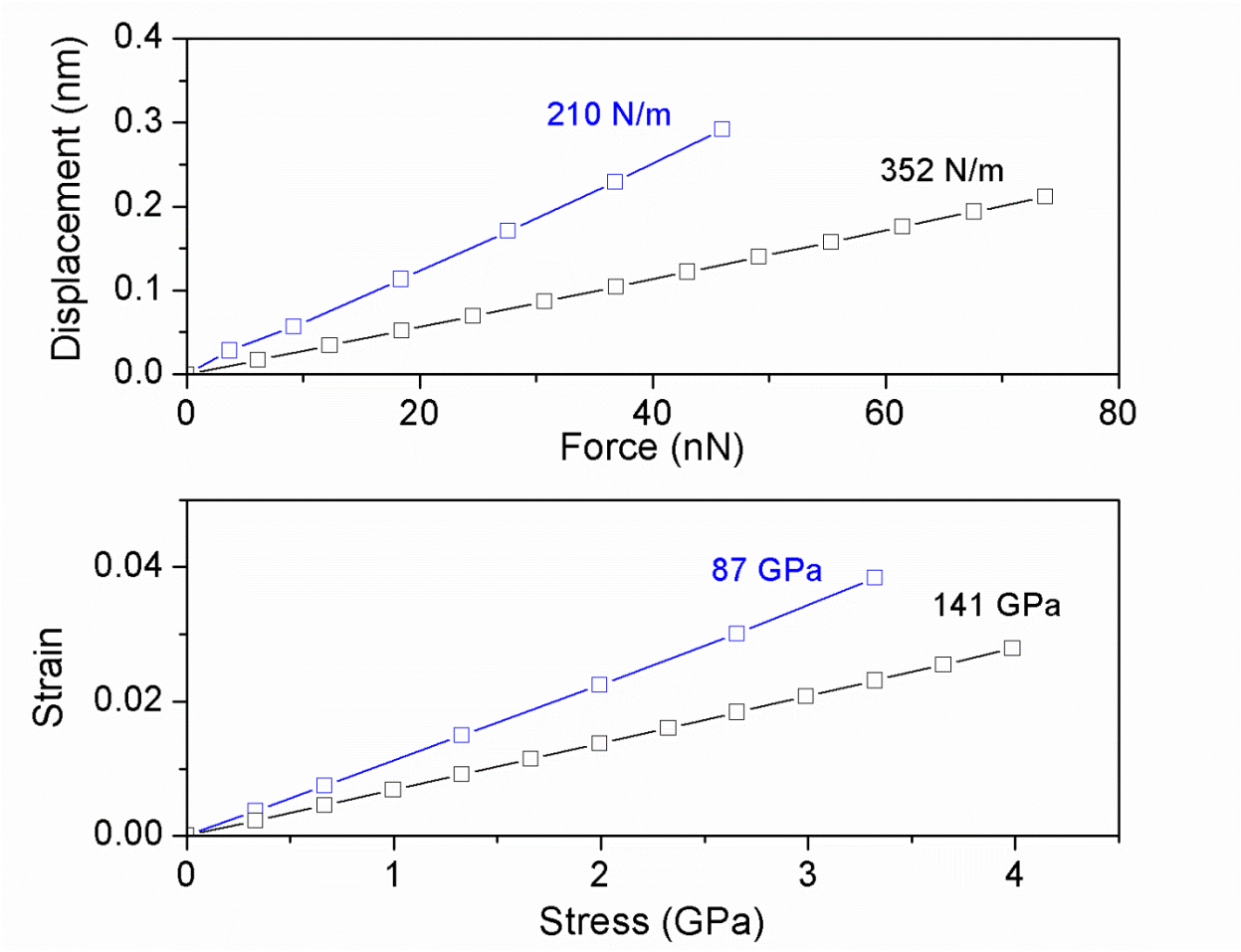

Figure 5-7: (a) Force-displacement, and (b) stress-strain curves for the nanofilm (black) and the nanowire (blue) used for estimating the axial stiffness and Young's modulus utilizing a linear least-squares analysis.

5.1.5 Damping in the subresonant regime

This section discusses the rationale behind the selection of different simulation parameters such as frequency of oscillation (f), magnitude of harmonic force (F_0), and convergence time (t_c) used for obtaining precise estimates of $\tan\phi$ and η.

Figure 5-8 (a) and (b) show the response of the nanofilm and the nanowire under the application of harmonic forces at 300 K, respectively. It is seen that for forces above 2 nN, the response of the structures surpass the thermomechanical noise floor. The stress-strain plots for the nanofilm and the nanowire (see Figure 5-7 (b)) reveal that for stresses up to 4 GPa (force 73 nN) for the nanofilm and 3.3 GPa (force 67 nN) for the nanowire the structures behave linearly.

Figure 5-9 represents the convergence curves of $\tan\phi$ and η in the nanofilm for longitudinal oscillations at 10 GHz calculated after each nanosecond for a total duration of 150 ns. The operating temperature was maintained at 300 K. The different curves illustrate the effect of increasing the magnitude of the harmonic force (starting from 12 nN till 86 nN) on damping as a function of time. The following observations are made from the figure. For small value of F_0 (12 nN), the harmonic response is comparable to the thermal noise floor and damping fluctuates between 3×10^{-4} and 4×10^{-4}. As the force amplitude was increased, simulations converged in the linear regime with $\tan\phi$ and η converging to 2.4×10^{-4} after 122 ns. Furthermore, $\tan\phi$ and η remained unchanged and converged linearly when the force was increased to 61 nN and 86 nN. We used 49 nN as the harmonic force for further damping simulations in the nanofilm.

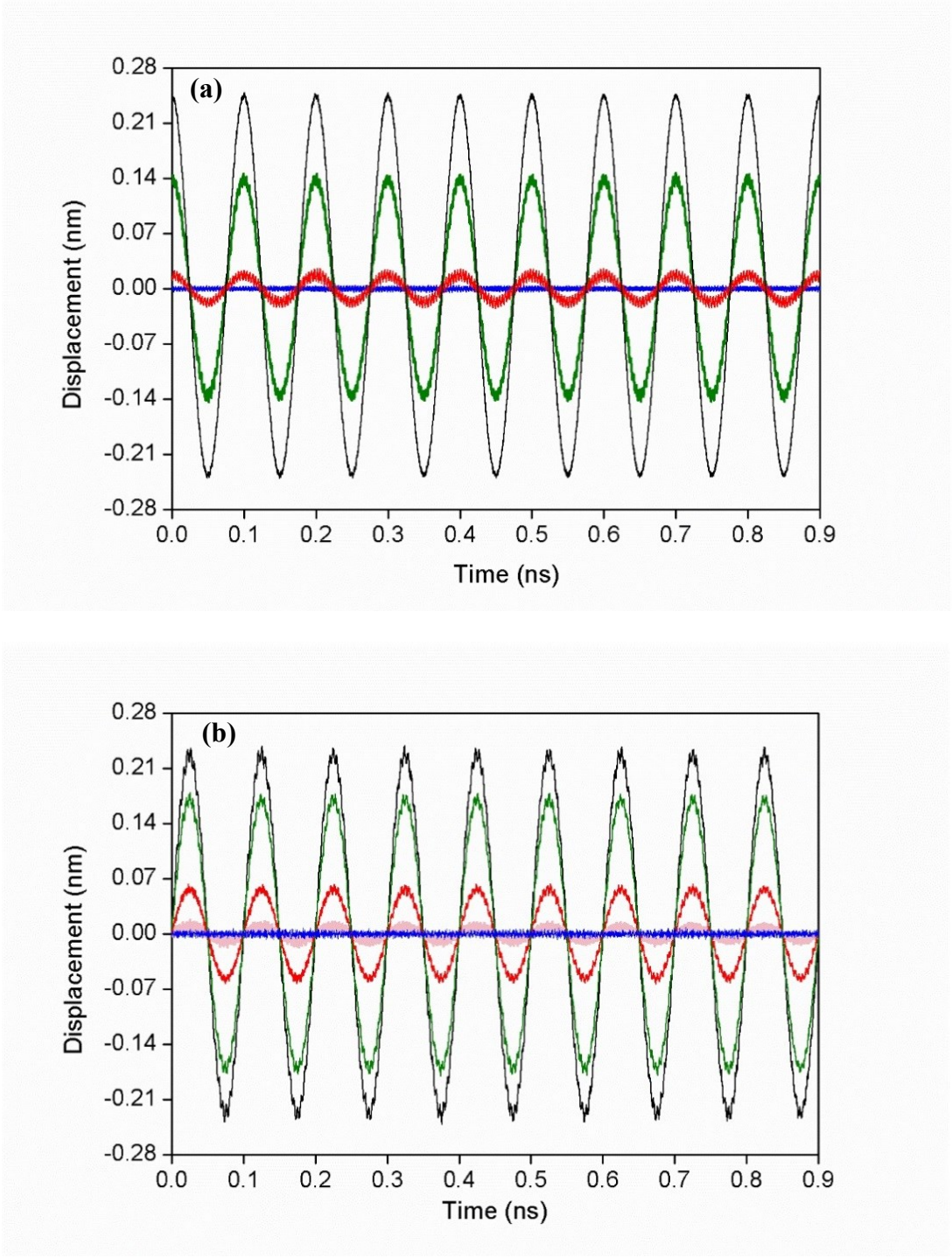

Figure 5-8: Axial displacement of the free end of the silicon (a) nanofilm and (b) nanowire while oscillating at 10 GHz. The blue curve shows the thermomechanical noise in the absence of any external driving force. In (a) the black, green, and red correspond to force amplitudes of 86 nN, 49 nN, 6 nN respectively. In (b) the black, green, red and pink correspond to force amplitudes of 49 nN, 37 nN, 12 nN and 2nN respectively.

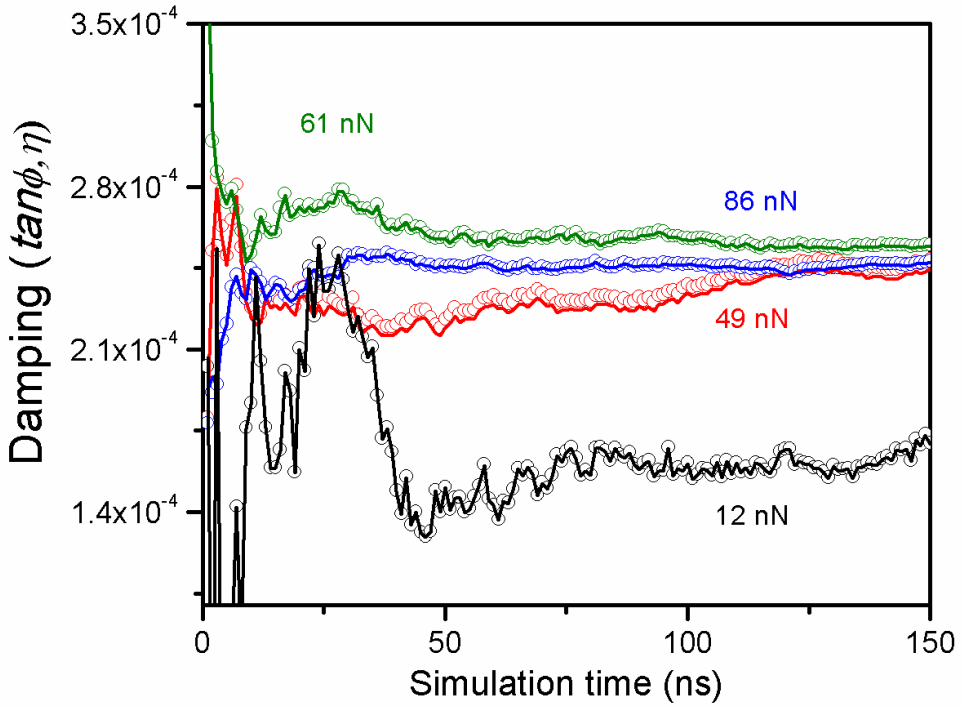

Figure 5-9: Convergence behavior of the loss tangent ($\tan\phi$) and the loss factor (η) in the nanofilm for longitudinal-mode oscillations at 10 GHz. The symbols represent the loss factor (η) and the lines represent the loss tangent ($\tan\phi$). Both measures were computed after every nanosecond. In all cases, $\tan\phi$ and η differed by less than 5%.

Figure 5-10 represents the convergence curves of $\tan\phi$ and η in the nanowire for longitudinal oscillations at 10 GHz calculated after each nanosecond for a total duration of 150 ns. For very small F_0 (2.5 nN) damping fluctuates wildly and does not converge. For the magnitude of the force 25 nN and 29 nN, the fluctuations in damping were mild but still did not converge till 150 ns. As the force amplitude was further increased, the simulations converged in the linear regime, with average $\tan\phi$ and η in the range 3.73×10^{-4} to 5.73×10^{-4}, giving a standard deviation of 7.08×10^{-5} for $\tan\phi$. We chose 37 nN as the harmonic force for damping simulations in the nanowire in the subresonant regime.

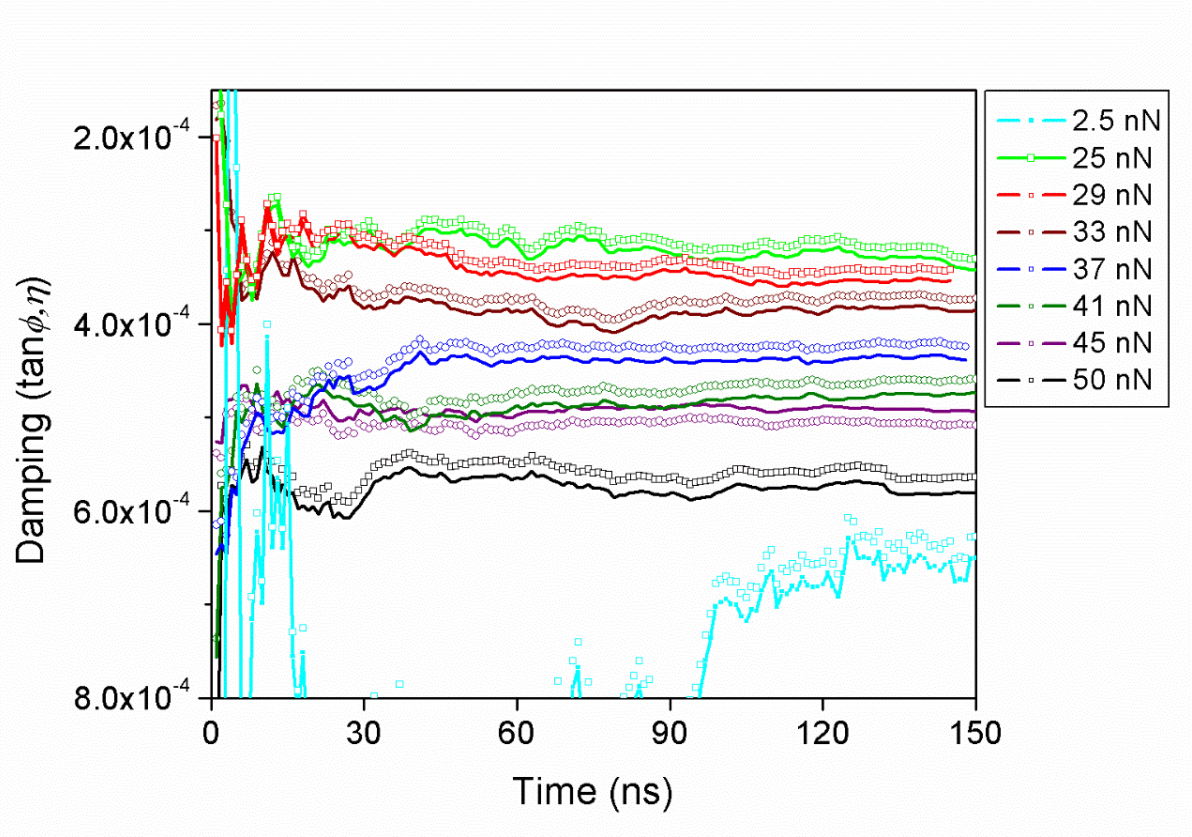

Figure 5-10: Convergence behavior of the loss tangent ($\tan\phi$) and the loss factor (η) for longitudinal-mode oscillations at 10 GHz of the nanowire. The symbols represent the loss factor (η) and the lines represent the loss tangent ($\tan\phi$). Both measures were computed after every nanosecond. In all cases, $\tan\phi$ and η differs by less than 5%.

5.2 Results

In this section we report the estimates of damping in the nanofilm and the nanowire for longitudinal oscillations as a function of frequency and temperature. Estimates of damping were obtained as a function of frequency at 50 K, 300 K and 500 K for the nanofilm, and at 300 K for the nanowire. Frequency response curves of damping showed characteristic peaks. The peaks in damping for the nanofilm shifted as the operating temperature was varied.

5.2.1 Frequency response of damping in the nanofilm as a function of temperature

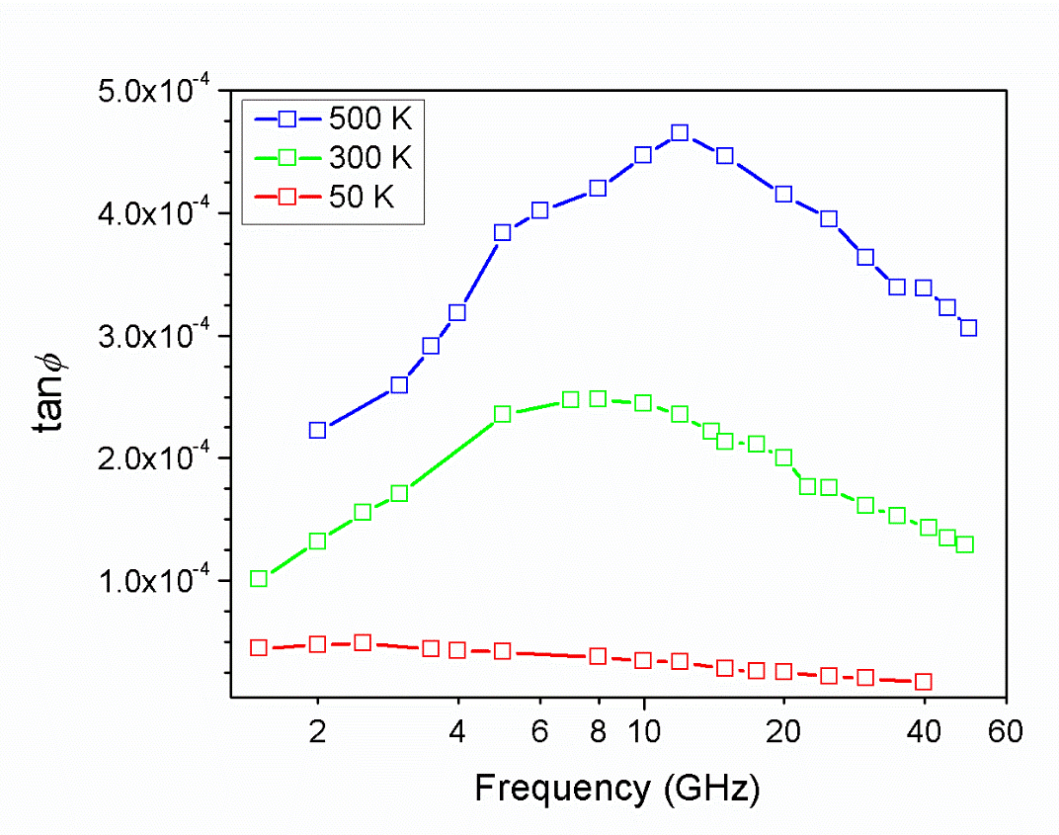

Figure 5-11: Comparison of frequency response of $\tan\phi$ in the nanofilm at 50 K, 300 K and 500 K. The magnitude of the harmonic force was 49 nN for all the simulations. Symbols of different colors represent damping estimates at 50 K (red), 300 K (green), and 500 K (blue). For the entire frequency range the maximum difference between the converged values of $\tan\phi$ and η in the nanofilm was less than 2.28% at 50 K, 1.86% at 300 K, and 3.06% at 500 K.

Figure 5-11, shows the comparison of damping in the nanofilm as a function of frequency at 50 K, 300 K and 500 K. The following observations can be made from the figure: (a) damping in the nanofilm at 300 K and 500 K is not monotonic, rather damping initially increases as the frequency is increased, reaches a peak, as the frequency is further increased damping drops monotonically, (b) a reduction in the temperature of the nanofilm from 500 K to 300 K shifted the frequency

corresponding to the peak in damping, (c) the peak in damping is not clearly visible for the curve corresponding to 50 K, for which damping initially increases till 3 K after which decreases monotonically till 40 GHz, and (d) overall, damping in the film increased with an increase in temperature. For the entire frequency range the maximum difference between the converged values of $\tan\phi$ and η in the nanofilm was less than 2.28% at 50 K, 1.86% at 300 K, and 3.06% at 500 K. Lists of $\tan\phi$ and η over the entire frequency range is presented in Table 5.1 (at 50 K), Table 5.2 (at 300 K) and Table 5.3 (at 500 K).

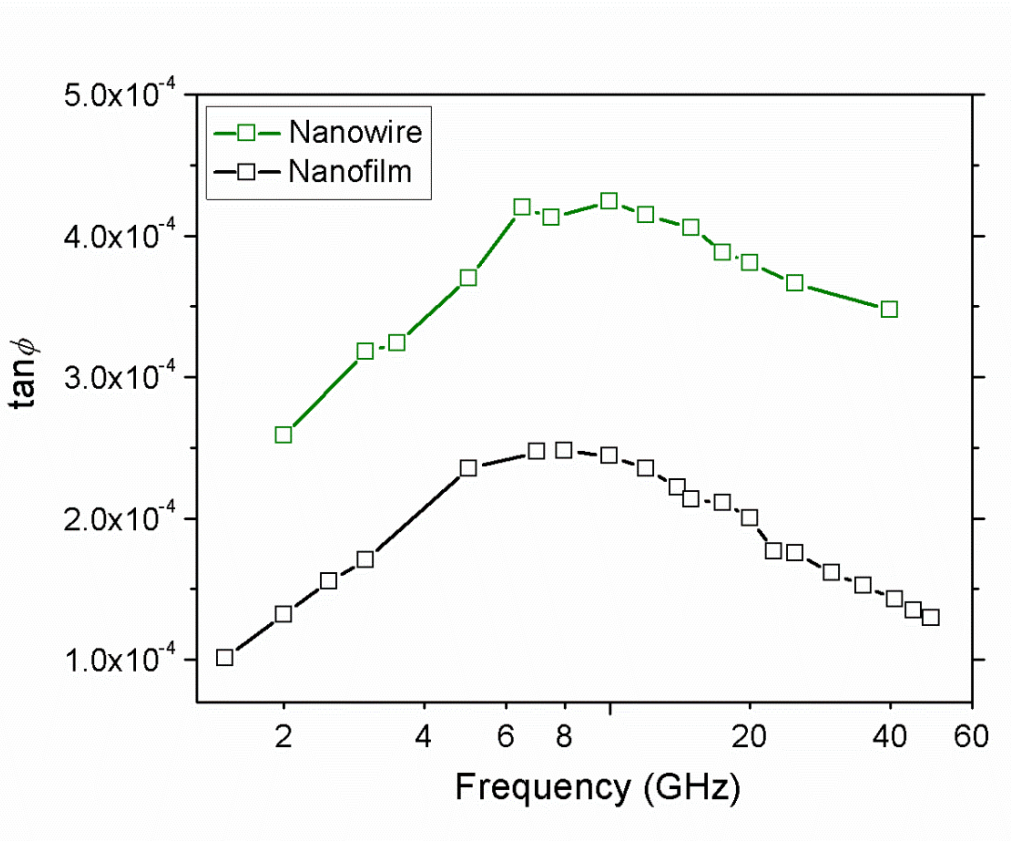

Figure 5-12: Comparison of the frequency response of damping in the nanofilm and the nanowire for longitudinal oscillations at 300K. Symbols represent estimates of $\tan\phi$. The magnitude of the applied force on the nanofilm and the nanowire was 49 nN and 37 nN respectively.

5.2.2 Comparison of damping in the nanofilm and the nanowire at 300 K

Figure 5-12 represents the comparison of damping in the nanofilm and the nanowire for longitudinal oscillations at 300 K. It can be seen that the damping-curves for both the structures follow similar trends as the frequency of oscillation is varied. Initially damping increases in both the structures, reaches a maximum in the range 6 GHz and 10 GHz. For frequencies larger than 10 GHz damping in both the structures decreases. Another interesting feature is that for the entire frequency range the nanowire dissipates more energy than the nanofilm. A list of $\tan\phi$ and η in the nanowire over the entire frequency range is presented in Table 5.4.

Table 5.1: Damping in the Si nanofilm at 50 K for the longitudinal-mode oscillation.

Frequency (GHz)	Total simulation time, t_f (ns)	Convergence time, t_c (ns)	$\tan\phi$	η	$\frac{\tan\phi-\eta}{\tan\phi}\times 100$
1.5	352	308	4.45×10^{-5}	4.55×10^{-5}	2.26
2	253	214	4.76×10^{-5}	4.87×10^{-5}	2.22
2.5	253	129	4.87×10^{-5}	4.98×10^{-5}	2.23
3	253	169	4.98×10^{-5}	5.09×10^{-5}	2.23
3.5	253	124	4.38×10^{-5}	4.47×10^{-5}	2.23
4	267	125	4.25×10^{-5}	4.35×10^{-5}	2.21
5	254	124	4.20×10^{-5}	4.29×10^{-5}	2.21
8	152	112	3.77×10^{-5}	3.85×10^{-5}	2.15
10	152	73	3.45×10^{-5}	3.52×10^{-5}	2.11
12	152	65	3.36×10^{-5}	3.43×10^{-5}	2.05
15	152	91	2.79×10^{-5}	2.85×10^{-5}	1.96
17.5	152	89	2.57×10^{-5}	2.62×10^{-5}	1.86
20	152	77	2.50×10^{-5}	2.54×10^{-5}	1.75
25	152	62	2.15×10^{-5}	2.18×10^{-5}	1.44
30	152	77	2.05×10^{-5}	2.08×10^{-5}	1.10
40	152	89	1.73×10^{-5}	1.73×10^{-5}	0.23

Table 5.2: Damping in the Si nanofilm at 300 K for longitudinal-mode oscillation.

Frequency (GHz)	Total simulation time, t_f (ns)	Convergence time, t_c (ns)	$\tan\phi$	η	$\frac{\tan\phi-\eta}{\tan\phi}\times 100$
1.5	548	359	1.01×10^{-4}	1.03×10^{-4}	1.85
2	552	381	1.32×10^{-4}	1.34×10^{-4}	1.86
2.5	351	218	1.55×10^{-4}	1.56×10^{-4}	0.39
3	550	288	1.71×10^{-4}	1.73×10^{-4}	1.58
5	352	188	2.35×10^{-4}	2.40×10^{-4}	1.84
7	252	114	2.47×10^{-4}	2.51×10^{-4}	1.75
8	246	147	2.48×10^{-4}	2.52×10^{-4}	1.73
10	251	122	2.44×10^{-4}	2.48×10^{-4}	1.72
12	152	69	2.35×10^{-4}	2.39×10^{-4}	1.65
14	152	43	2.21×10^{-4}	2.25×10^{-4}	1.61
15	152	54	2.13×10^{-4}	2.16×10^{-4}	1.57
17.5	152	70	2.11×10^{-4}	2.11×10^{-4}	0.12
20	151	76	2.00×10^{-4}	2.03×10^{-4}	1.42
22.5	149	36	1.76×10^{-4}	1.78×10^{-4}	1.20
25	152	47	1.76×10^{-4}	1.77×10^{-4}	1.04
30	150	51	1.61×10^{-4}	1.62×10^{-4}	0.15
35	152	44	1.53×10^{-4}	1.53×10^{-4}	0.31
41	152	34	1.43×10^{-4}	1.42×10^{-4}	0.29
45	152	37	1.35×10^{-4}	1.34×10^{-4}	0.74
49	152	38	1.29×10^{-4}	1.28×10^{-4}	1.23

Table 5.3: Damping in the Si nanofilm at 500 K for longitudinal-mode oscillation.

Frequency (GHz)	Total simulation time, t_f (ns)	Convergence time, t_c (ns)	$\tan\phi$	η	$\frac{\tan\phi-\eta}{\tan\phi}\times 100$
2	253	192	2.22×10^{-4}	2.27×10^{-4}	2.43
3	252	162	2.59×10^{-4}	2.67×10^{-4}	3.06
3.5	252	206	2.91×10^{-4}	3.00×10^{-4}	3.04
4	152	94	3.18×10^{-4}	3.28×10^{-4}	3.05
5	152	57	3.84×10^{-4}	3.95×10^{-4}	3.05
6	252	82	4.01×10^{-4}	4.13×10^{-4}	3.04
8	252	77	4.20×10^{-4}	4.32×10^{-4}	3.01
10	252	74	4.47×10^{-4}	4.60×10^{-4}	2.97
12	152	39	4.65×10^{-4}	4.79×10^{-4}	2.92
15	152	44	4.46×10^{-4}	4.59×10^{-4}	2.82
20	136	23	4.14×10^{-4}	4.25×10^{-4}	2.60
25	152	42	3.95×10^{-4}	4.04×10^{-4}	2.31
30	152	54	3.63×10^{-4}	3.70×10^{-4}	1.96
35	152	39	3.39×10^{-4}	3.44×10^{-4}	1.53
40	152	16	3.38×10^{-4}	3.42×10^{-4}	1.04
45	150	15	3.22×10^{-4}	3.24×10^{-4}	0.48
50	152	22	3.06×10^{-4}	3.05×10^{-4}	0.14

Table 5.4: Damping in the Si nanowire at 300 K for longitudinal-mode oscillations.

Frequency (GHz)	Total simulation time, t_f (ns)	Convergence time, t_c (ns)	$\tan\phi$	η	$\frac{\tan\phi-\eta}{\tan\phi}\times 100$
2	149	132	2.59×10^{-4}	2.67×10^{-4}	3.36
3	148	70	3.18×10^{-4}	3.29×10^{-4}	3.39
3.5	150	118	3.24×10^{-4}	3.35×10^{-4}	3.37
5	147	80	3.70×10^{-4}	3.82×10^{-4}	3.36
6.5	150	68	4.20×10^{-4}	4.34×10^{-4}	3.35
7.5	150	53	4.13×10^{-4}	4.26×10^{-4}	3.29
10	148	38	4.24×10^{-4}	4.38×10^{-4}	3.24
12	198	155	4.15×10^{-4}	4.15×10^{-4}	0.05
15	150	59	4.06×10^{-4}	4.18×10^{-4}	2.96
17.5	150	57	3.88×10^{-4}	3.99×10^{-4}	2.81
20	151	41	3.81×10^{-4}	3.91×10^{-4}	2.56
25	151	22	3.66×10^{-4}	3.74×10^{-4}	2.13
40	147	51	3.48×10^{-4}	3.48×10^{-4}	0.13

5.3 Comparison between simulated damping and mechanisms of material damping

In order to understand these findings we go back to Section 2.1 where we have described common sources of material damping in single-crystal materials. We can examine these mechanisms one-by-one to see if their predictions are consistent with our simulations. Among the various mechanisms of material damping the possible dissipation sources in the nanofilm and the nanowire are thermoelastic damping (TED), surface damping, and phonon damping.

Table 5.5: Properties for bulk Si obtained using the SW potential.

Property	Symbol	Unit	300 K	500 K
Density	ρ	(Kg/m^3)	2315 [144]	2310 [144]
Specific heat	C_V	($J/m^3/K$)	1.55×10^6 [145]	1.84×10^6 [145]
Young's modulus	E	(GPa)	141.4 (current work)	140.1 (current work)
Thermal conductivity	k	(W/m K)	350 [146], and 255 [147]	284 [10], and 75
Speed of sound	V_s	(m/s)	7815 (calculated using Eq. (2.5)	7776 (calculated using Eq. (2.5)
Coefficient of thermal expansion	α	(K^{-1})	2.67×10^{-6} [144], 3.9×10^{-6} [148]	3.43×10^{-6} [144]
Grüneisen parameter	γ	-	0.2, 0.5, 1.2	0.2, 0.5, 1.2

Figure 5-13, shows prediction of thermoelastic damping (TED) as a function of frequency for single-crystal Si at 300 K calculated using Eq. (2.1), also super imposed in the same plot are the estimates of $\tan\phi$ for the nanofilm and the nanowire at 300 K. The material properties used for the calculations are presented in Table 5.5. The calculations of TED were performed using two different values of thermal conductivity, $k = 255$ W/m K, and 355 W/m K. It can be observed that in the frequency range of 1 GHz to 50 GHz, the estimates of $\tan\phi$ for both the nanofilm and the nanowire are significantly larger than the predictions of TED obtained using Eq. (2.1). For example, at 1 GHz, TED in single-crystal Si is equal to 1×10^{-6} whereas the magnitude of $\tan\phi$ in

both the structures were to the tune of 1×10^{-4}. It is important to note that the magnitude of thermoelastic damping gradually increased with frequency. These comparisons suggest that although TED had contributions in the estimated values of $\tan\phi$, but it was not the dominant source of damping in the Si nanoresonators.

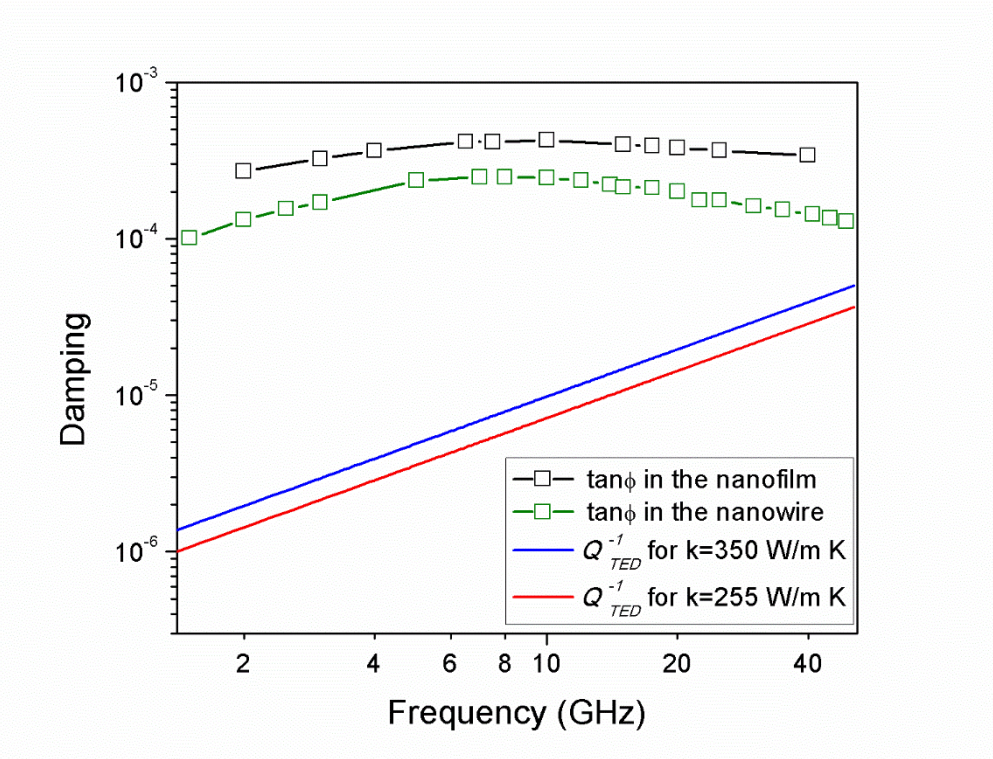

Figure 5-13: Comparison of $\tan\phi$ in the nanofilm and the nanowire at 300 K and TED calculated using Eq. (2.1). The material properties used for calculating TED are presented in Table 5.5.

Surface reconstruction in the free surfaces of both the structures took place during the thermal equilibration process (see Figure 5-4). Furthermore, due to the presence of extra free surfaces, the ratio of surface to volume ratio is higher in the nanowire (0.15) compared to the nanofilm (0.0175). As a consequence of this increased surface to volume ratio, damping in the nanowire increased by 60% to 100% than the nanofilm at 300 K over the entire frequency range investigated. This implies that damping from surface related mechanisms were significant in both the structures.

Unfortunately, a quantitative comparison of the simulated estimates of $\tan\phi$ and surface damping is not possible because of unavailability of closed-form expressions for calculating the later.

In order to find out the contribution of phonon-phonon damping, we compare the frequency response of damping in the nanofilm at 300 K and 500 K with the phonon damping models described in Section 2.1.2. Depending on the period of mean phonon relaxation time compared to the period of the forced oscillation, phonon damping manifests as either Landau-Rumer (L-R) damping or Akheiser damping.

- *Comparison of damping estimate*s *with Laundau-Rumer damping (Eq. (2.7)):* Figure 5-14 (a) and (b) show the comparison between the estimates of $\tan\phi$ in the nanoresonators and L-R damping for bulk SW Si calculated using Eq. (2.7) at 300 K and 500 K, respectively. The properties for the SW Si used for the calculations are presented in Table 5.5. The magnitudes of L-R damping were calculated for γ equal to 1.2, 0.5 and 0.2 to account for the uncertainties associated with this parameter in calculated L-R damping. This assumption for the values of γ is reasonable since the average experimental value of γ is 0.5 at 300 K [9].

A quantitative comparison reveals that the values of $\tan\phi$ are within the limits of the calculated L-R damping, but the frequency dependencies do not match. For example, the magnitudes of $\tan\phi$ varies with frequency showing characteristic peaks at both 300 K and 500 K in the nanofilm, and at 300 K in the nanowire but such peaks are not present in the frequency dependence of L-R damping. Instead, the L-R damping values are frequency independent.

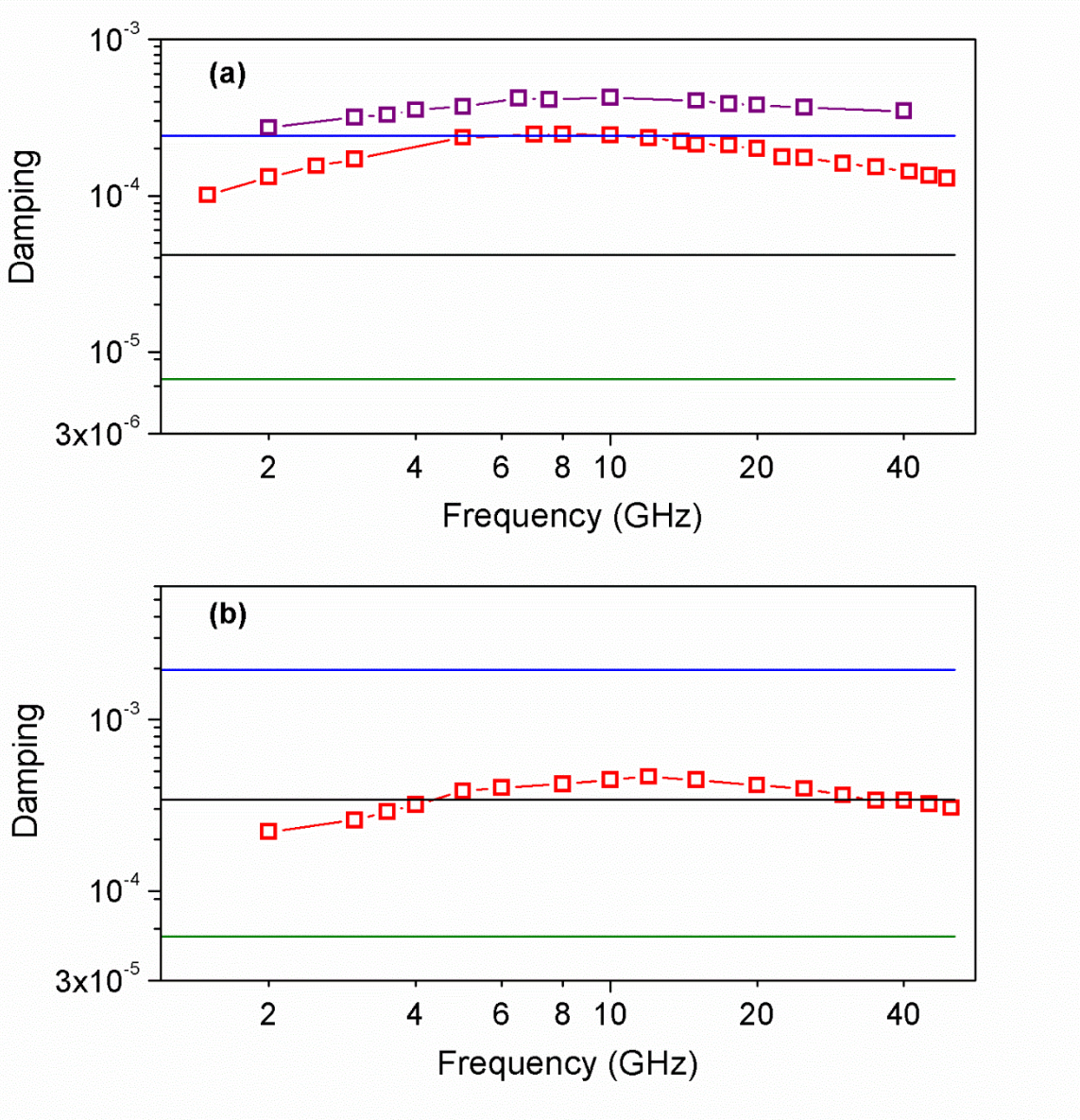

Figure 5-14: (a) Comparison between simulated $\tan\phi$ in the nanostructures and Laundau-Rumer damping in bulk SW silicon calculated using Eq. (2.1) at (a) 300 K, and (b) 500 K. The red and the violet squares represent the estimates of $\tan\phi$ in the nanofilm and the nanowire respectively. The material properties used for the calculation of L-R damping are given in Table 5.5.The blue, black and green colored lines represent damping values for γ equal to 1.2, 0.5 and 0.2.

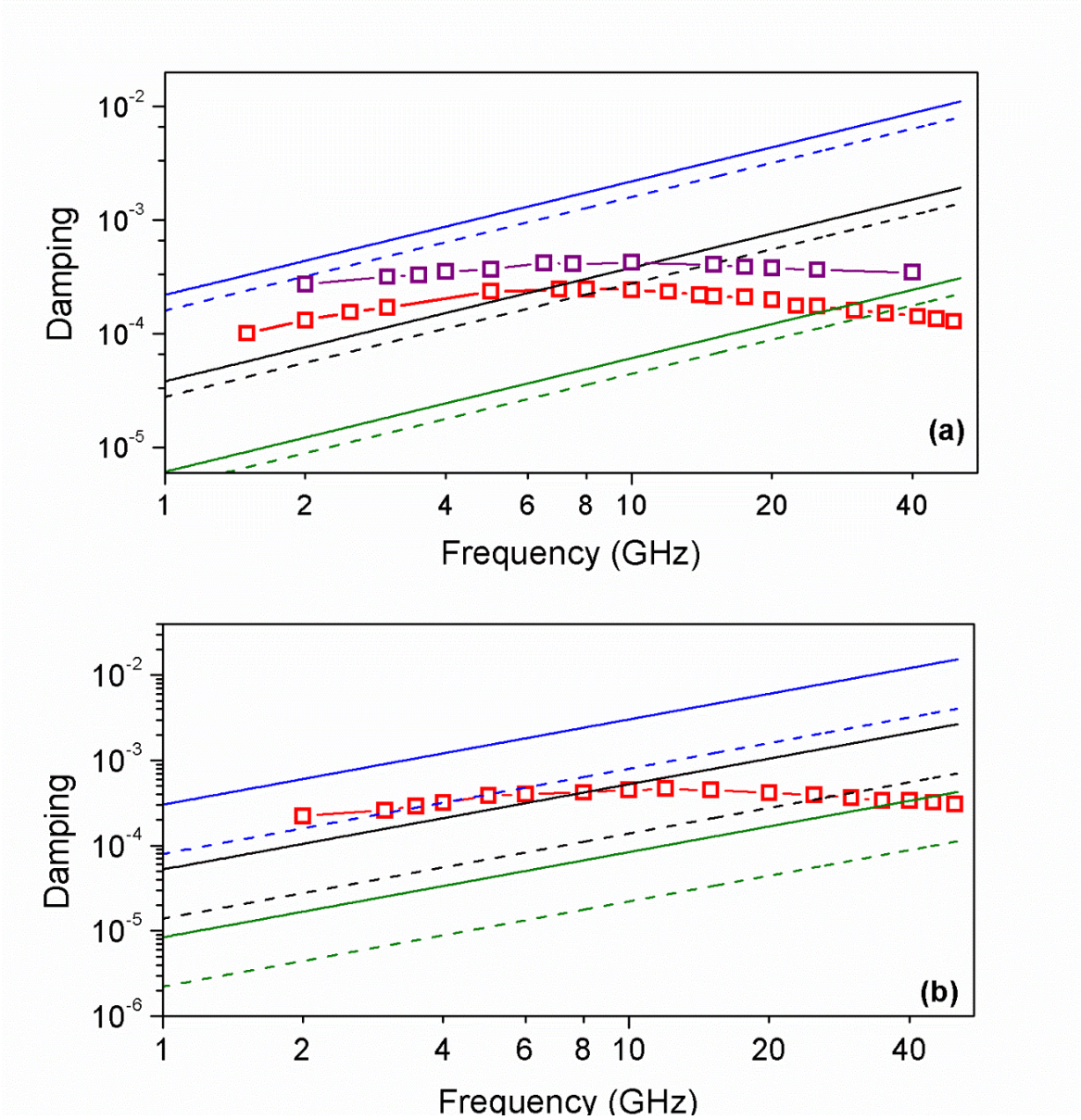

Figure 5-15: Comparison between simulated $\tan\phi$ with Akheiser damping for bulk SW silicon calculated using Eq. (2.5) at (a) 300 K, and (b) 500 K, respectively. The red and the violet squares represent the estimates of $\tan\phi$ in the nanofilm and the nanowire, respectively. The material properties used for the calculation of Akheiser damping are given in Table 5.5. The solid lines and the dashed lines represent the magnitude of Akheiser damping for the ranges of thermal conductivity for SW Silicon (355 W/m K and 255 W/m K at 300 K and 284 W/m K and 75 W/m K at 500 K). The blue, black and green colored lines represent Akheiser damping calculated using γ values of 1.2, 0.5 and 0.2, 0.5.

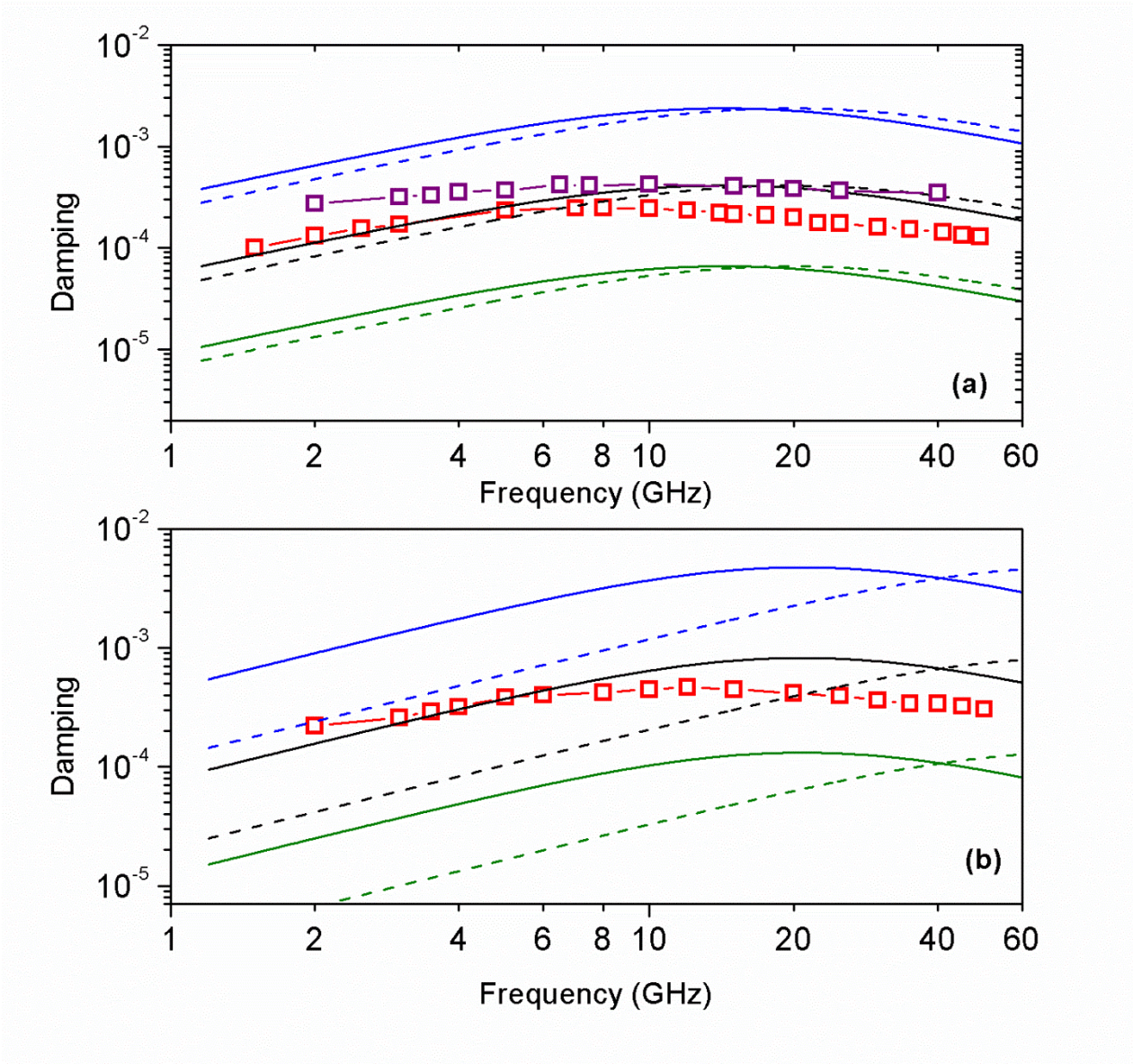

Figure 5-16: Comparison between simulated $\tan\phi$ with Akheiser damping in bulk SW silicon calculated using Eq. (2.6) at (a) 300 K, and (b) 500 K. The red and the violet squares represent the estimates of $\tan\phi$ in the nanofilm and the nanowire respectively. The material properties used for the calculation of Akheiser damping are given in Table 5.5. The solid lines and the dashed lines represent the magnitude of Akheiser damping for the ranges of thermal conductivity for SW Silicon (355 W/m K and 255 W/m K at 300 K and 284 W/m K and 75 W/m K at 500 K). The blue, black and green colored lines represent Akheiser damping calculated using γ values of 1.2, 0.5 and 0.2, 0.5.

- *Comparison of simulated damping with Eq. (2.5):* Figure 5-15 (a) and (b) show the comparison between the magnitudes of $\tan\phi$ in the nanofilm and the nanowire with Akheiser damping calculated using Eq. (2.5). Here also, three different magnitudes of γ (1.2, 0.5 and 0.2) was considered to account for the uncertainties in the values of Akheiser damping. A qualitative comparison shows that our estimates of $\tan\phi$ fall directly between the values of Akheiser damping. No peak is observed in the frequency dependence of Akheiser damping.

- *Comparison of simulated damping with Eq. (2.6):* Figure 5-16 (a) and (b) show the comparison between the magnitudes of $\tan\phi$ in the nanofilm and the nanowire and Akheiser damping calculated using Eq. (2.6) at temperatures 300 K and 500 K. It can be clearly observed that Akheiser damping values calculated using Eq. (2.6) provide the best agreement with the simulated $\tan\phi$ values over the entire frequency range. Eq. (2.6) not only captures the magnitudes of $\tan\phi$, but also captures the presence of the peaks in damping at both the temperatures.

5.4 Discussions

Following are the key deductions from the discussions in the previous section: (a) TED in the nanofilm and the nanowire is significantly smaller than the simulated $\tan\phi$, (b) an increase in surface to volume ratio increased damping in the nanowire by 60% - 100% compared to the nanofilm, (c) the estimates of $\tan\phi$ are in the same range but not identical compared to the magnitudes of Akheiser damping, and (d) the peaks in Akheiser damping calculated using Eq. (2.6) are in the same frequency range compared to the peak frequencies of $\tan\phi$.

During the longitudinal oscillations of a structure, uniform spatial strain gradients are generated. Therefore, generally, the contribution of TED to the total damping in a longitudinally oscillating structure is small [148].

Akheiser damping arises from the heat transfer between different phonon modes of the structure. The physical origin of such heat flows lies in the difference of the mode dependent Grüneisen parameter (γ). Large difference between the Grüneisen parameter implies an increased energy exchange between different phonon modes, and therefore large damping. In a bulk crystal, there are only two phonon modes present namely the longitudinal and the transverse modes. Therefore, the magnitude of damping depends on the magnitude of the difference between the Grüneisen parameter of these two modes only. However, a deviation from the bulk case, (i.e. the nanofilm and the nanowire) leads to the generation of additional modes in the phonon spectrum. The presence of these additional modes will therefore contribute to an increase in the inter-modal heat transfer, hence, an increase in the energy dissipation. The magnitude of the extra damping will depend on the Gruneisen parameters of the additional phonon branches, the properties of the surface atoms, and the volume fraction of the surface atoms. Therefore, the increased damping in the nanowire is not surprising.

The discrepancy mentioned in observation (c) can be attributed to the following factors: (i) as discussed above, the Akheiser damping model is strictly valid for bulk solids, the nanoresonators investigated in this thesis had free surfaces which resulted in additional phonon damping by dissipation due to the extra phonon modes, (ii) the material properties used for calculating Akheiser damping had large spread, for example, the magnitude of k ranged between 350 W/m K and 255 W/m K at 300 K and 284 W/m K and 75 W/m K at 500 K, this inconsistency could have introduced

errors in our calculations, (iii) the occurrence of surface reconstruction in the free surfaces of both the structures could have led to additional surface mediated damping.

The Akheiser damping calculated using Eq. (2.5) and (2.6) is strictly valid in the case: $2\pi f\tau_p < 1$. This effect is captured in Figure 5-16, wherein the prediction of Akheiser damping increasingly deviates from the $\tan\phi$ estimates at frequencies away from the damping peak at both 300 K and 500 K. However, interestingly, Eq. (2.6) captures the trend of $\tan\phi$ over the entire frequency range. Additionally the magnitude of $\tan\phi$ also falls in the range of Landau-Rumer damping at frequencies smaller than the peak frequency. The physical origins of these observations are not clear.

A direct comparison between our simulated results and experimental measurements is difficult, because: (a) very few measurements of damping in single-crystal Si at the GHz regime are available in the literature, and (b) the available measurements do not specify the contributions of phonon damping.

5.5 Summary

This chapter presented results from the isothermal molecular dynamics simulations of damping in single-crystal Si nanoresonators as a function of frequency and temperature. The interactions between Si atoms were captured using the SW potential. Characteristic peaks were obtained in the damping spectrum as a function of temperature. Analysis of different sources of damping and a quantitative comparison of the simulated damping and Akheiser model showed satisfactory match. These results demonstrate the dominant role played by phonons in the dissipation of energy in

single-crystal nanoresonators. The performance of silicon nanoresonators can be significantly improved by operating them away from frequency dependent phonon damping peaks.

Chapter 6

Damping in amorphous silicon

The low temperature transport, thermodynamic and acoustic properties of amorphous materials are different from crystalline materials. The first measurement of damping peaks in fused silica was reported in 1953 [149, 150], later it was identified to be caused by structural relaxation of the glassy state [151]. Since then, damping measurements in glasses have mainly focused on two regimes: (i) very low temperatures (<10 K) and low frequencies [152, 153], and (b) very high frequencies below 300 K. Phenomenological models such as TLS [109, 154] have been used to explain these properties [155]. On the other hand, damping in glasses at temperatures above 10 K and at high frequencies in the range 1 GHz to 1 THz is not well understood [156, 157]. This is primarily because of the complexity arising from the presence of several mechanisms that can potentially cause damping [158]. In this chapter we report MD simulations of damping in an amorphous silicon nanofilm with dimensions identical to the single-crystal Si nanofilm discussed in Chapter 5. We use identical parameters for the SW potential to describe the interactions of silicon atoms in the amorphous phase. Damping simulations were performed at high frequencies (GHz regime) as a function of temperature. These results have been compared with damping estimates in the single-crystal silicon nanofilm. We point out possible mechanisms contributing to the damping.

Sections 6.1 describes the simulation methodology which includes a review of techniques used for obtaining a-Si using MD, the details of the thermal relaxation process, analysis used for characterizing the amorphous phase, simulation parameters used to ensure linearity, and

convergence of $\tan\phi$ and η in the subresonant regime. Section 6.2 includes the damping estimates in the amorphous structure as a function of frequency and temperature. The damping results are also compared with damping in the single-crystal Si nanofilm. In section 6.3 we discuss the results and make an effort to interpret the results by drawing comparison with experimental results. The chapter ends with a summary in section 6.4.

6.1 Simulation methodology

This section starts with a brief overview of the different techniques used for creating amorphous silicon (a-Si) in MD simulations. The details of the structural dimensions of the nanofilm, interatomic potential, and details of the thermal relaxation process are presented next. Also discussed are the results obtained from the analysis performed to characterize the amorphous silicon phase. The section ends with summarizing the simulation parameters used for calculating $\tan\phi$ and η in the subresonant regime.

6.1.1 Review of methods for creating amorphous silicon

In crystalline Si, every atom is tetrahedrally bonded to four nearest neighboring atoms giving four fold coordinated atoms. This structure is repeated over and over, forming a long range ordered lattice. In a-Si, however, this long range order is damaged. In contrast, there exists a random network of atoms, with fewer atoms retaining the four fold coordination of the crystalline phase. This randomness in the structure makes preparing an amorphous phase a difficult task in MD simulations.

Over the years, several methods have been proposed for generating a-Si in MD simulations. These methods can be broadly classified into three categories: the direct construction by bond switching method developed by Wooten, Winer and Weaire (WWW) [159, 160], the activation-relaxation (ART) method [161, 162] and the melting-and-quenching method [163-165]. In the first two techniques i.e. WWW and ART, the simulations start with a perfectly crystalline diamond cubic structure, which undergoes series of bond rearrangements according to a set of rules. These rules are chosen to achieve agreement with the continuous random network (CRN) model [166]. The melting-and-quenching method starts with a perfect crystalline structure, which is heated well above the melting point to obtain a liquid phase. The liquid phase is then rapidly quenched to the desired temperature to obtain the amorphous phase. The rate of cooling the liquid melt should be sufficiently large to restrict the atoms to diffuse back to the long range order of the crystalline phase [163].

These methods have different advantages and disadvantages. The disadvantage of the bond switching method is that even though effective for small system sizes, difficulties arise in the implementation when the number of atoms in the system is to the tune of thousands [167]. This is because increased number of force calculations (hundreds for each atom) are needed to be performed in order to reach the desired random configuration. The limitations of the ART method arises because the algorithm does not describe the thermal trajectory through phase space in detail [168].

The limitation of the melting-and-quenching technique originates from the inherent time scales associated with atomistic simulations. With current day computational resources, it is difficult to

perform simulations of cooling liquid melts at a rate less than 10^{10} K/s. Nevertheless, instead of this limitation, in several studies, the melting-and-quenching method has been found to be a viable method for obtaining the amorphous silicon phase. Also, the melting-and-quenching method does not necessitate assumptions about the configuration of atoms in the amorphous phase [164, 169]. These considerations motivated us to adopt the melting-and-quenching method for creating the amorphous silicon phase.

6.1.2 Structural details

The starting structure consisted of Si atoms arranged in a body-centered tetrahedral (BCT) lattice with lattice parameter of 5.43 Å. A Cartesian coordinate system was attached to the structure with the x, y, and z axes oriented along the [1 0 0], [0 1 0], and [0 0 1] directions, respectively. The structural dimensions, and the boundary conditions of the a-Si nanofilm were identical to the single-crystal Si nanofilm mentioned in Chapter 5.

6.1.3 Interatomic potential for obtaining amorphous silicon

Several interatomic potentials [88, 135, 170, 171] including the SW potential [162, 167, 172, 173] have been used to simulate the amorphous phase of silicon. The a-Si obtained using SW potential has a high-density liquid-like structure which is characterized by a shoulder on the second-neighbor peak of the radial distribution function (RDF) and a large fraction of over-coordinated atoms [174, 175], which has not been observed in experiments. A solution suggested to this problem is to increase the three-body term by 50% to 100% [161, 176]. In addition, a comparison with the experimental measurements of the elastic constants for a-Si shows that the SW potentials

fail to produce the elastic constants for a-Si accurately. Also, to be able to compare damping in c-Si and a-Si for the same structure, the SW potential was used unchanged.

6.1.4 Thermal equilibration

The NH thermostat was used for generating and equilibrating the a-Si phase using a τ_{NH} of 0.01 ps. In order to obtain the amorphous phase, the initial crystalline phase at 1 K was first melted at 3000 K followed by rapid quenching to 300 K. This is achieved by implementing the following steps. First, the temperature of the c-Si structure was raised to 3000 K in 0.05 ns, followed by equilibration at 3000 K for another 1 ns. Quenching the molten Si atoms to 300 K was carried out in two steps. The liquid Si phase was first cooled down to 1000 K using a cooling rate of 40 K/ps. The transition from the liquid to the amorphous state occurred during this step [173]. Next, the a-Si phase was annealed at 1000 K for another 2 ns. Finally, the amorphous structure was cooled to 300 K in 0.002 ns, and equilibrated to ensure the atoms reach equilibrium potential energy and pressure. Once equilibrated, selected atoms were removed from the simulation box to obtain desired dimensions for the amorphous nanofilm. Clamping condition was imposed by freezing the motion of the first two atomic layers from $x = 0$ in the axial direction. Schematic illustrations of the initial c-Si structure, the liquid Si phase, and the a-Si nanofilm at 300 K are shown in Figure 6-1(a), (b), and (c) respectively.

Figure 6-2, shows the variation of pressure in the lateral directions of the a-Si nanofilm at 300 K as a function of time. The mean value of pressure in the lateral directions were tensile 5050 Bar and 4800 Bar respectively. The reason behind such pressure build-ups is not clear yet. However, the tensile nature of the pressure indicates that there was an increase in the density of the Si atoms

in the amorphous phase compared to the c-Si phase which caused a decrease in the volume of the structure. Further analysis confirmed a density of 2.56 g/cm^3 for the a-Si nanofilm, an increase of 10% from the density of the c-Si nanofilm. In order to avoid such pressure build-ups, the equilibrium lattice spacing for the a-Si was identified.

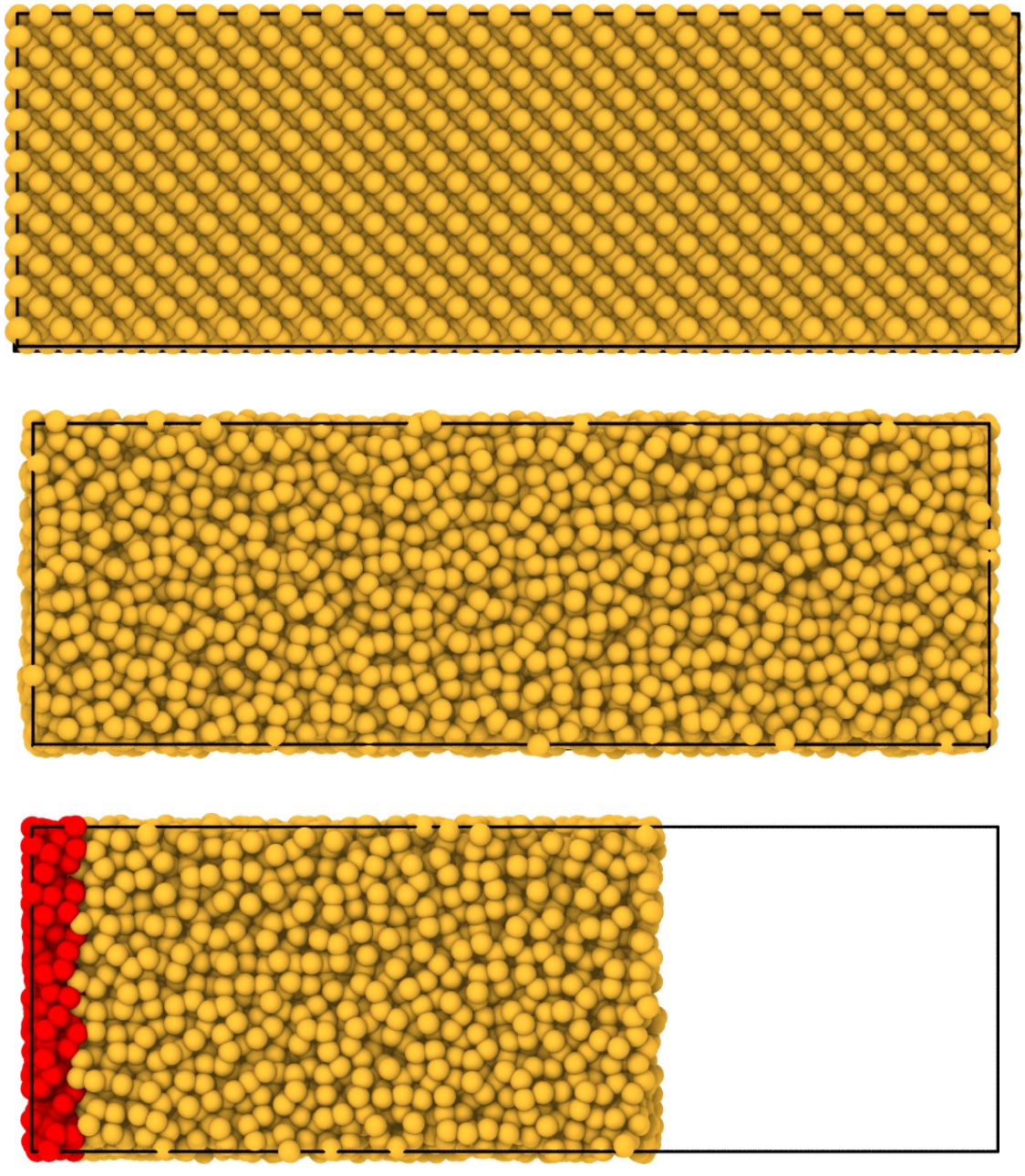

Figure 6-1: Schematic illustration of atomic configurations in (a) the initial c-Si structure, (b) the liquid silicon, and (c) the a-Si nanofilm. The clamped atoms are shown in red.

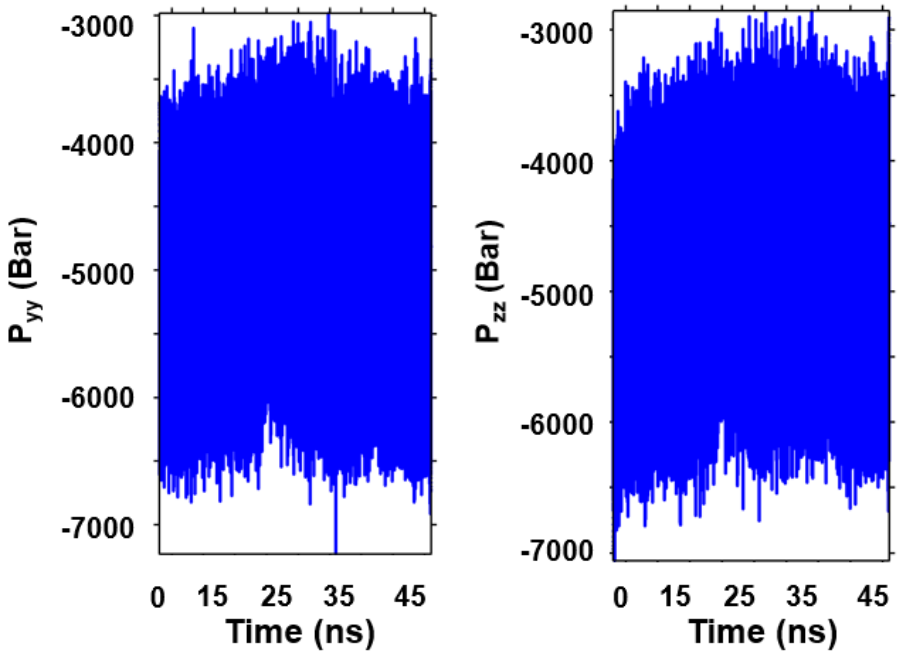

Figure 6-2: Variation of pressure in the lateral directions for the lattice spacing 5.43 Å. The mean pressure in the y (P_{yy}) and z (P_{zz}) direction from 30 ns till 45 ns were tensile 5050 Bar and tensile 4800 Bar respectively.

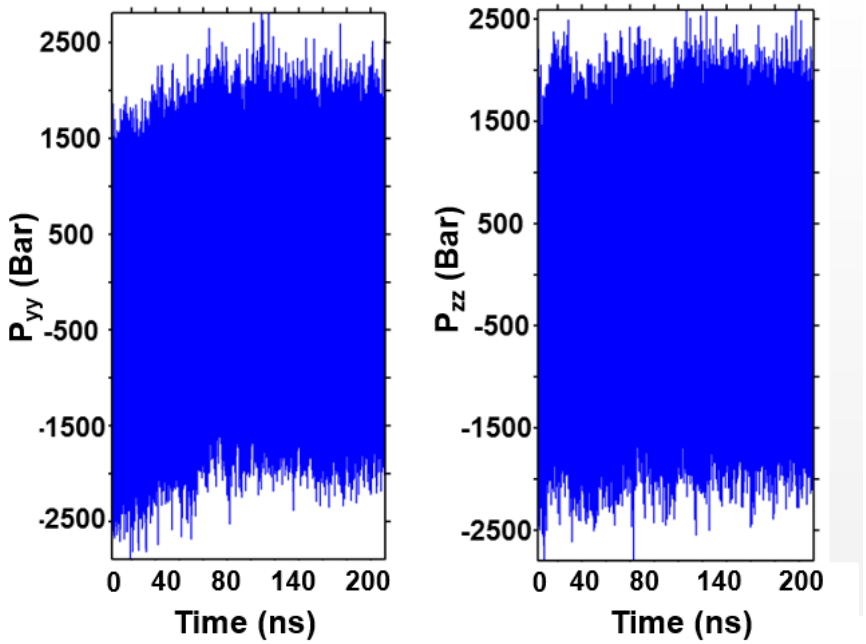

Figure 6-3: Variation of pressure in the lateral directions for the lattice spacing 5.283 Å. The mean pressure in the y (P_{yy}) and z (P_{zz}) direction from 100 ns till 220 ns were compressive 85 Bar and compressive 43 Bar respectively.

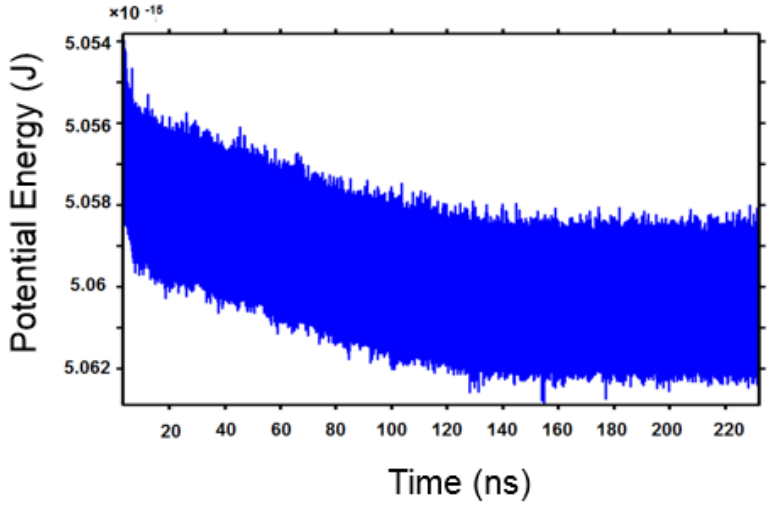

Figure 6-4: Time trace of the potential energy in the a-Si nanofilm as a function of time for lattice spacing 5.283 Å. It can be seen that the potential energy reached equilibrium after 145 ns.

Experimental measurements of damping in vitreous silica indicate that a high pressure in the structure influences the distribution of barrier heights of TLSs [177]. Therefore, in order to avoid the influence of pressure, a set of lattice parameters were selected and the a-Si nanofilm was created following the melting-and-quenching steps. The magnitudes of the mean pressure in the lateral directions were calculated for each simulation. The optimum value of the lattice parameter was selected using the method of trial and error. It was found that for a lattice parameter of 5.283 Å, the magnitudes of the mean pressure in the y and z directions were of 85 and 43 Bar at 300 K. The corresponding plots of the pressure in the y and z directions as functions of time are shown in Figure 6-3. Figure 6-4 shows that the a-Si phase reached equilibrium potential energy in 150 ns.

The atomic configuration in the nanofilm at 300 K was used to obtain the amorphous phase at temperatures below 300 K. Equilibrium lattice parameters were obtained in each case by rescaling the simulation cell size to avoid high pressures in the simulation cell.

6.1.5 Characterization of the amorphous phase

In general, structural properties of amorphous phases are characterized in terms of the radial distribution function ($g(r)$), and bond order parameters. In this section, we present a detailed analysis of these parameters, and their distributions in the a-Si nanofilm. The radial distribution function showed characteristic smooth peaks as a function of radial distance. The bond order parameters revealed that the bct lattice of the crystalline phase was destroyed in the amorphous phase.

6.1.5.1 Radial distribution function (*g(r)*)

Radial distribution function (RDF) is a common method for analyzing the distribution of atoms in any structure [178]. For a group of atoms, the radial distribution function, $g(r)$, is defined as the likelihood of finding a particle at distance r from another particle. The RDF is obtained by calculating the number of particles within a distance of r and $r + dr$ for every particle in the group, and binning them into a histogram.

The RDF as a function of the distance between atoms shows characteristic peaks. These peaks correspond to groups of neighbors surrounding each atom. The RDF for the a-Si phase was calculated using the VMD [179] software by analyzing the atomic trajectories obtained from the MD simulations.

Figure 6-5 shows the RDF for the a-Si phase at 300 K (red line), also shown is the same plot is the RDF for c-Si (black line) at 300 K. The following observations can be made from Figure 6-5: (a) the c-Si system had more number of peaks in the RDF compared to a-Si, (b) a-Si phase had 3 peaks in the RDF with each of them smaller than the preceding one, with the first peak having a deep valley, (c) the location of the first peak in the RDF for both c-Si and a-Si appeared at the same distance of 2.35 Å, and (d) after a distance of 6 Å the long range order was broken in the amorphous phase. The RDF is also used to find the cut-off distance for calculating coordination number distribution. This cut-off given by the first minimum value in RDF, was found to be 2.45 Å in a-Si, which matches with the value reported in the literature for SW potential [180]. Figure 6-6 shows the effect of cooling rate on the RDF. It can be seen that the intensity of the peak at $r = 2.45$ Å is the smallest for the largest cooling rate, implying maximum irrecoverable disorder caused by smaller time for diffusion. The intensity of this peak increases as the cooling rate is reduced as there is more time for the diffusion of the Si atoms through the structure.

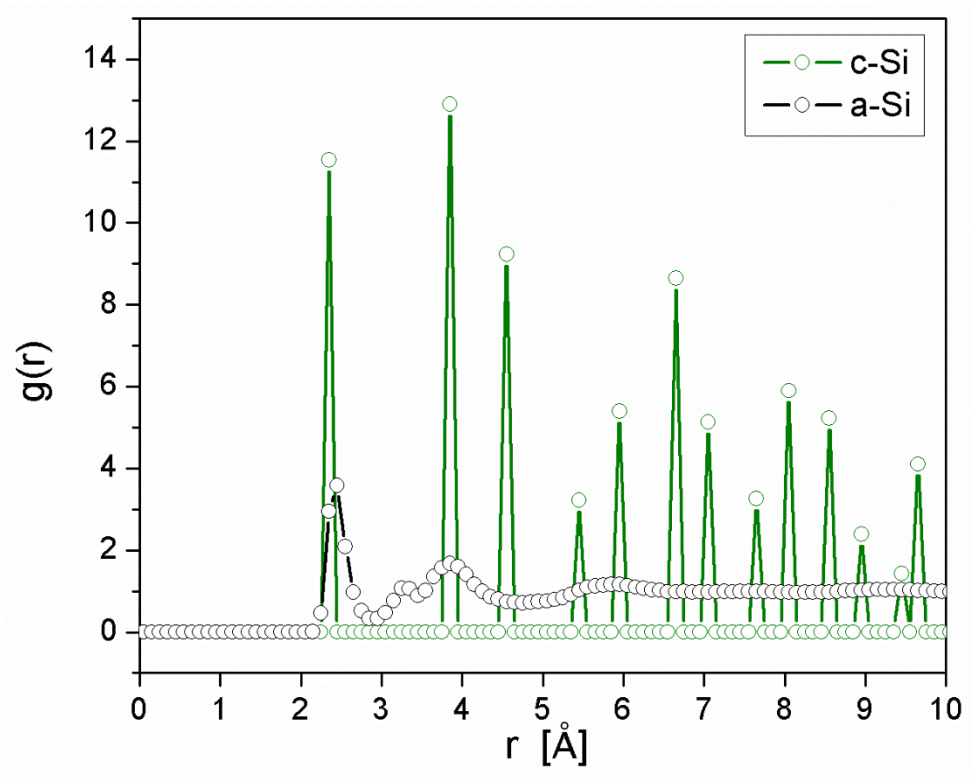

Figure 6-5. The radial distribution functions (RDFs) for c-Si (green) and as-quenched a-Si (black) system at 300 K.

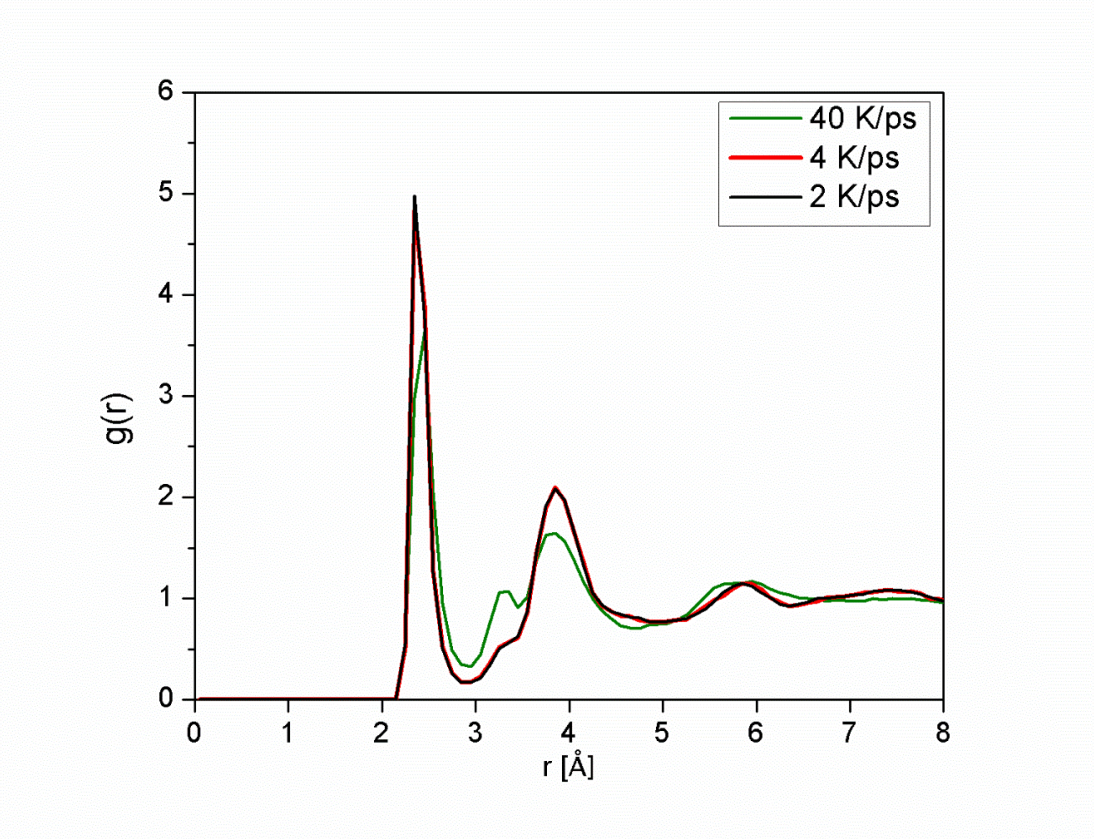

Figure 6-6. Radial distribution function for three different a-Si structures obtained using different cooling rates. Different colors represent different cooling rates.

6.1.5.2 Bond order parameters

Bond-order parameters are extensively used for quantifying the extent of disorder in amorphous structures [181-183]. These parameters are useful in distinguishing particles in a solid environment from those in a liquid, and therefore can be used for identifying different crystalline phases without requiring any knowledge about the initial structure. The bond order parameters describe the symmetry of the bond orientations regardless of the bond lengths [184], and are calculated using the spherical harmonic functions, Y_{lm}. The definition of the complex vector $q_{lm}(i)$ for particle i is given as [183]

$$q_{l,m}(i) = \frac{1}{N_n(i)} \sum_{j=1}^{N_n(i)} Y_{lm}(\vec{R}_{ij}), \tag{5.1}$$

where N_n is the number of particles within a given radius $r_{nb} = 1.2r_0$ (where r_0 is the position of the first peak in the radial distribution function for the structure) around particle i, $\vec{R}_{ij}$ is the unit vector connecting atom i with each of its N_n neighboring atoms j, l is a free integer parameter and m is an integer that runs from $m = -l$ to $m = +l$.

The rotational invariants of the bond-order parameters are given by [183]

$$q_l(i) = \left[\frac{4\pi}{2l+1} \sum_{m=-l}^{l} |q_{lm}(i)|^2 \right]^{\frac{1}{2}}. \tag{5.2}$$

The bond order parameters are found to distinguish between solid-like and liquid-like atoms. These quantities depend on the angles between the vectors related to the neighboring atoms. Therefore these parameters are independent of a reference frame.

Different methods have been developed depending on the local bond order parameters for analyzing the crystalline structure in liquid and solid phases. For example, the bond order parameters are sensitive to the crystal structure depending on the choice of l. For example, $l = 6$, is used to detect atoms experiencing fcc and hcp-like surroundings. This is because the hexagonal planes in these lattices have six-fold symmetry.

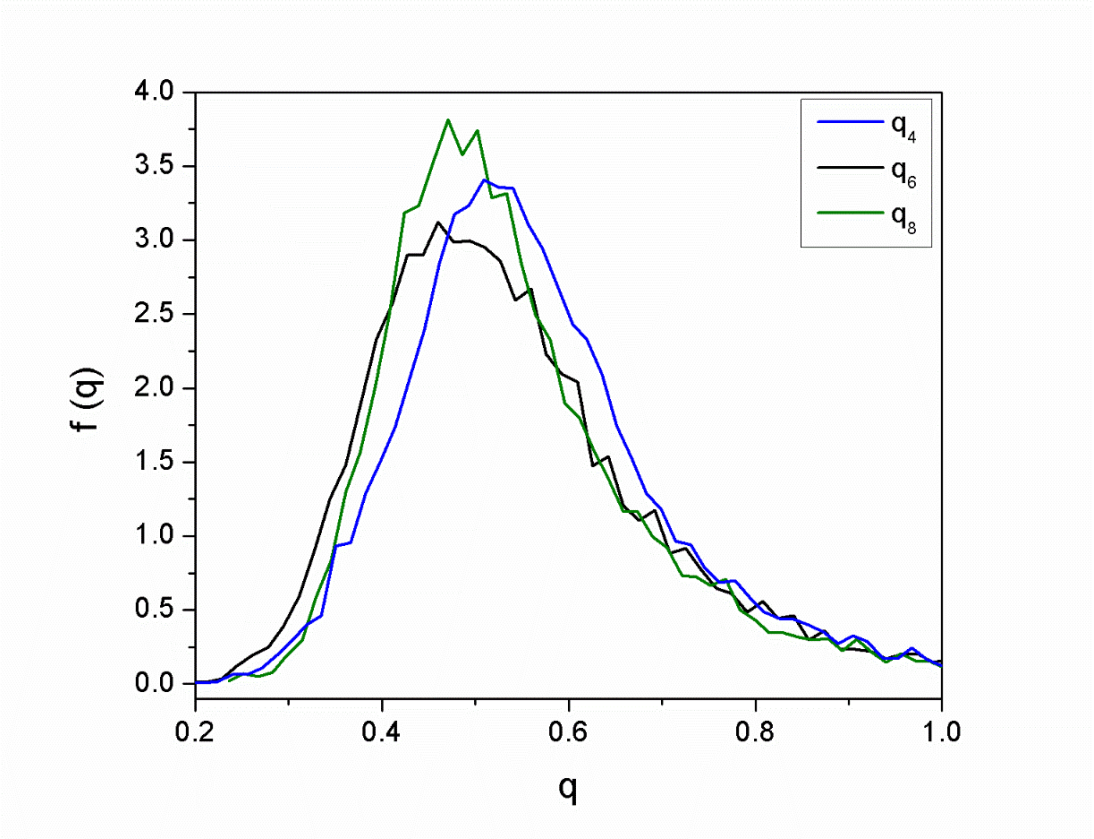

Figure 6-7. The distribution of the local bond order parameters q_4, q_6, and q_8, for the a-Si phase at 300K.

The values of $q_4(i)$, $q_6(i)$, and $q_8(i)$ for perfect structures at 0 K and 300 K calculated in this work along with their values in the literature are listed in Table 6-1. The table also contains the values for the bond order parameters for the a-Si and c-Si phase. Figure 6-7 shows the histogram of q_4, q_6, and q_8 for the atoms in the a-Si phase.

The average q_6 for c-Si and a-Si was calculated as 0.7725 and 0.554. These numbers indicated a loss of order in the amorphous phase. The value of 0.554 for the q_6 in a-Si is in good agreement of 0.45 at 1000 K for 2-D a-Si obtained using cooling rate of 10.8 K/ ps [184].

Table 6-1: Average values of q_4, q_6, and q_8 for different local environments at 0 K and 300 K.

Bond order parameter		FCC	BCC (300 K)	c-Si (300 K)	a-Si (300 K)
q_4	Current work	0.0364	0.1909	0.7115	0.575
	Literature	0.036 [183]	0.191 [183]		
q_6	Current work	0.5106	0.5745	0.7725	0.554
	Literature	0.511 [183]	0.575 [183]		
q_8	Current work	0.4293	0.4039	0.603	0.552
	Literature	0.429 [183]	0.404 [183]		

6.1.6 Natural frequency (f_0) and axial stiffness (K_x)

The FFT of the thermal noise captured for the layer at $x = l_x$ produced resonance peak for the first longitudinal mode at 284.5 GHz. The force displacement curve obtained by applying static forces on the atoms in the end layer is shown in Figure 6-8. The figure shows that the structure exhibited an initial linear elastic region followed by nonlinear deformation beyond a force magnitude of 18 nN.

Figure 6-9 shows the response of the a-Si nanofilm for static force 24 nN. It can be seen that the nanofilm progressively deformed with time as the force was applied. Axial stiffness was obtained by fitting a straight line to the linear portion (shown by arrows) of the force-displacement curve shown in Figure 6-8. The stiffness of the structure was found to be 389 N/m at 300 K.

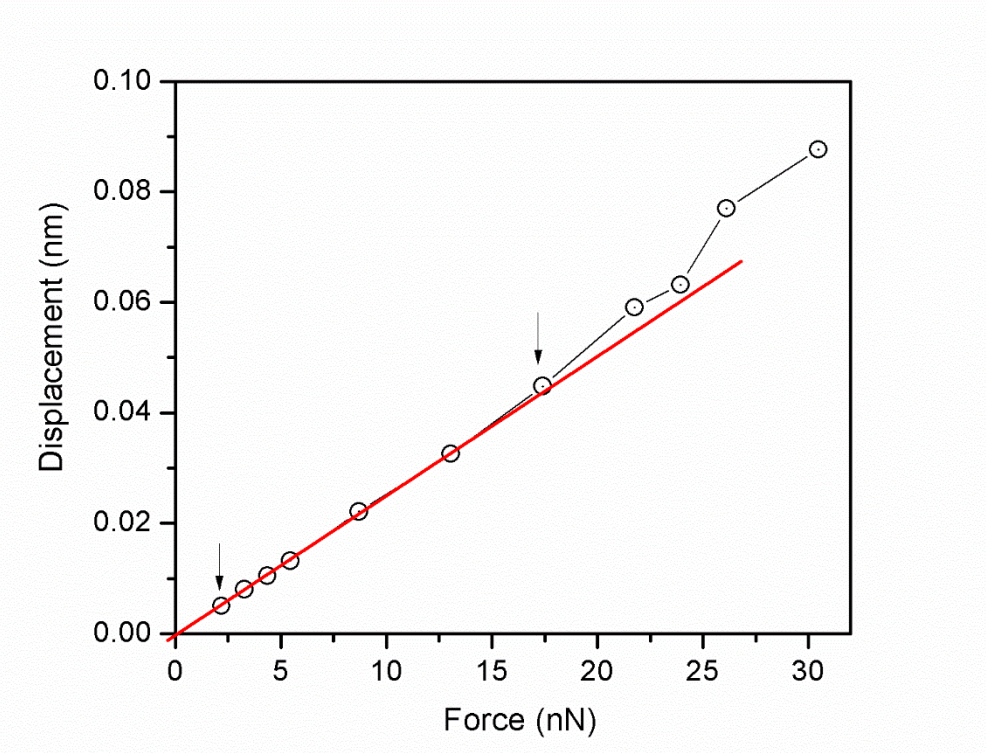

Figure 6-8: Force-displacement curve for the nanofilm used for estimating the axial stiffness.

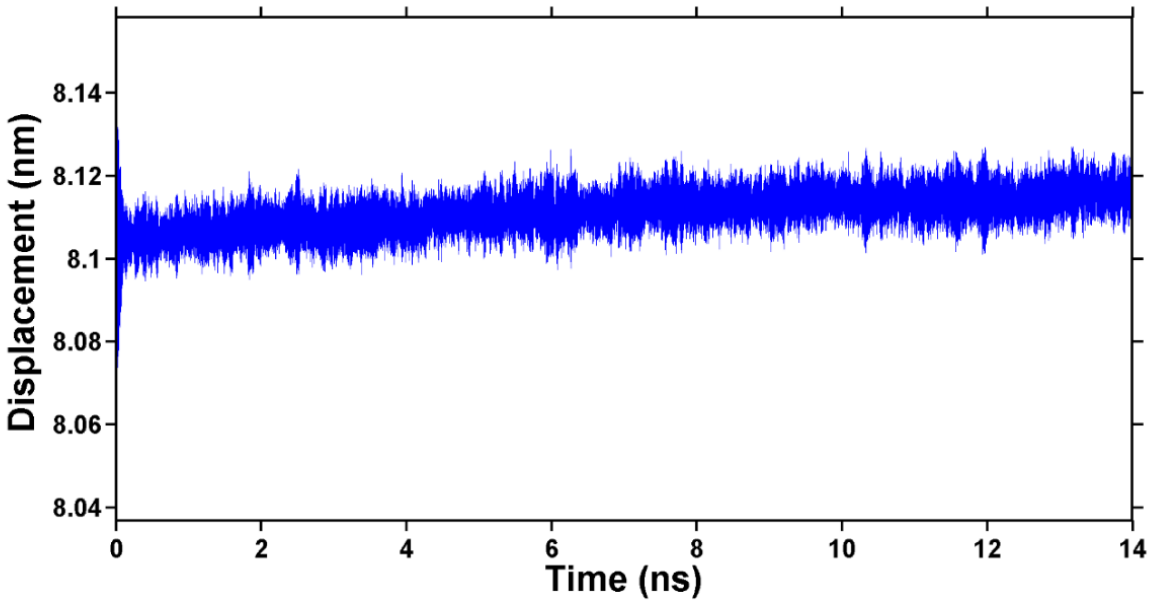

Figure 6-9: Time series of displacement for the a-Si nanofilm for static force 24 nN. The film progressively deforms as the load is applied.

6.1.7 Damping in the subresonant regime

Damping in the a-Si nanofilm in the subresonant regime was estimated using $\tan\phi$ and η.

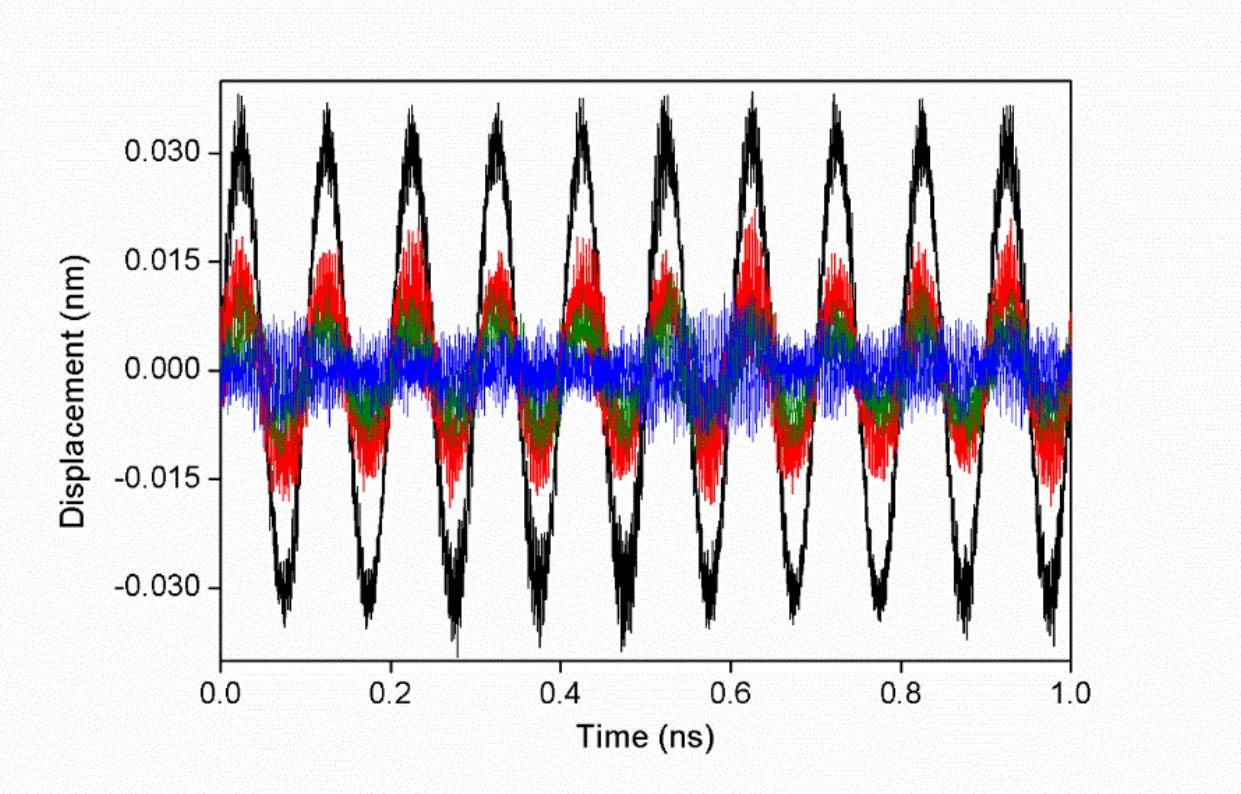

Figure 6-10: Axial displacement of the free end of the nickel nanofilm at 10 GHz. The blue curve shows the thermomechanical noise in the absence of any external driving force. The green, red and black curves correspond to force amplitudes of 2.1 nN, 4.3 nN, and 13 nN respectively.

Figure 6-10 shows the response of the nanofilm undergoing harmonic oscillations for different force magnitudes, also shown in the same plot is the time trace of thermal noise. It is seen that for forces above 2 nN, the response of the structure surpasses the thermomechanical noise floor. The stress-strain plots obtained from the static tensile tests are shown in Figure 6-11. It can be concluded that for stresses up to 0.97 GPa (17 nN) the response of the nanofilm was linear.

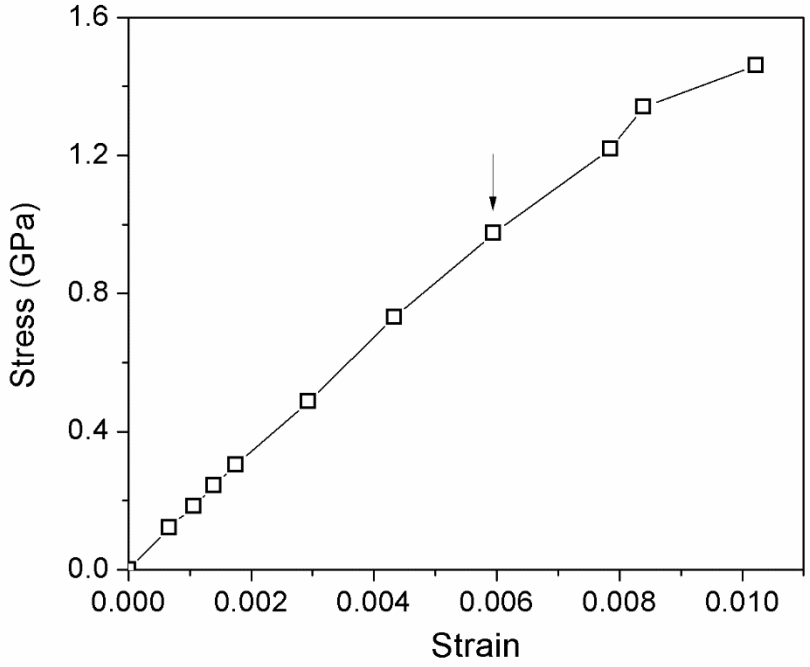

Figure 6-11: Stress-strain curve for the nanofilm in the axial direction at 300 K. The magnitude of the static force varies between 2 nN and 30 nN. The deviation of the trend from the elastic behavior take place for forces larger than beyond 17 nN (shown by the arrow) which corresponds to a strain of 0.6%.

The convergence behavior of $\tan\phi$ and η for the longitudinal mode in the a-Si nanofilm for different harmonic forces with frequency 10 GHz is shown in Figure 6-12. The following observations are made from the figure. For small values of F_0, the harmonic response is comparable to the thermal noise floor (1 nN and 2 nN), and the simulations are slow to converge. As the force amplitude is gradually increased, the simulations converge in the linear regime. As the force is further increased, the damping values converge fast (4.3 nN to 17.4 nN). For forces larger than 17 nN, damping values converge faster but are large. A force of 4.3 nN was selected

for damping analysis since it was found to be the smallest force for which damping converged, and the difference between $\tan\phi$ and η was less than 7%.

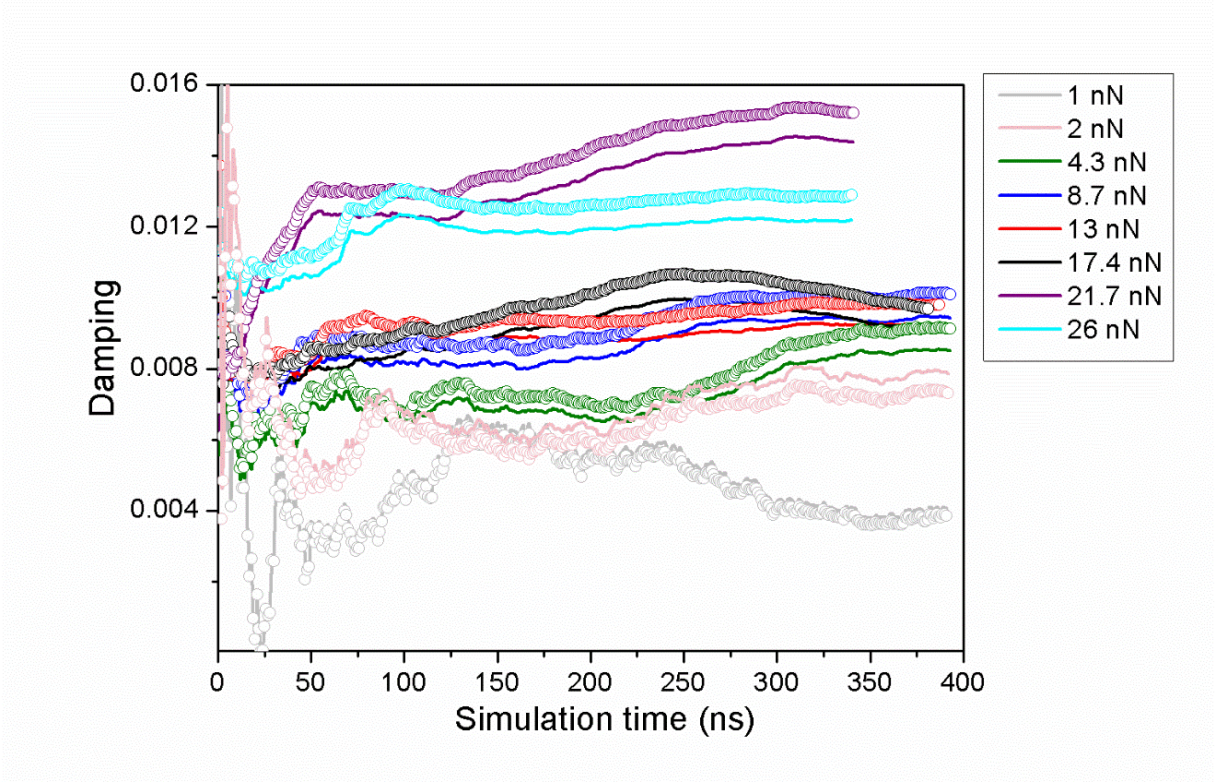

Figure 6-12: Convergence behavior of the loss tangent ($\tan\phi$) and the loss factor (η) in the nanofilm for longitudinal-mode oscillations at 10 GHz. The markers represent the loss factor (η) and the solid lines represent the loss tangent ($\tan\phi$). Both measures were computed after every nanosecond. In all cases, $\tan\phi$ and η differed by less than 7%.

6.2 Results

In this section we discuss the results obtained for the damping simulations in the a-Si nanofilm for oscillations in the longitudinal mode. MD simulations were performed as a function of temperature and frequency. Frequency response of damping was simulated at 300 K and was compared with that of the c-Si nanofilm. Damping in the a-Si nanofilm as a function of temperature (15 K$\leq T \leq$300 K) at 10 GHz revealed two peaks.

6.2.1 Comparison of damping in a-Si and c-Si nanofilms at 300 K

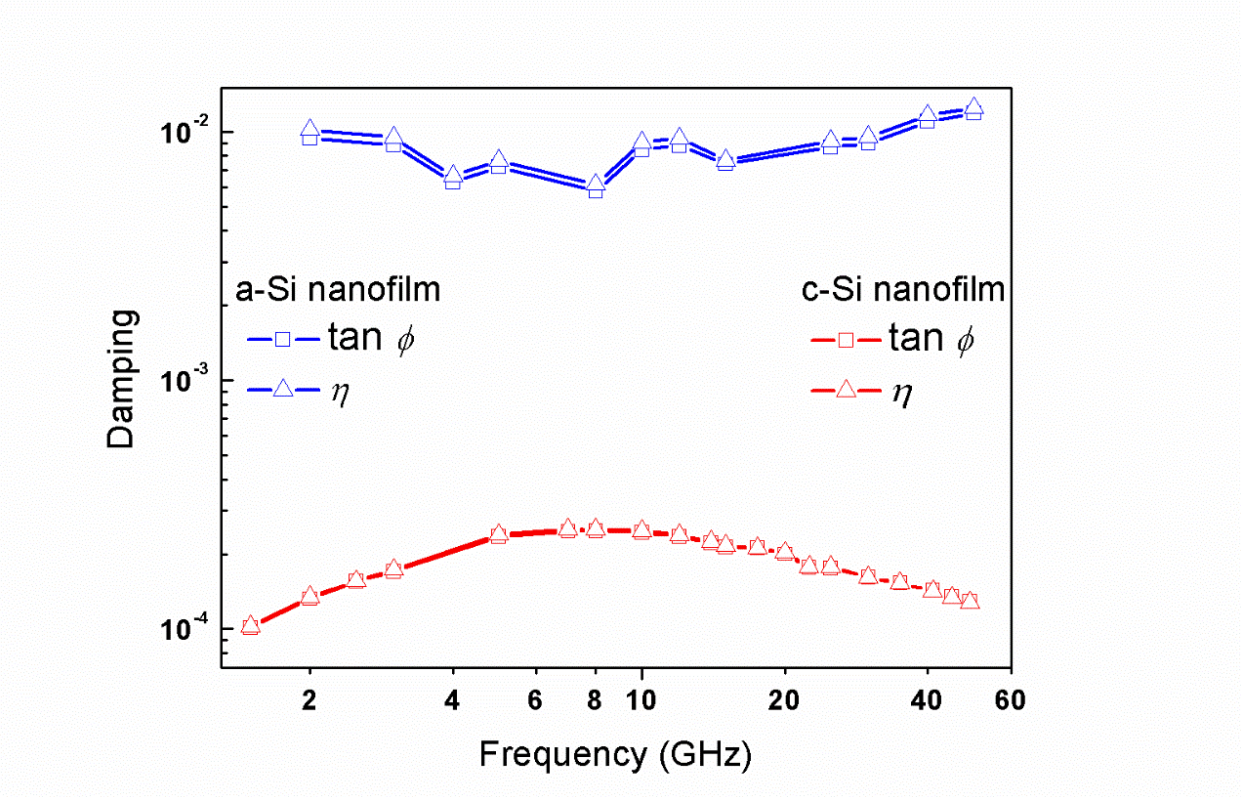

Figure 6-13: Frequency response of damping in the a-Si nanofilm (shown in blue), and the c-Si nanofilm (shown in red) for longitudinal mode vibrations. The magnitude of the harmonic force applied on the a-Si and c-Si nanofilms were 4.3 nN and 49 nN respectively. The magnitudes of $\tan\phi$ and η differed by less than 2% in the c-Si nanofilm, and less than 7% in the a-Si nanofilm over the entire frequency range.

Frequency dependent damping in the a-Si nanofilm in the longitudinal mode for the harmonic force 4.3 nN as a function of frequency at 300 K is plotted in Figure 6-13. It can be seen that damping is a weak function frequency at 300 K. The minimum and the maximum difference between $\tan\phi$ and η over the frequency range of 2 GHz to 50 GHz was between 4% and 8%. In the same figure we have plotted the magnitudes of $\tan\phi$ and η for the c-Si nanofilm at 300 K. From the figure it can be noticed that for identical structural dimensions, boundary conditions, and

clamping conditions the damping in the a-Si nanofilm was orders of magnitude more than the c-Si nanofilm. For the entire frequency range the converged values of $\tan\phi$ and η in the a-Si nanofilm are given in Table 6.2.

6.2.2 Damping in a-Si nanofilm as a function of temperature

The effect of temperature on the damping in the a-Si nanofilm is illustrated in Figure 6-14. Starting from the atomic configurations at 300 K, the a-Si structure was first equilibrated at various temperatures in the range 15 K and 300 K. Previous experimental measurements in vitreous silica indicated that damping at ultrasonic frequencies is dependent on the external pressure [185]. Therefore, in order to minimize effects from the pressure build ups in the lateral directions, the size of the simulation box was adjusted and equilibrium lattice parameters were obtained for every temperature. The magnitudes of axial stiffness at all the temperatures were obtained following the procedure discussed in Section 6.1.6.

Over the entire temperature range, for oscillations at 10 GHz the difference between $\tan\phi$ and η was less than 7%. Following observations can be made from the figure: (a) over the entire temperature range the damping in the structure increased by a factor of 10, but this trend was not monotonic, (b) as the temperature of the nanofilm was increased above 15 K damping also increased till 50 K and then started to decrease until 70 K. After 70 K, damping in the structure increased monotonically and maximized at 150 K, (c) at temperatures between 150 K and 275 K overall damping in the structure reduced with increasing temperature. The temperatures at which damping peaks are observed are shown as P_1 and P_2 in the same figure. For the entire temperature range the converged values of $\tan\phi$ and η in the a-Si nanofilm are given in Table 6.3.

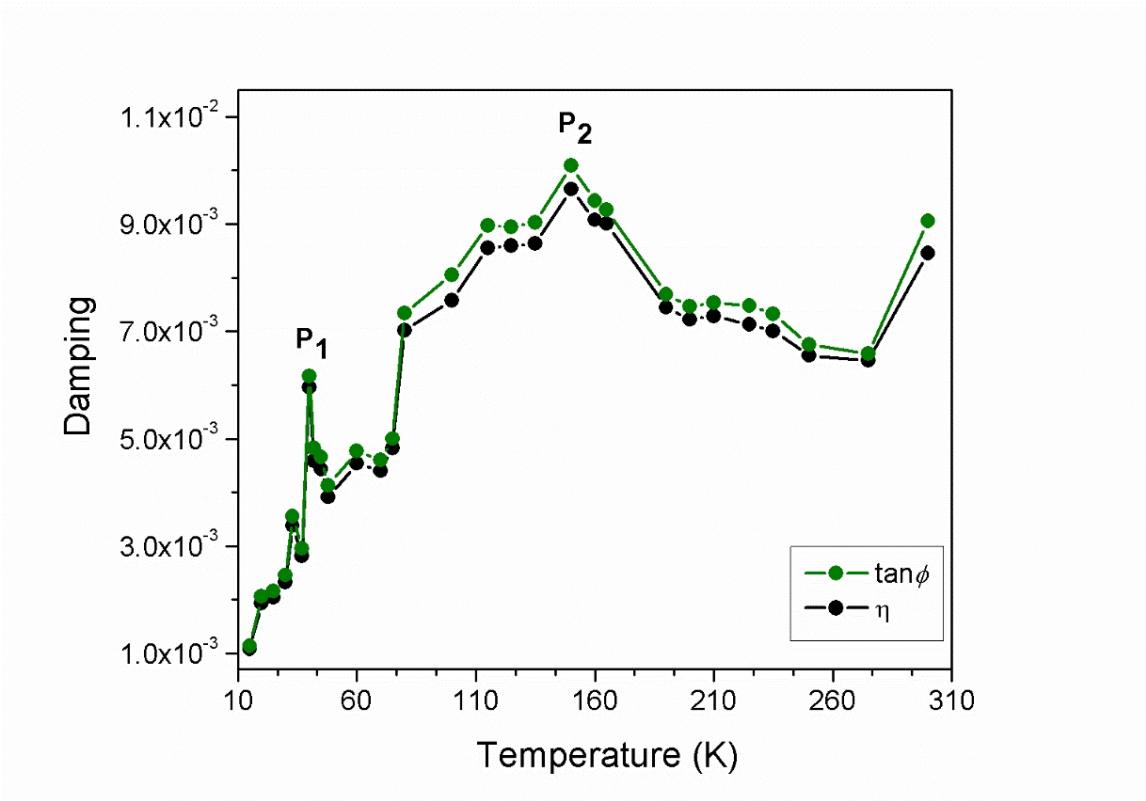

Figure 6-14: Damping in the nanofilm for temperatures ranging between 15 K and 300 K for longitudinal mode oscillations at 10 GHz. The magnitude of the harmonic force applied on the a-Si was 4.3 nN. The magnitudes of $\tan\phi$ and η differed by less than 7% over the entire temperature range.

Table 6.2: Damping in the a-Si nanofilm as a function of frequency at 300 K for the longitudinal-mode oscillation.

Frequency (GHz)	Total simulation time, t_f (ns)	Convergence time, t_c (ns)	$\tan\phi$	η	$\frac{\tan\phi-\eta}{\tan\phi}\times 100$
2	309	288	9.48×10^{-3}	1.02×10^{-3}	7.17
3	350	304	8.86×10^{-3}	9.50×10^{-3}	7.21
4	243	227	6.25×10^{-3}	6.66×10^{-3}	6.52
5	243	162	7.21×10^{-3}	7.66×10^{-3}	6.24
8	243	178	5.77×10^{-3}	6.14×10^{-3}	6.40
10	393	328	8.46×10^{-3}	9.05×10^{-3}	6.99
12	276	217	8.81×10^{-3}	9.43×10^{-3}	7.01
15	161	135	7.41×10^{-3}	7.67×10^{-3}	3.47
25	242	154	8.67×10^{-3}	9.20×10^{-3}	6.20
30	243	104	8.99×10^{-3}	9.55×10^{-3}	6.22
40	243	207	1.10×10^{-2}	1.17×10^{-2}	6.08
50	243	218	1.19×10^{-2}	1.25×10^{-2}	4.94

Table 6.3: Damping in the a-Si nanofilm as a function of temperature for oscillations in the longitudinal-mode at 10 GHz.

Temperature (K)	Total simulation time, t_f (ns)	Convergence time, t_c (ns)	$\tan\phi$	η	$\frac{\tan\phi-\eta}{\tan\phi}\times 100$
15	258	131	1.09×10^{-3}	1.14×10^{-3}	4.83
20	256	96	1.94×10^{-3}	2.06×10^{-3}	6.17
25	271	83	2.04×10^{-3}	2.16×10^{-3}	5.86
30	257	68	2.32×10^{-3}	2.46×10^{-3}	5.81
33	214	51	3.38×10^{-3}	3.56×10^{-3}	5.20
37	215	110	2.81×10^{-3}	2.95×10^{-3}	4.84
40	223	64	5.96×10^{-3}	6.17×10^{-3}	3.51
42	402	129	4.58×10^{-3}	4.82×10^{-3}	5.16
45	390	193	4.44×10^{-3}	4.66×10^{-3}	4.94
48	264	86	3.91×10^{-3}	4.13×10^{-3}	5.70
60	284	133	4.54×10^{-3}	4.77×10^{-3}	5.04
70	291	234	4.40×10^{-3}	4.60×10^{-3}	4.60
75	272	135	4.83×10^{-3}	5.00×10^{-3}	3.59
80	239	101	7.02×10^{-3}	7.34×10^{-3}	4.55
100	335	285	7.58×10^{-3}	8.05×10^{-3}	6.30
115	246	139	8.56×10^{-3}	8.97×10^{-3}	4.81
125	272	153	8.59×10^{-3}	8.94×10^{-3}	4.10

Table 6.3 continued

Temperature (K)	Total simulation time, t_f (ns)	Convergence time, t_c (ns)	$\tan\phi$	η	$\frac{\tan\phi-\eta}{\tan\phi}\times 100$
135	358	244	8.34×10^{-3}	8.73×10^{-3}	4.62
150	270	89	9.65×10^{-3}	1.01×10^{-2}	4.52
160	315	93	9.08×10^{-3}	9.44×10^{-3}	3.97
165	312	289	9.01×10^{-3}	9.26×10^{-3}	2.82
190	243	190	7.45×10^{-3}	7.69×10^{-3}	3.31
200	270	206	7.22×10^{-3}	7.47×10^{-3}	3.41
210	303	263	7.29×10^{-3}	7.54×10^{-3}	3.44
225	338	200	7.12×10^{-3}	7.48×10^{-3}	5.02
235	320	144	7.01×10^{-3}	7.32×10^{-3}	4.53
250	249	147	6.55×10^{-3}	6.76×10^{-3}	3.15
275	251	207	6.46×10^{-3}	6.58×10^{-3}	2.00

6.3 Discussion

The results from the MD simulations of damping in the a-Si nanofilm can be summarized as follows.

(1) No clear trend could be observed in the magnitudes of $\tan\phi$ for the longitudinal oscillations in a-Si nanofilm at 300 K over the frequency range 2-50 GHz. The magnitude of damping over the entire frequency range stayed between 9.48×10^{-3} and 1.19×10^{-2} -which is orders of magnitude larger than the damping in the c-Si nanofilm for similar temperature and frequencies.

(2) Damping as a function of temperature for oscillations at 10 GHz showed two peaks, a narrow peak at 40 K (P_1) and another broad peak at 150 K (P_2).

In order to interpret the simulated results, let us start the discussion by considering observation (1). Amorphous materials are usually more damped than their crystalline counterparts, for example, at 300 K and 35 GHz damping in vitreous silica (damping = 4×10^{-3}) is nearly 4 times that of quartz at 40 GHz (damping =1.4×10^{-3}) [186]. Recent room temperature measurements at 50 GHz and 100 GHz also report a 6 to 7 times more damping in thin films of a-Si compared to c-Si thin film [157]. However, our estimate of $\tan\phi$ (1.19×10^{-2}) at 300 K and 50 GHz is about an order larger than the damping in the a-Si thin film ($1.2\times10^{-3}\pm5.9\times10^{-4}$) reported in Ref. [157]. Possible explanations for this discrepancy are: (a) difference in the material properties and the film thicknesses of the nanofilm reported in this thesis and those in Ref. [157], and (b) the possibility of hydrogen contamination in the a-Si film reported in Ref. [157].

In order to calculate frequency dependent Akheiser type phonon damping in a-Si, Fabien and Allen calculated mode dependent Gruneisen constant for a SW a-Si structure with WWW coordinates [187, 188]. Their model considered internal strain in the a-Si which originates from the random atomic positions in amorphous systems. The internal strain produces large anomalous Gruneisen parameter (as large -30) in certain low-frequency resonant modes in a-Si. Their calculated frequency dependent phonon damping in a-Si at 300 K with and without internal strain and our $\tan\phi$ estimates are presented in Table 6.4. It can be seen that $\tan\phi$ estimates are larger than the calculated Akheiser-type phonon damping below 15 GHz, however a better agreement is present above 15 GHz.

A direct comparison of observation (2) with published literature is not possible due to the unavailability of experimental damping measurements in a-Si at 10 GHz as a function of temperature. Nevertheless, an indirect comparison can be made with the low frequency measurements. The damping peak P_2 (see Figure 6-14) bears resemblance to the low frequency (5 KHz) broad peak at 130 K reported in Ref [155, 189] and 270 K peak at 300 MHz in Ref [190]. In order to compare the activation energies of the underlying relaxation processes, P_2 was fit to an Arrhenius type equation, $\tau = \tau_0 \exp\left(\frac{E}{k_B T}\right)$, where τ_0 is assumed to be 10^{-13} for a-Si [190]. The fit produced E = 70 meV as opposed to 200 meV for the peak reported in Ref [155, 190]. Further calculations predict that the 200 meV peak should appear at 426 K for the longitudinal oscillations of a-Si nanofilm at 10 GHz; this temperature range was not probed in this thesis.

An indirect comparison of temperature dependent magnitudes of $\tan\phi$ can be made with the Brillouin-scattering measurements of damping in vitreous silica. Such a comparison shows two striking similarities, (a) in the temperature range of 15 K to 300 K, the range of $\tan\phi$ (1.09×10^{-3} – 9.65×10^{-3}) at 10 GHz is of similar order compared to damping in vitreous silica at 35 GHz (1.3×10^{-3} and 5.8×10^{-3}), and (b) the temperature dependent trend of $\tan\phi$ at 10 GHz resembles the trend in damping in vitreous silica at 30 GHz. For example, damping in vitreous silica as a function of temperature shows a hump at 40 K and a broad peak at 135 K similar to P_1 and P_2 (see Figure 6-14). Foret *et al.* [158] calculated the magnitude of damping due to TLS and obtained reasonable agreement with experimental measurements. However, it should be noted that the above mentioned similarities between the damping estimates in the a-Si nanofilm and the experimental measurements of damping in vitreous silica can be fortuitous because the state of disorder can be

different in these two material systems. Therefore, mechanism specific damping calculations in SW a-Si need to be performed and compared with simulated estimates of $\tan\phi$ to find out the dominant damping mechanism.

Table 6.4: Damping in the a-Si nanofilm as a function of frequency at 300 K for the longitudinal-mode oscillation.

Frequency (GHz)	$\tan\phi$	Ref [188]	
		With internal strain	Without internal strain
2	9.48×10^{-3}	9.73×10^{-4}	6.08×10^{-5}
3	8.86×10^{-3}	1.46×10^{-3}	8.11×10^{-5}
4	6.25×10^{-3}	1.82×10^{-3}	1.22×10^{-4}
5	7.21×10^{-3}	2.48×10^{-3}	1.52×10^{-4}
8	5.77×10^{-3}	4.01×10^{-3}	2.21×10^{-4}
10	8.46×10^{-3}	5.06×10^{-3}	3.16×10^{-4}
12	8.81×10^{-3}	5.37×10^{-3}	3.04×10^{-4}
15	7.41×10^{-3}	6.49×10^{-3}	4.22×10^{-4}
25	8.67×10^{-3}	1.02×10^{-2}	5.45×10^{-4}
30	8.99×10^{-3}	1.05×10^{-2}	6.41×10^{-4}
40	1.10×10^{-2}	1.14×10^{-2}	7.24×10^{-4}
50	1.19×10^{-2}	1.27×10^{-2}	8.52×10^{-4}

6.4 Summary

This chapter presented the first MD simulations of damping in amorphous silicon for longitudinal oscillations as a function of frequency and temperature using the SW potential. The amorphous

phase was obtained by melting a single-crystal Si structure followed by rapid quenching. Detailed analysis using RDF and bond order parameters revealed the destruction of the long range order of the crystalline phase in the amorphous structure. The damping in the nanofilm was found to be orders of magnitude larger than the c-Si nanofilm at 300 K for frequencies in the range 2 GHz to 50 GHz. Peaks in damping in the a-Si nanofilm were observed at 40 K and 150 K for oscillations at 10 GHz.

Chapter 7

Nonlinear oscillations in silicon nanoresonators

In this chapter, we present molecular dynamic simulations of nonlinear oscillations in two doubly-clamped nanobeams a undergoing flexural oscillations, and a clamped-free nanofilm undergoing longitudinal oscillations. The nanostructures were made of single-crystal Si atoms, and the atomic interactions were described using the SW potential.

In Section 7.1 we describe the simulation methodology which include details about the structural dimensions, boundary conditions, the thermal relaxation steps and the protocol used for obtaining the steady-state harmonic response. Results from simulations are presented in Section 7.2. Attempts have been made to make comparisons between simulated estimates of different dynamical quantities, e.g. resonance frequencies, and Q-factor with existing models of linear and nonlinear oscillations.

7.1 Simulation methodology

The following steps were implemented for simulating the steady-state harmonic responses of the single-crystal Si nanoresonators as a function of frequency and force. The first step was to create nanoresonators in LAMMPS environment with fundamental natural frequencies in the GHz range. These structures were then equilibrated at 300 K isothermally using the NH thermostat. Thermally relaxed structures were excited by applying sinusoidal harmonic forces with frequencies in the vicinity of their natural frequencies.

7.1.1 Structural details

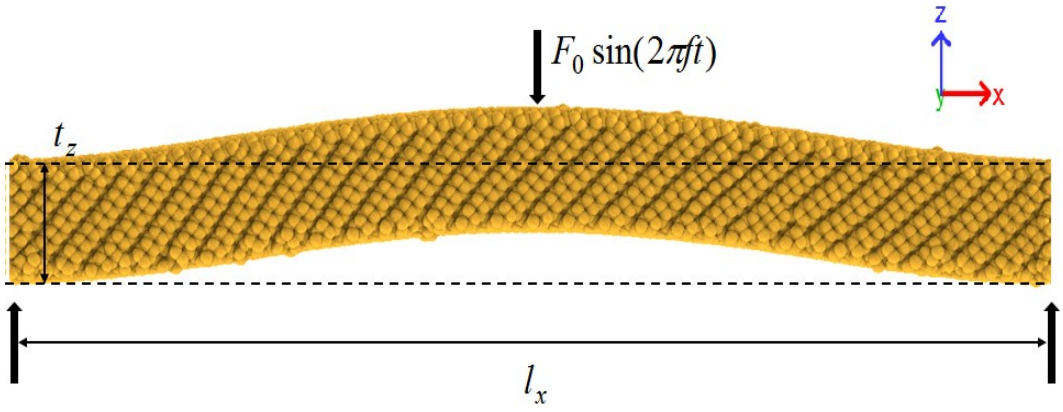

Figure 7-1: Schematic representation of the Sample 1. The thickness of the structure is t_z. The structure is clamped at the two ends (shown by black arrow), i.e. $x = 0$ and $x = l_x$. The dotted lines show the initial configuration of the atoms. The harmonic force $F_0 \sin(2\pi ft)$ is applied on the atoms in the center of the structure in the z-direction to obtain bending vibrations.

Single-crystal Si structures were constructed by placing atoms in the body centered tetragonal lattice positions with a lattice parameter of 5.43 Å. The interactions between Si atoms were modeled using the SW potential. A Cartesian coordinate system was attached to the structures with the x, y, and z axes oriented along the [1 0 0], [0 1 0], and [0 0 1] directions respectively. The dimensions, clamping conditions, modes of oscillations, and the aspect ratios of the different structures studied are presented in Table 7.1. Doubly-clamped condition was achieved by fixing atomic layers at the two ends ($x = 0$ and $x = l_x$) of the structure in the axial direction. A schematic illustration of the Sample 1 (doubly-clamped beam) is shown in Figure 7-1. The clamping condition for Sample 3 (clamped-free nanofilm) was the same as that for the silicon nanofilm mentioned in Chapter 5. Free-surface boundary condition was applied in the lateral directions of

the doubly-clamped structures, and the nanofilm had free-surface boundary condition for the atoms in the end atomic layer ($x = l_x$).

7.1.2 Thermal equilibration

The method used for the thermal equilibration of the structures at 300 K was similar to the method presented in Section 5.1.2. The NH thermostat was used for the entire equilibration process and the value of τ_{NH} was chosen to be 0.01 ps. Initially the structures were heated to 300 K, the doubly-clamped structures reached 300 K in 6 ns and the nanofilm in 4 ns. At 300 K the structures were equilibrated for 40 ns to prepare them for further simulations. Surface reconstruction was observed in all the samples.

Table 7.1: Boundary conditions and geometric properties of the nanoresonators

	Boundary condition	Mode	Geometry	Length, l_x (nm)	Width, w_y (nm)	Thickness, t_z (nm)	Aspect ratio, $\frac{l_x}{w_y}$
Sample 1	Doubly-clamped	Flexural	Beam	30	6	3	5
Sample 2	Doubly-clamped	Flexural	Beam	29.6	3.5	3.5	8.5
Sample 3	Clamped-free	Longitudinal	Film	7.6	4.34	4.34	2

7.1.3 Methodology for obtaining steady-state harmonic response

The steady-state harmonic responses of the structures were obtained using the following steps.

a) The displacement noise was captured in the axial and the out-of-plane directions for all the samples. The resonance frequencies for the first bending modes of Sample 1 and Sample 2 and the first longitudinal mode of Sample 3 were obtained by analyzing the FFT of the displacement noise.

b) Doubly-clamped structures were set to flexural oscillations in the out of plane direction by applying sinusoidal harmonic forces ($F_0 \sin(2\pi ft)$) on the atoms in the central atomic layer, i.e., at $x = \frac{l_x}{2}$ (see Figure 7-1). The nanofilm was put to oscillations in the axial direction by applying forces on atoms in the end layer, i.e., at $x = l_x$. The motions of the atoms under the application of the harmonic forces were recorded for calculating the amplitude of oscillation.

c) Amplitude of oscillation was calculated from the steady-state response using Eq. (4.4). The initial transient was selected manually from the time trace of the displacement. The duration of the transient oscillations varied from sample to sample, depending on the frequency of operation, magnitude of the force and the mode of oscillation.

7.2 Results

In this section, we report dynamical quantities of the single-crystal Si nanoresonators estimated from the simulations of steady-state harmonic response, and thermal noise. The resonance frequencies of mechanical modes were calculated using the finite element simulations and the FFT of the thermomechanical noise. The Q-factor for the fundamental modes were calculated from the thermal noise and the steady-state harmonic response.

7.2.1 Sample 1

The analysis of nonlinear oscillators involves the identification of linear resonance frequencies and normal modes. The nonlinear response is then interpreted in terms of linear resonance frequency and mode shapes. Therefore modal analysis is central to the understanding of nonlinear oscillations.

7.2.1.1 Modal analysis

The resonance frequencies for the bending modes of a doubly-clamped Euler-Bernoulli beam with rectangular cross-section is given by [46]

$$f_n = \frac{k_n^2}{2\pi l_x^2} t_z \sqrt{\frac{E}{12\rho}}, k_n = \{4.73,..\}. \quad (7.1)$$

Using the properties of SW Si and Eq. (7.1) the resonance frequencies for the first and the second bending modes for Sample 1 were calculated as 21.05 GHz and 57.9 GHz.

Table 7.2: Comparison of the resonance frequencies of the first 4 modes of Sample 1 obtained using COMSOL and MD simulations

Mechanical mode	Resonance frequency using COMSOL (GHz)	Resonance frequency from thermal noise (GHz)
Principal in-plane flexural mode	20.4	20.86
Principal out-of-plane flexural mode	34.5	35.5
Principal torsional mode	49	51
In-plane second bending mode	58	59

Figure 7-2, shows the modeshapes of the first 4 modes of Sample 1 calculated using the finite element software COMSOL. These modes are the fundamental bending mode, first in-plane bending mode, first torsional mode, and the second bending mode. Next, the predictions of the resonance frequencies obtained using the finite element analysis is compared with the estimates of molecular dynamic simulations. In order to do that, the displacement noise in the x, y and z directions at 300 K were captured by tracking the motion of the atomic layer at $x = \frac{l_x}{2}$ for a total duration of 300 ns. The mode dependent resonance frequencies of Sample 1 were calculated from the FFT of the displacement noise. A comparison of the resonance frequencies of the first 4 modes of Sample 1 calculated using the FFT of thermal noise and the finite element simulations is presented in Table 7.2.

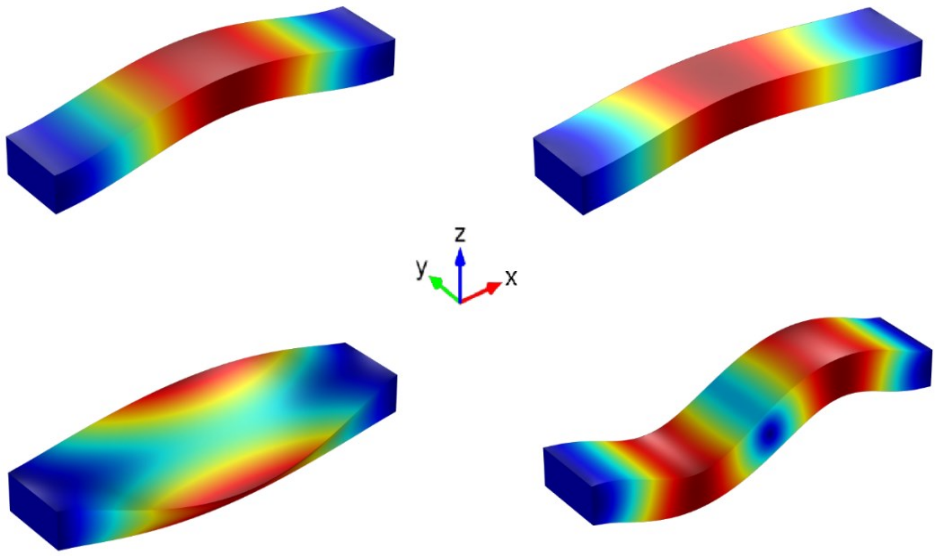

Figure 7-2: Modal analysis of the Sample 1. The images were obtained using the finite element method simulation software, COMSOL. The calculated resonant frequencies of the different modes are: (a) principal in-plane flexural mode, 20.4 GHz; (b) principal out-of-plane flexural mode, 34.5 GHz; (c) principal torsional mode, 49 GHz and (d) in-plane second bending mode, 58 GHz. These images are indicative of the dynamic behavior of the different modes and should not be used to compare relative modal displacement.

7.2.1.2 Q-factor from thermal noise

The Q-factor for the first bending mode of Sample 1 was calculated from the time trace of thermal noise using the method described in Section 4.2.2.3. The thermal noise for the atomic layer at $x = \frac{l_x}{2}$ in the z-direction was captured for a total duration of 400 ns. The PSD of the displacement noise was calculated after dividing the noise data into equal segments of duration 100 ns each. The estimates of the Q-factor for the fundamental bending mode obtained for each of these segments were 313, 1234, 1026, and 1498. These numbers gave the estimates of Q_0 and σ_Q as 1018 and 508. The latter is in reasonable agreement with Eq. (2.24) which predicts a standard deviation of 491.

7.2.1.3 Steady-state harmonic response

Steady-state harmonic response around the fundamental bending mode frequency for Sample 1 is plotted in Figure 7-3. For small forces, F_0 = 0.002 nN, the harmonic response resembled linear Lorentzian behavior with the peak in amplitude at 20.9 GHz. As the magnitude of the force was increased, the response increasingly deviated from the linear behavior and the peak amplitude frequencies shifted further away from the damped natural frequency of 20.9 GHz, showing signature of spring hardening. The curve for F_0 = 0.01 nN showed infinite slope at 21.01 GHz. The backbone curve was fit to Eq. (2.29) to obtain f_0 = 20.9 GHz, Q = 835. Figure 7-4, shows the amplitude frequency curve obtained from MD simulations with simulated amplitude-frequency curves obtained using Eq. (2.26) superimposed.

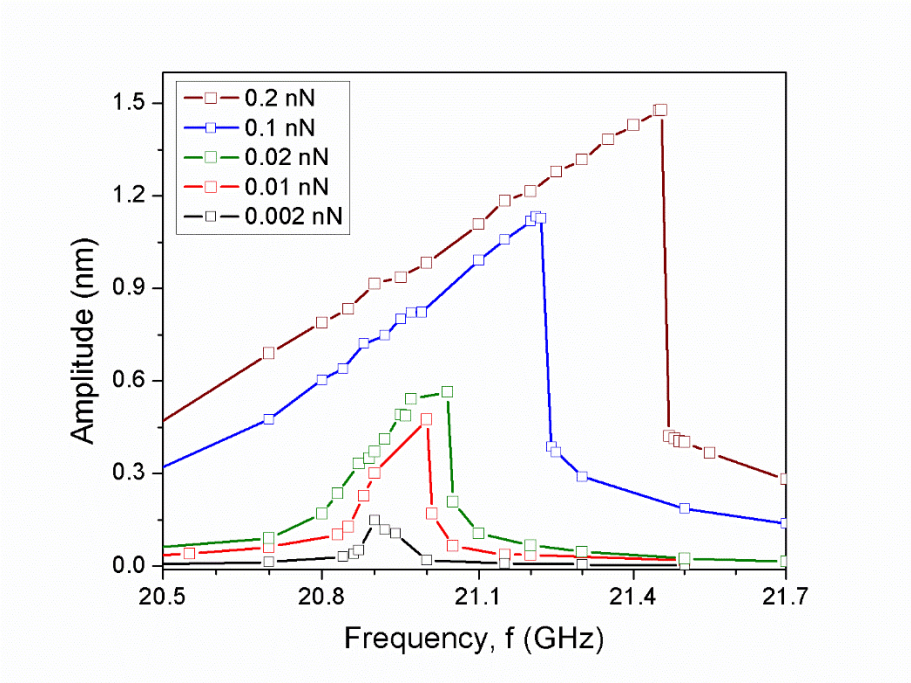

Figure 7-3: Steady-state harmonic response of Sample 1 in the vicinity of the fundamental bending resonance frequency as functions of frequency and harmonic force.

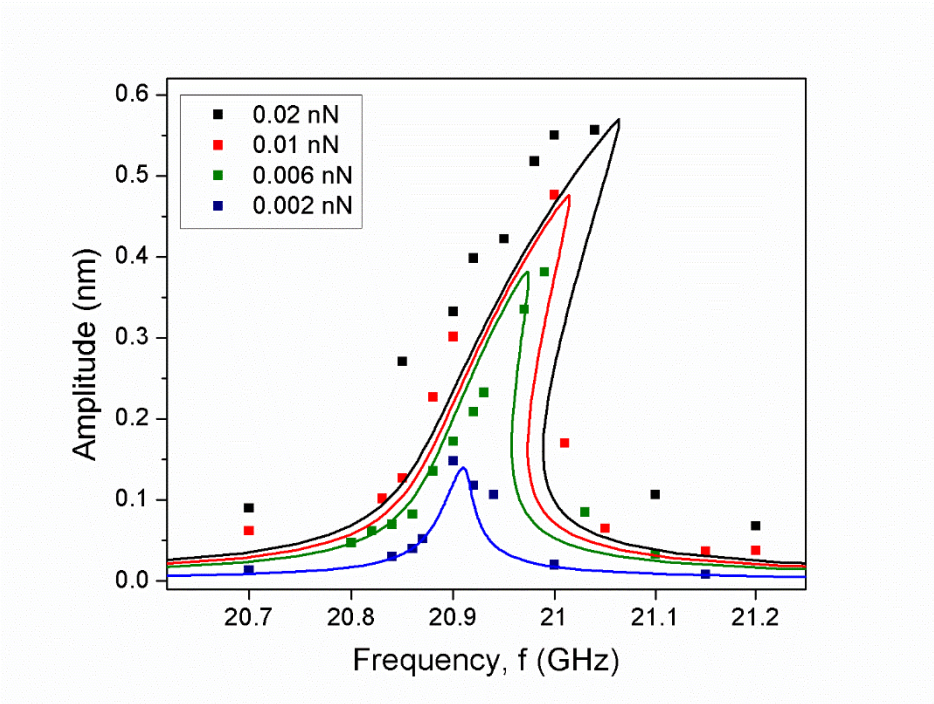

Figure 7-4: Comparison of the nonlinear response in Sample 1 obtained from MD simulations and the Duffing equation. The symbols represent data from MD simulations and the curves are calculated using Eq. (2.26).

7.2.2 Sample 2

7.2.2.1 Modal analysis

The modal analysis using COMSOL and thermal noise revealed that the resonance frequencies of the first out-of-plane bending mode and the first in plane bending mode for Sample 2 to be 25.2 GHz. Figure 7-5 shows the simulated modeshapes of these two degenerate modes superimposed. The resonance frequencies for the out-of-plane and the in-plane resonance frequencies were found to be 25.19 GHz from the FFT of the thermal noise captured for 10 ns.

7.2.2.2 Steady-state harmonic response

Steady-state harmonic response across the fundamental bending mode natural frequency for Sample 2 is plotted in Figure 7-6. For very small magnitude of the harmonic force, $F_0 = 8\times10^{-4}$ nN, the harmonic response shows two resonant peaks at 25.15 GHz and 25.2 GHz. As the magnitude of the force was increased, the peak at 25.2 GHz increasingly shifted towards higher frequencies showing signatures of spring hardening. Jump like phenomenon did not take place for forces smaller than 0.1 nN. The resonance peak at 25.15 GHz, initially, did not change with increased force amplitudes, and stayed at 25.15 GHz till a force of 8×10^{-3} nN. However, for the force 3.2×10^{-3} nN this peak shifted to 25.2 GHz, and disappeared for the maximum force of 0.1 nN. This harmonic response is similar to 1:1 internal resonance of two-degree-of-freedom Duffing system with cubic coupled terms [191]. Similar coupling of orthogonal modes has been reported in doubly-clamped gold nanoresonators [192].

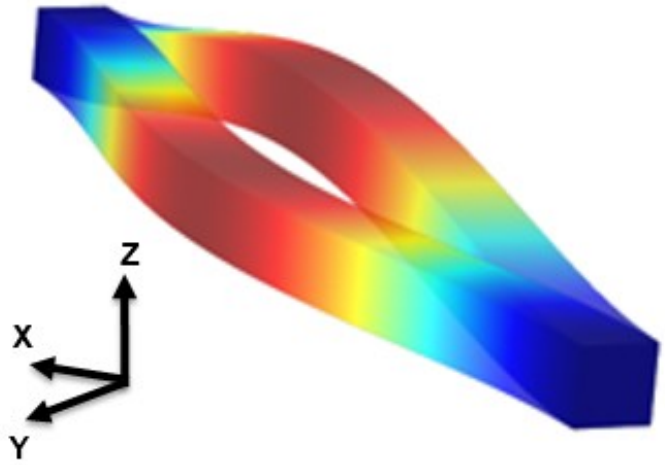

Figure 7-5: Mode shapes for the fundamental out-of-plane bending mode and in-plane bending mode of Sample 2.

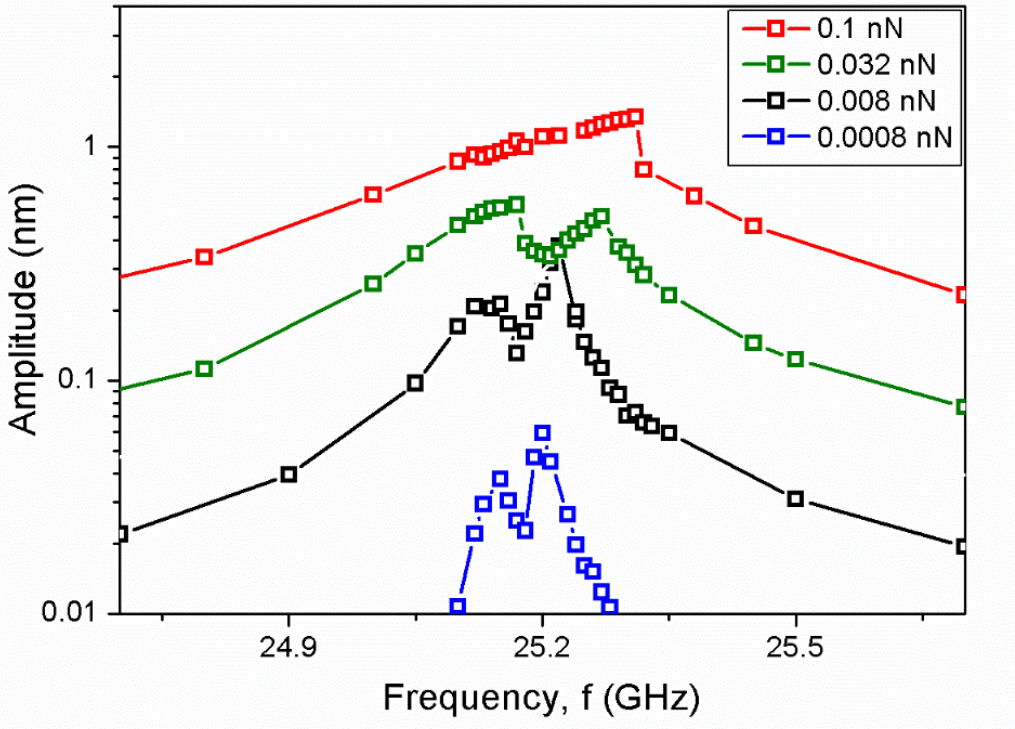

Figure 7-6: Steady-state harmonic response of Sample 2 in the vicinity of the fundamental bending mode resonance frequency as function of frequency and harmonic force.

7.2.3 Sample 3

The structural dimensions and clamping conditions of Sample 3 are identical to the silicon nanofilm reported in Chapter 5. In this section, we present results from the nonlinear oscillations of the nanonfilm for oscillations in the longitudinal mode. The steady-state harmonic response of the structure was simulated around the first longitudinal mode natural frequency of 256.5 GHz, and the response was fit to the Duffing model.

7.2.3.1 Q-factor from thermal noise

The axial displacement noise in the end layer of the nanofilm was captured for 285 ns and was divided into 3 equal segments 85 ns. The Lorentzian fit to the peak in the PSD of the noise corresponding to the fundamental longitudinal mode for each of these segments produced Q-factor estimates of 7034, 3956 and 5451, the mean of which was 5480 and the standard deviation was 1539. The latter is in good agreement with Eq. (2.24) which predicted a standard deviation of 2074.

7.2.3.2 Q-factor from harmonic response

Steady-state harmonic response across the first longitudinal resonance frequency for Sample 3 for a range of harmonic forces is plotted in Figure 7-7. For small magnitude of the harmonic force, F_0 = 0.001 nN, the harmonic response is similar to linear Lorentzian behavior. As the magnitude of the force was increased, the response increasingly deviated from the linear behavior. The peak amplitude frequencies shifted further away from the damped natural frequency of 256.5 GHz, showing signature of spring softening. The curve for F_0 = 0.004 nN showed infinite slope at

256.37 GHz. A fit to the backbone curve with Eq. (2.29) was performed to obtain $f_0 = 256.5$ GHz and $Q = 6384$, which was in good agreement with the thermomechanical noise analysis.

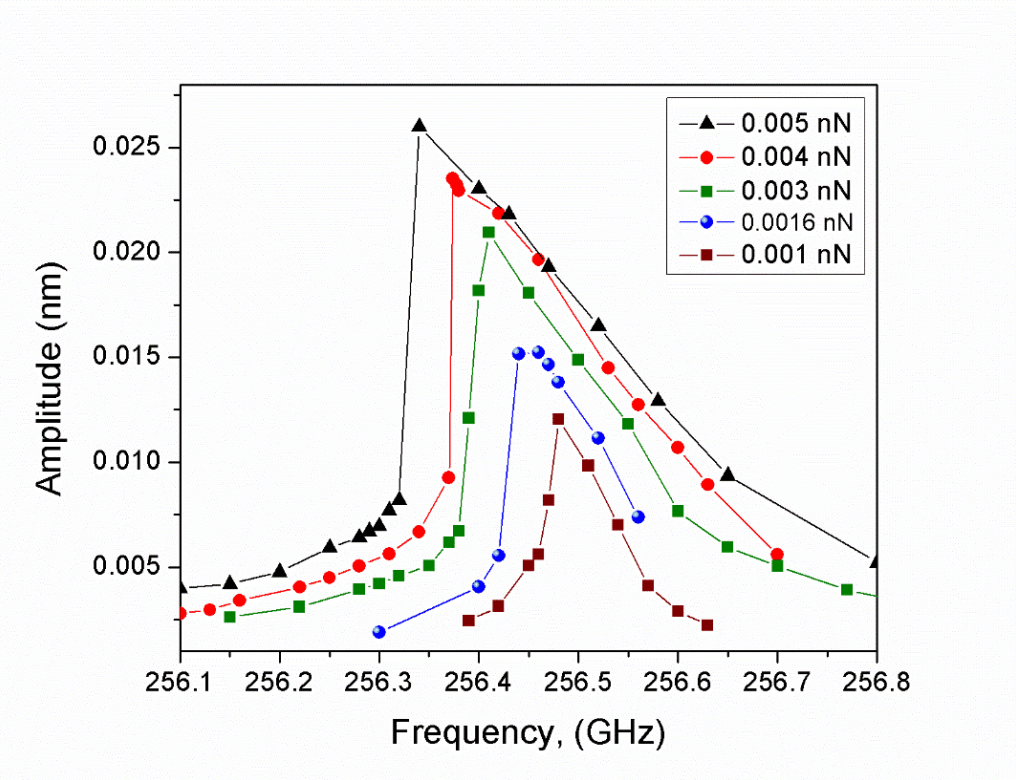

Figure 7-7: Nonlinear frequency responses for the silicon nanofilm. The data points were obtained from MD simulations and the curves were calculated using Eq. (2.29) with $A_c = 0.00927$ nm (corresponding force 0.004 nm), $f_0 = 256.5$ GHz and $Q = 6384$.

7.2.3.3 Modeshape

The simulated mode shape for the longitudinal mode at 255 GHz is shown in Figure 7-8, also superimposed in the same plot is the modeshape at 10 GHz. It is clearly observed that at 255 GHz, the structure deviates from linear behavior displaying signatures of nonlinear geometric effects. A possible source of this nonlinearity is the mode coupling between the longitudinal mode and a torsional mode at 182 GHz.

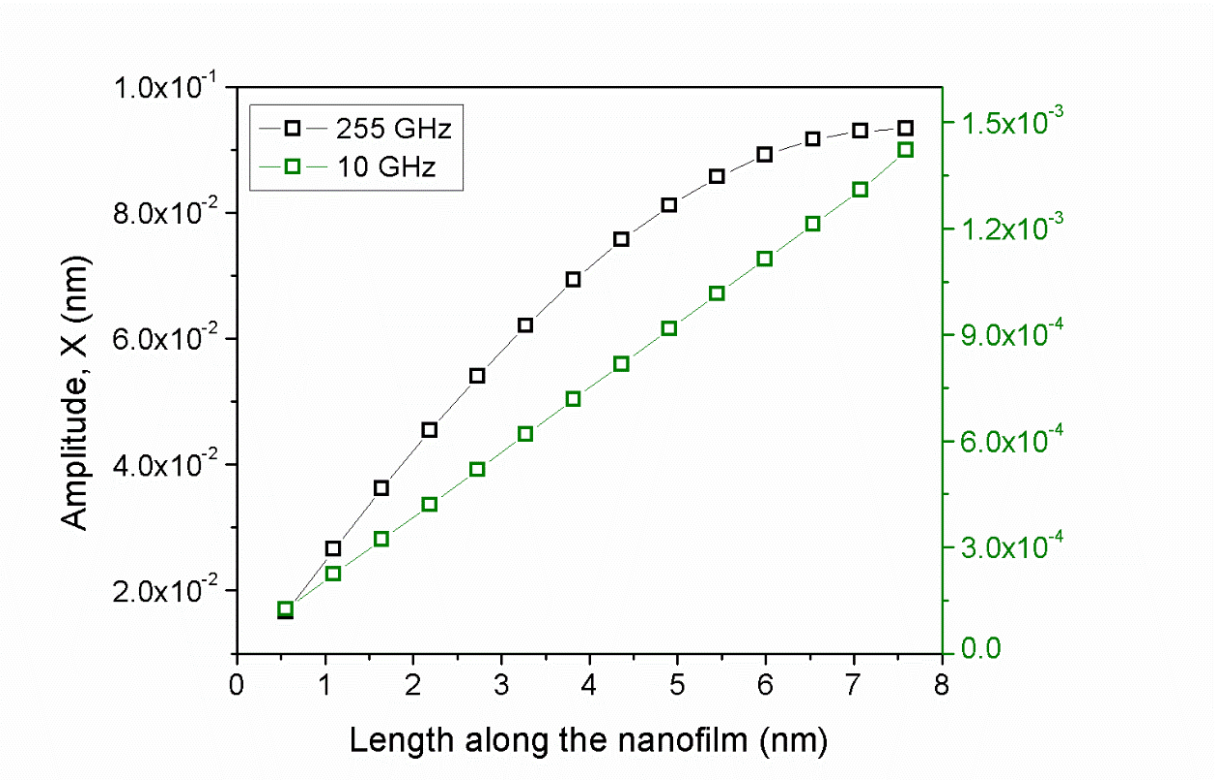

Figure 7-8: Comparison of the modeshape in the nanofilm calculated for oscillations at 10 GHz and 255 GHz.

7.3 Discussion

Steady-state harmonic oscillations of Sample 1 (doubly-clamped beam) showed spring hardening type nonlinearity, this observation is in agreement with the experimental investigations of nonlinear oscillations in doubly-clamped beams [48, 53]. Dissipative nonlinearities can be neglected because the quality factor is in good agreement with the value of 1018±507 obtained from the linear analysis of thermomechanical noise. Similarly, the Q=835 is of similar orders compared to the value of $\tan\phi$=3.81×10^{-4} ($\sim Q$=2600) at 20 GHz for the nanowire investigated in Chapter 5.

The flexural oscillation of a doubly-clamped beams is associated with the stretching of the mid plane. The increase in the length is associated with displacement-dependent nonhomogeneous tension in the structure (increased tension at the clamped ends compared to the center of the beam). This effect is small as long as the amplitude of oscillation is much smaller than the width of the beam. Accounting for the tension in the beam due to strain, we get the following equation of motion similar to the Duffing equation mentioned in Section 2.3 [193]

$$\ddot{z} + \frac{2\pi f_0}{Q}\dot{z} + 4\pi^2 f_0^2 z + \Lambda z^3 = \frac{F_0}{m}\sin(2\pi f t), \tag{7.2}$$

where z is the out-of-plane displacement and $\Lambda = \frac{E}{18\rho}\left(\frac{2\pi}{l}\right)^4$. The critical amplitude of a doubly-clamped beam is given by

$$A_c = \frac{2}{\sqrt[4]{3}}\sqrt{\frac{1}{Q}\left(\frac{w^2}{3} + \frac{T_0 l^2}{\pi^2 E w t}\right)}, \tag{7.3}$$

Ignoring the tension term in Eq. (7.3) and using Q=1018, A_c can be calculated as 0.08 nm which is in reasonable agreement with 0.17 nm obtained from MD simulations.

The presence of multiple peaks in the harmonic response of doubly-clamped strucutres due to internal resonance has been observed before [122]. Geometries with square cross-section such as wires, strings, and beams have commensurate resonance frequencies for the in-plane and out-of-plane fundamental modes. When one of these two modes is harmonically oscillated the other mode gets excited. Therefore, the observation of 1:1 internal resonance indicates modal coupling between these two modes.

Sample 3 showed nonlinear spring softening behavior in the harmonic response. An analysis of the mode shape close to the resonance frequency and away from the resonance frequency also showed signatures of nonlinearity. It is interesting to note that two geometries (Sample 1 and Sample 3) of the same material showed different nonlinear behavior depending on the mode of oscillation, and clamping condition.

The results reported in this chapter demonstrate the usefulness of MD simulations in studying nononlinear oscillations in nanoresonators. Steady-state harmonic response in nanoresonators can be reached easily because of very high frequency oscillations. Therefore, in spite of limitations of computational resources, multiple measurements of amplitude across the resonance frequencies can be performed easily. Moreover, in MD simulations the user can enforce boundary conditions at will and study idealized conditions which is otherwise difficult to achieve using experiments. Furthermore, tiny devices with dimensions on the order of few nanometers, and intricate architectures can be simulated with precise control, which are difficult to fabricate and investigate experimentally. The method used for studying nonlinear oscillations in single-crystal silicon nanoresonators can be applied to a wide range of nanoresonators of different materials, and modes.

7.4 Summary

In this chapter we have presented MD simulations of nonlinear oscillations for the fundamental flexural modes of two doubly-clamped nanobeams and fundamental longitudinal mode oscillations of a nanofilm, all made of single-crystal Si. A protocol has been developed for obtaining the steady-state harmonic oscillations in the structures in the vicinity of their resonance frequencies. The harmonic response of one of the doubly-clamped nanobeam (with rectangular cross-section) and the nanofilm had qualitative match with the Duffing model. The doubly-clamped nanobeam

with square cross-section displayed signatures of 1:1 internal resonance which had qualitative similarities with 1:1 internal resonance two-degree-of-freedom Duffing system.

Chapter 8

8.1 Statement of original contributions

The original contributions contained in this thesis are as follows.

1. Developed protocol for the estimation of damping in nanoresonators using isothermal MD simulations considering the linearity and convergence of damping to ensure accuracy.

2. Models of Akheizer damping mechanism have been shown to be in agreement with MD simulations of damping in single-crystal Si nanoresonators.

3. Performed first MD simulations of damping in amorphous nanoresonators.

4. It has been demonstrated that damping in a-Si is two orders of magnitude larger than c-Si for room temperatures oscillations in the GHz range. Temperature dependent damping peaks in a-Si have been observed.

5. Simulation methodology has been developed for studying nonlinear oscillations in nanoresonators.

8.2 Future work

This study can be extended in any of the following areas.

Damping in the Landau-Rumer regime

MD simulations of damping in the silicon nanofilm showed Akheiser damping as the dominant source of dissipation in silicon at room temperature. The same structure can be used to find out the frequency and temperature range in which Landau-Rumer damping becomes significant.

Damping from free surfaces in nanoresonators

MD simulations of damping in the single-crystal Si nanofilm and the nanowire showed that free surfaces contribute to the overall damping. One way to minimize this effect would be to passivate the dangling bonds at the surfaces which are formed during the surface reconstruction by atomic hydrogen. Experimental studies at low frequencies have indicated that hydrogen contamination in very small volume fraction reduces dissipation in amorphous silicon by eliminating the dangling bonds. Molecular dynamics simulations can be used to confirm this behavior and gain insight into the mechanisms that causes this drop in damping.

Mechanisms of damping by crystallographic defects

Materials used for nanoresonators often have crystallographic defects such as vacancies, impurity atoms, and grain boundaries. Although we understand how these defects affect damping at low frequencies, there is a growing need to understand and develop models for damping caused by crystallographic defects at very high frequencies. The damping results for the silicon nanofilm can be

used as benchmark to understand the effect of defects such as interstitials, vacancies, dislocations, twins, grain boundaries (by creating bamboo-like structure) on damping in silicon and other materials.

References

[1] M. Matheny, L. Villanueva, R. Karabalin, J. E. Sader, and M. Roukes, "Nonlinear mode-coupling in nanomechanical systems," *Nano Letters,* vol. 13, pp. 1622-1626, 2013.

[2] Z. Qian, Y. Hui, F. Liu, S. Kar, and M. Rinaldi, "245 MHz graphene-aluminum nitride nano plate resonator," in *Solid-State Sensors, Actuators and Microsystems (TRANSDUCERS & EUROSENSORS XXVII), Transducers & Eurosensors XXVII: The 17th International Conference on*, pp. 2005-2008, 2013.

[3] M. Zalalutdinov, K. L. Aubin, R. B. Reichenbach, A. T. Zehnder, B. Houston, J. M. Parpia, and H. G. Craighead, "Shell-type micromechanical actuator and resonator," *Applied Physics Letters,* vol. 83, pp. 3815-3817, 2003.

[4] X. L. Feng, R. He, P. Yang, and M. L. Roukes, "Very High Frequency Silicon Nanowire Electromechanical Resonators," *Nano Letters,* vol. 7, pp. 1953-1959, 2007.

[5] L. Ding, C. Baker, P. Senellart, A. Lemaitre, S. Ducci, G. Leo, and I. Favero, "High Frequency GaAs Nano-Optomechanical Disk Resonator," *Physical Review Letters,* vol. 105, pp. 263903-1-263903-4, 2010.

[6] M. Li, H. X. Tang, and M. L. Roukes, "Ultra-sensitive NEMS-based cantilevers for sensing, scanned probe and very high-frequency applications," *Nature Nanotechnology,* vol. 2, pp. 114-120, 2007.

[7] V. Kaajakari, T. Mattila, A. Lipsanen, and A. Oja, "Nonlinear mechanical effects in silicon longitudinal mode beam resonators," *Sensors and Actuators A: Physical,* vol. 120, pp. 64-70, 2005.

[8] S. Etaki, F. Konschelle, Y. M. Blanter, H. Yamaguchi, and H. Van Der Zant, "Self-sustained oscillations of a torsional SQUID resonator induced by Lorentz-force back-action," *Nature Communications,* vol. 4, pp. 1803-1-1803-5, 2013.

[9] S. Ghaffari, S. A. Chandorkar, S. Wang, E. J. Ng, C. H. Ahn, V. Hong, *Y.* Yang, and T. W. Kenny, "Quantum limit of quality factor in silicon micro and nano mechanical resonators," *Scientific Reports,* vol. 3, 2013.

[10] M. Rinaldi, C. Zuniga, and G. Piazza, "5-10 GHz AlN contour-mode nanoelectromechanical resonators," in *Micro Electro Mechanical Systems. MEMS. IEEE 22nd International Conference on*, pp. 916-919, 2009.

[11] G. Anetsberger, R. Rivière, A. Schliesser, O. Arcizet, and T. J. Kippenberg, "Ultralow-dissipation optomechanical resonators on a chip," *Nature Photonics,* vol. 2, pp. 627-633, 2008.

[12] V. Sazonova, Y. Yaish, H. Üstünel, D. Roundy, T. A. Arias, and P. L. McEuen, "A tunable carbon nanotube electromechanical oscillator," *Nature,* vol. 431, pp. 284-287, 2004.

[13] A. W. Barnard, V. Sazonova, A. M. van der Zande, and P. L. McEuen, "Fluctuation broadening in carbon nanotube resonators," *Proceedings of the National Academy of Sciences,* vol. 109, pp. 19093-19096, 2012.

[14] J. S. Bunch, A. M. Van Der Zande, S. S. Verbridge, I. W. Frank, D. M. Tanenbaum, J. M. Parpia, H. G. Craighead, and P. L. McEuen, "Electromechanical resonators from graphene sheets," *Science,* vol. 315, pp. 490-493, 2007.

[15] D. Garcia-Sanchez, A. M. van der Zande, A. S. Paulo, B. Lassagne, P. L. McEuen, and A. Bachtold, "Imaging mechanical vibrations in suspended graphene sheets," *Nano Letters,* vol. 8, pp. 1399-1403, 2008.

[16] M. Sansa, E. Sage, E. C. Bullard, M. Gely, T. Alava, E. Colinet, A. K. Naik, L. G. Villanueva, L. Duraffourg, M. L. Roukes, G. Jourdan, and S. Hentz, "Frequency fluctuations in silicon nanoresonators," *arXiv preprint arXiv:1506.08135,* 2015.

[17] Y. T. Yang, C. Callegari, X. L. Feng, K. L. Ekinci, and M. L. Roukes, "Zeptogram-Scale Nanomechanical Mass Sensing," *Nano Letters,* vol. 6, pp. 583-586, 2006.

[18] L. Villanueva, R. Karabalin, M. Matheny, D. Chi, J. Sader, and M. Roukes, "Nonlinearity in nanomechanical cantilevers," *Physical Review B,* vol. 87, pp. 024304-1-024304-8, 2013.

[19] X. M. H. Huang, C. A. Zorman, M. Mehregany, and M. L. Roukes, "Nanoelectromechanical systems: Nanodevice motion at microwave frequencies," *Nature,* vol. 421, pp. 496-496, 2003.

[20] B. Ilic, H. Craighead, S. Krylov, W. Senaratne, C. Ober, and P. Neuzil, "Attogram detection using nanoelectromechanical oscillators," *Journal of Applied Physics,* vol. 95, pp. 3694-3703, 2004.

[21] J. Chaste, A. Eichler, J. Moser, G. Ceballos, R. Rurali, and A. Bachtold, "A nanomechanical mass sensor with yoctogram resolution," *Nature Nanotechnology,* vol. 7, pp. 301-304, 2012.

[22] M. S. Hanay, S. Kelber, A. K. Naik, D. Chi, S. Hentz, E. C. Bullard, E. Colinet, L. Duraffourg, and M. L. Roukes, "Single-protein nanomechanical mass spectrometry in real time," *Nature Nanotechnology,* vol. 7, pp. 602-608, 2012.

[23] M. S. Hanay, S. I. Kelber, C. D. O'Connell, P. Mulvaney, J. E. Sade*r, and M. L. Roukes, "Inertial imaging with nanomechanical systems," Nature Nanotechnology,* Vol. 10, pp. 339-344, *2*015.

[24] H. J. Mamin and D. Rugar, "Sub-attonewton force detection at millikelvin temperatures," *Applied Physics Letters,* vol. 79, pp. 3358-3360, 2001.

[25] R. Budakian, H. Mamin, and D. Rugar, "Spin manipulation using fast cantilever phase reversals," *Applied Physics Letters,* vol. 89, pp. 113113-1-113113-3, 2006.

[26] R. He, X. Feng, M. Roukes, and P. Yang, "Self-transducing silicon nanowire electromechanical systems at room temperature," *Nano Letters,* vol. 8, pp. 1756-1761, 2008.

[27] A. Naik, M. Hanay, W. Hiebert, X. Feng, and M. Roukes, "Towards single-molecule nanomechanical mass spectrometry," *Nature Nanotechnology,* vol. 4, pp. 445-450, 2009.

[28] M. Zheng, K. Eom, and C. Ke, "Calculations of the resonant response of carbon nanotubes to binding of DNA," *Journal of Physics D: Applied Physics,* vol. 42, pp. 145408-1-145408-8, 2009.

[29] T. Kwon, J. Park, J. Yang, D. S. Yoon, S. Na, C.-W. Kim, J.-S. Suh, Y.-M. Huh, S. Haam, and K. Eom, "Nanomechanical in situ monitoring of proteolysis of peptide by cathepsin B," *PLoS One,* vol. 4, pp. e6248-1-e6248-8, 2009.

[30] D. Rugar, R. Budakian, H. Mamin, and B. Chui, "Single spin detection by magnetic resonance force microscopy," *Nature,* vol. 430, pp. 329-332, 2004.

[31] A. D. O'Connell, M. Hofheinz, M. Ansmann, R. C. Bialczak, M. Lenander, E. Lucero, M. Neeley, D. Sank, H. Wang, M. Weides J. Wenner, J. M. Martinis, and A. N. Cleland, "Quantum ground state and single-phonon control of a mechanical resonator," *Nature,* vol. 464, pp. 697-703, 2010.

[32] J. Chan, T. M. Alegre, A. H. Safavi-Naeini, J. T. Hill, A. Krause, S. Gröblacher, M. Aspelmeyer, and O. Painter, "Laser cooling of a nanomechanical oscillator into its quantum ground state," *Nature,* vol. 478, pp. 89-92, 2011.

[33] M. Dragoman, A. Takacs, A. Muller, H. Hartnagel, R. Plana, K. Grenier, and D. Dubuc, "Nanoelectromechanical switches based on carbon nanotubes for microwave and millimeter waves," *Applied Physics Letters,* vol. 90, pp. 113102-1-113102-3, 2007.

[34] P. Sharma, J. Perruisseau-Carrier, C. Moldovan, and A. M. Ionescu, "Electromagnetic performance of RF NEMS graphene capacitive switches," *Nanotechnology, IEEE Transactions on,* vol. 13, pp. 70-79, 2014.

[35] C. Chen, S. Lee, V. V. Deshpande, G.-H. Lee, M. Lekas, K. Shepard, and J. Hone, "Graphene mechanical oscillators with tunable frequency," *Nature Nanotechnology,* vol. 8, pp. 923-927, 2013.

[36] Y. Xu, C. Chen, V. V. Deshpande, F. A. DiRenno, A. Gondarenko, D. B. Heinz, S. Liu, P. Kim, and J. Hone, "Radio frequency electrical transduction of graphene mechanical resonators," *Applied Physics Letters,* vol. 97, pp. 243111-1-243111-3, 2010.

[37] A. S. Nowick and B. S. Berry, *Anelastic relaxation in crystalline solids*: Academic Press, 1972.

[38] K. Ekinci, Y. Yang, and M. Roukes, "Ultimate limits to inertial mass sensing based upon nanoelectromechanical systems," *Journal of Applied Physics,* vol. 95, pp. 2682-2689, 2004.

[39] S. Joshi, S. Hung, and S. Vengallatore, "Design strategies for controlling damping in micromechanical and nanomechanical resonators," *EPJ Techniques and Instrumentation,* vol. 1, pp. 1-14, 2014.

[40] S. Reid, G. Cagnoli, D. Crooks, J. Hough, P. Murray, S. Rowan, M. M. Fejer, R. Route, and S. Zappe, "Mechanical dissipation in silicon flexures," *Physics Letters A,* vol. 351, pp. 205-211, 2006.

[41] G. Sosale, S. Prabhakar, L. G. Fréchette, and S. Vengallatore, "A microcantilever platform for measuring internal friction in thin films using thermoelastic damping for calibration," *Journl of Microelectromechanical Systems,* vol. 20, pp. 764-773, 2011.

[42] G. Sosale, K. Das, L. Fréchette, and S. Vengallatore, "Controlling damping and quality factors of silicon microcantilevers by selective metallization," *Journal of Micromechanics and Microengineering,* vol. 21, pp. 105010-1-105010-7, 2011.

[43] A. L. Kimball and D. E. Lovell, "Internal Friction in Solids," *Physical Review,* vol. 30, pp. 948-959, 1927.

[44] C. M. Zener and S. Siegel, "Elasticity and Anelasticity of Metals," *The Journal of Physical Chemistry,* vol. 53, pp. 1468-1468, 1949.

[45] C. Zener, "Anelasticity of metals," *Il Nuovo Cimento (1955-1965),* vol. 7, pp. 544-568, 1958.

[46] W. Thomson, *Theory of vibration with applications*: CRC Press, 1996.

[47] J. J. Stoker, *Nonlinear vibrations in mechanical and electrical systems*: Interscience Publishers, 1950.

[48] I. Kozinsky, H. C. Postma, I. Bargatin, and M . Roukes, "Tuning nonlinearity, dynamic range, and frequency of nanomechanical resonators," *Applied Physics Letters,* vol. 88, pp. 253101-1-253101-3, 2006.

[49] Z. Wang and P. X.-L. Feng, "Dynamic range of atomically thin vibrating nanomechanical resonators," *Applied Physics Letters,* vol. 104, pp. 103109-1-103109-5, 2014.

[50] A. H. Nayfeh and D. T. Mook, *Nonlinear oscillations*: John Wiley & Sons, 2008.

[51] C. Samanta, P. Gangavarapu, and A. Naik, "Nonlinear Mode Coupling and Internal Resonances in MoS2 Nanoelectromechanical System," *arXiv preprint arXiv:1505.07329,* 2015.

[52] T. Dunn, J.-S. Wenzler, and P. Mohanty, "Anharmonic modal coupling in a bulk micromechanical resonator," *Applied Physics Letters,* vol. 97, pp. 123109-1-123109-3, 2010.

[53] K. J. Lulla, R. B. Cousins, A. Venkatesan, M. J. Patton, A. D. Armour, C. J. Mellor, and J. R. Owers-Bradley, "Nonlinear modal coupling in a high-stress doubly-clamped nanomechanical resonator," *New Journal of Physics,* vol. 14, pp. 113040-1-113040-14, 2012.

[54] A. H. Nayfeh and P. F. Pai, *Linear and nonlinear structural mechanics*: John Wiley & Sons, 2008.

[55] A. Eichler, J. Moser, J. Chaste, M. Zdrojek, I. Wilson-Rae, and A. Bachtold, "Nonlinear damping in mechanical resonators made from carbon nanotubes and graphene," *Nature Nanotechnology,* vol. 6, pp. 339-342, 2011.

[56] M. Imboden, O. Williams, and P. Mohanty, "Nonlinear dissipation in diamond nanoelectromechanical resonators," *Applied Physics Letters,* vol. 102, pp. 103502-1-103502-4, 2013.

[57] L. G. Villanueva, R. B. Karabalin, M. H. Matheny, E. Kenig, M. C. Cross, and M. L. Roukes, "A nanoscale parametric feedback oscillator," *Nano Letters,* vol. 11, pp. 5054-5059, 2011.

[58] J. Gieseler, L. Novotny, and R. Quidant, "Thermal nonlinearities in a nanomechanical oscillator," *Nature Physics,* vol. 9, pp. 806-810, 2013.

[59] M. J. Buehler and H. Gao, "Ultra-large scale simulations of dynamic materials failure," *Handbook of Computational and Theoretical Nanotechnology,* pp. 427-467, 2005.

[60] D. Vlachakis, E. Bencurova, N. Papangelopoulos, and S. Kossida, "Current state-of-the-art molecular dynamics methods and applications," *Advances in Protein Chemistry and Structural Biology,* vol. 94, pp. 269-313, 2014.

[61] L. Sklar, *Physics and chance: Philosophical issues in the foundations of statistical mechanics*: Cambridge University Press, 1995.

[62] K. Kunal and N. R. Aluru, "Akhiezer damping in nanostructures," *Physical Review B,* vol. 84, pp. 245450-1-245450-8, 2011.

[63] H. Jiang, M.-F. Yu, B. Liu, and Y. Huang, "Intrinsic energy loss mechanisms in a cantilevered carbon nanotube beam oscillator," *Physical Review Letters,* vol. 93, pp. 185501-1-185501-4, 2004.

[64] S. Y. Kim and H. S. Park, "On the utility of vacancies and tensile strain-induced quality factor enhancement for mass sensing using graphene monolayers," *Nanotechnology,* vol. 21, pp. 105710-1-105710-8, 2010.

[65] A. F. Ávila, A. C. Eduardo, and A. S. Neto, "Vibrational analysis of graphene based nanostructures," *Computers & Structures,* vol. 89, pp. 878-892, 2011.

[66] J.-W. Jiang and J.-S. Wang, "Why edge effects are important on the intrinsic loss mechanisms of graphene nanoresonators," *Journal of Applied Physics,* vol. 111, pp. 054314-1-054314-9, 2012.

[67] J.-W. Jiang and J.-S. Wang, "Graphene-based torsional resonator from molecular-dynamics simulation," *EPL (Europhysics Letters),* vol. 96, pp. 66007-1-66007-6, 2011.

[68] J.-W. Jiang, H. S. Park, and T. Rabczuk, "Enhancing the mass sensitivity of graphene nanoresonators via nonlinear oscillations: the effective strain mechanism," *Nanotechnology,* vol. 23, pp. 475501-1-475501-7, 2012.

[69] S. Y. Kim and H. S. Park, "Multilayer friction and attachment effects on energy dissipation in graphene nanoresonators," *Applied Physics Letters,* vol. 94, pp. 101918-1-101918-3, 2009.

[70] S. Y. Kim and H. S. Park, "The importance of edge effects on the intrinsic loss mechanisms of graphene nanoresonators," *Nano Letters,* vol. 9, pp. 969-974, 2009.

[71] S. Y. Kim and H. S. Park, "Utilizing mechanical strain to mitigate the intrinsic loss mechanisms in oscillating metal nanowires," *Physical Review Letters,* vol. 101, pp. 215502-1-215502-4, 2008.

[72] Z. Qi and H. S. Park, "Intrinsic energy dissipation in CVD-grown graphene nanoresonators," *Nanoscale,* vol. 4, pp. 3460-3465, 2012.

[73] K. Kunal and N. R. Aluru, "Phonon mediated loss in a graphene nanoribbon," *Journal of Applied Physics,* vol. 114, pp. 084302-1-084302-8, 2013.

[74] K. Kunal and N. R. Aluru, "Intrinsic loss due to unstable modes in graphene," *Nanotechnology,* vol. 24, pp. 275701-1-275701-10, 2013.

[75] A. K. Vallabhaneni, J. F. Rhoads, J. Y. Murthy, and X. Ruan, "Observation of nonclassical scaling laws in the quality factors of cantilevered carbon nanotube resonators," *Journal of Applied Physics,* vol. 110, pp. 034312-1-034312-7, 2011.

[76] A. K. Vallabhaneni, X. Ruan, J. F. Rhoads, and J. Murthy, "A band-pass filter approach within molecular dynamics for the prediction of intrinsic quality factors of nanoresonators," *Journal of Applied Physics,* vol. 112, pp. 074301-1-074301-6, 2012.

[77] R. Raghunathan, P. A. Greaney, and J. C. Grossman, "Phonostat: Thermostatting phonons in molecular dynamics simulations," *The Journal of Chemical Physics,* vol. 134, pp. 214117-1-214117-9, 2011.

[78] S. Akita, S. Sawaya, and Y. Nakayama, "Energy loss of carbon nanotube cantilevers for mechanical vibration," *Japanese Journal of Applied Physics,* vol. 46, pp. 6295-6298, 2007.

[79] W. Guo, Y. Guo, H. Gao, Q. Zheng, and W. Zhong, "Energy dissipation in gigahertz oscillators from multiwalled carbon nanotubes," *Physical Review Letters,* vol. 91, pp. 125501-1-125501-4, 2003.

[80] Z. Zhou, V. K. Vasudevan, and D. Qian, "Energy Loss in Carbon Nanotube Beam Oscillators due to Anelastic Relaxation," *Journal of Engineering Materials and Technology,* vol. 134, pp. 031005-1-031005-8, 2012.

[81] D. Georgakaki, O. Ziogos, and H. Polatoglou, "Vibrational and mechanical properties of Si/Ge nanowires as resonators: A molecular dynamics study," *physica status solidi (a),* vol. 211, pp. 267-276, 2014.

[82] J.-W. Jiang and T. Rabczuk, "Mechanical oscillation of kinked silicon nanowires: A natural nanoscale spring," *Applied Physics Letters,* vol. 102, pp. 123104-1-123104-4, 2013.

[83] Y. Kogure, T. Kosugi, and M. Doyama, "Simulation for mechanical relaxation and interaction of point defects," *Materials Science and Engineering: A,* vol. 370, pp. 100-104, 2004.

[84] Y. Kogure, T. Kosugi, M. Doyama, and H. Kaburaki, "Simulation of mechanical response of point defects in copper," *Materials Science and Engineering: A,* vol. 442, pp. 71-74, 2006.

[85] K. Kunal and N. R. Aluru, "Intrinsic dissipation in a nano-mechanical resonator," *Journal of Applied Physics,* vol. 116, pp. 094304-1-094304-11, 2014.

[86] J.-W. Jiang, H. S. Park, and T. Rabczuk, "MoS 2 nanoresonators: intrinsically better than graphene?," *Nanoscale,* vol. 6, pp. 3618-3625, 2014.

[87] J.-W. Jiang, H. S. Park, and T. Rabczuk, "Preserving the Q-factors of ZnO nanoresonators via polar surface reconstruction," *Nanotechnology,* vol. 24, pp. 405705-1-405705-8, 2013.

[88] J. Tersoff, "Empirical interatomic potential for silicon with improved elastic properties," *Physical Review B,* vol. 38, pp. 9902-9905, 1988.

[89] H. Koh, J. J. Cannon, T. Shiga, J. Shiomi, S. Chiashi, and S. Maruyama, "Thermally induced nonlinear vibration of single-walled carbon nanotubes," *Physical Review B,* vol. 92, pp. 024306-1-024306-10, 2015.

[90] D. Midtvedt, A. Croy, A. Isacsson, Z. Qi, and H. S. Park, "Fermi-pasta-ulam physics with nanomechanical graphene resonators: intrinsic relaxation and thermalization from flexural mode coupling," *Physical Review Letters,* vol. 112, pp. 145503-1-145503-5, 2014.

[91] J.-Y. Lee and A. Seshia, "5.4-MHz single-crystal silicon wine glass mode disk resonator with quality factor of 2 million," *Sensors and Actuators A: Physical,* vol. 156, pp. 28-35, 2009.

[92] D. Weinstein and S. Bhave, "Internal dielectric transduction of a 4.5 GHz silicon bar resonator," in *Electron Devices Meeting. IEDM. IEEE International*, pp. 415-418, 2007.

[93] R. O. Pohl, X. Liu, and E. Thompson, "Low-temperature thermal conductivity and acoustic attenuation in amorphous solids," Reviews of Modern Physics, vol. 74, pp. 991-1013, 2002.

[94] K. Y. Yasumura, T. D. Stowe, E. M. Chow, T. Pfafman, T. W. Kenny, B. C. Stipe, and D. Rugar, "Quality factors in micron-and submicron-thick cantilevers," *Journal of Microelectromechanical Systems,* vol. 9, pp. 117-125, 2000.

[95] C. Zener, "Internal friction in solids. I. Theory of internal friction in reeds," Physical review, vol. 52, pp. 230-235, 1937.

[96] C. Zener, "Internal friction in solids II. General theory of thermoelastic internal friction," Physical Review, vol. 53, pp. 90-99, 1938.

[97] V. B. Braginsky, V. P. Mitrofanov, V. I. Panov, and R. Krotkov, "Systems with Small Dissipation," *American Journal of Physics,* vol. 55, pp. 1153-1154, 1987.

[98] N. W. Ashcroft and N. D. Mermin, *Solid State Physics*: Holt, Rinehart and Winston, 1976.

[99] J. W. Tucker, *Microwave ultrasonics in solid state physics. [By] J. W. Tucker and V. W. Rampton*. Amsterdam: North-Holland Pub. Co, 1972.

[100] R. Lifshitz, "Phonon-mediated dissipation in micro-and nano-mechanical systems," *Physica B: Condensed Matter,* vol. 316, pp. 397-399, 2002.

[101] V. Gantmakher and Y. Levinson, *Carrier scattering in metals and semiconductors*: Elsevier, 2012.

[102] A. Akhiezer, "On the absorption of sound in solids," *Journal of Physics,* vol. 1, pp. 277-287, 1939.

[103] T. Woodruff and H. Ehrenreich, "Absorption of sound in insulators," *Physical Review,* vol. 123, pp. 1553-1559, 1961.

[104] W. P. Mason and T. Bateman, "Ultrasonic-Wave Propagation in Pure Silicon and Germanium," *The Journal of the Acoustical Society of America,* vol. 36, pp. 644-652, 1964.

[105] H. Barrett and M. Holland, "Critique of current theories of akhieser damping in solids," *Physical Review B,* vol. 1, pp. 2538-2544, 1970.

[106] H. Bömmel and K. Dransfeld, "Excitation and attenuation of hypersonic waves in quartz," *Physical Review,* vol. 117, pp. 1245-1252, 1960.

[107] H. Maris, "Ultrasonic attenuation in dirty dielectric crystals," *Physical Review,* vol. 175, pp. 1077-1081, 1968.

[108] L. Landau and G. Rumer, "Absorption of sound in solids," *Physik. Z. Sowjetunion,* vol. 11, 1937.

[109] W. Phillips, "Tunneling states in amorphous solids," *Journal of Low Temperature Physics,* vol. 7, pp. 351-360, 1972.

[110] P. W. Anderson, B. Halperin, and C. M. Varma, "Anomalous low-temperature thermal properties of glasses and spin glasses," *Philosophical Magazine,* vol. 25, pp. 1-9, 1972.

[111] S. Hunklinger, "Phonons in amorphous materials," *Le Journal de Physique Colloques,* vol. 43, pp. C9-461-C9-474, 1982.

[112] P. Esquinazi, *Tunneling systems in amorphous and crystalline solids*: Springer Science & Business Media, 2013.

[113] P. Mohanty, D. A. Harrington, K. L. Ekinci, Y. T. Yang, M. J. Murphy, and M. L. Roukes, "Intrinsic dissipation in high-frequency micromechanical resonators," *Physical Review B,* vol. 66, pp. 085416-1-085416-15, 2002.

[114] C. Seoánez, F. Guinea, and A. H. Castro Neto, "Surface dissipation in nanoelectromechanical systems: Unified description with the standard tunneling model and effects of metallic electrodes," *Physical Review B,* vol. 77, pp. 125107-1-125107-14, 2008.

[115] J. Yang, T. Ono, and M. Esashi, "Surface effects and high quality factors in ultrathin single-crystal silicon cantilevers," *Applied Physics Letters,* vol. 77, pp. 3860-3862, 2000.

[116] Y. Wang, J. A. Henry, D. Sengupta, and M. A. Hines, "Methyl monolayers suppress mechanical energy dissipation in micromechanical silicon resonators," *Applied Physics Letters,* vol. 85, pp. 5736-5738, 2004.

[117] H. B. Callen and T. A. Welton, "Irreversibility and generalized noise," *Physical Review,* vol. 83, pp. 34-40, 1951.

[118] H. B. Callen and R. F. Greene, "On a theorem of irreversible thermodynamics," *Physical Review,* vol. 86, pp. 702-710, 1952.

[119] Y. Levin, "Internal thermal noise in the LIGO test masses: A direct approach," *Physical Review D,* vol. 57, pp. 659-663, 1998.

[120] J. E. Sader, B. D. Hughes, J. A. Sanelli, and E. J. Bieske, "Effect of multiplicative noise on least-squares parameter estimation with applications to the atomic force microscope," *Review of Scientific Instruments,* vol. 83, pp. 055106-1-055106-6, 2012.

[121] I. Kovacic and M. J. Brennan, *The Duffing equation: nonlinear oscillators and their behaviour*: John Wiley & Sons, 2011.

[122] D. Antonio, D. H. Zanette, and D. López, "Frequency stabilization in nonlinear micromechanical oscillators," *Nature Communications,* vol. 3, pp. 806-1-806-6, 2012.

[123] S. Plimpton, “Fast parallel algorithms for short-range molecular dynamics,” Journal of Computational Physics, vol. 117, pp. 1-19, 1995.

[124] C. W. Gear, *Numerical initial value problems in ordinary differential equations*: Prentice Hall PTR, 1971.

[125] R. W. Hockney, "POTENTIAL CALCULATION AND SOME APPLICATIONS," Langley Research Center, Hampton, Va.1970.

[126] L. Verlet, "Computer" experiments" on classical fluids. I. Thermodynamical properties of Lennard-Jones molecules," *Physical Review,* vol. 159, pp. 98-103, 1967.

[127] M. P. Allen and D. J. Tildesley, *Computer simulation of liquids*: Oxford university press, 1989.

[128] D. W. Brenner, O. A. Shenderova, J. A. Harrison, S. J. Stuart, B. Ni, and S. B. Sinnott, "A second-generation reactive empirical bond order (REBO) potential energy expression for hydrocarbons," *Journal of Physics: Condensed Matter,* vol. 14, pp. 783-802, 2002.

[129] K. Laasonen, A. Pasquarello, R. Car, C. Lee, and D. Vanderbilt, "Car-Parrinello molecular dynamics with Vanderbilt ultrasoft pseudopotentials," *Physical Review B,* vol. 47, pp. 10142-10153, 1993.

[130] J. Lennard-Jones, "On the forces between atoms and ions," *Proceedings of the Royal Society of London. Series A, Containing Papers of a Mathematical and Physical Character,* pp. 584-597, 1925.

[131] P. M. Morse, "Diatomic molecules according to the wave mechanics. II. vibrational levels," *Physical Review,* vol. 34, pp. 57-64, 1929.

[132] S. Foiles, M. Baskes, and M. Daw, "Embedded-atom-method functions for the fcc metals Cu, Ag, Au, Ni, Pd, Pt, and their alloys," *Physical Review B,* vol. 33, pp. 7983-7991, 1986.

[133] F. Ercolessi, M. Parrinello, and E. Tosatti, "Simulation of gold in the glue model," *Philosophical magazine A,* vol. 58, pp. 213-226, 1988.

[134] J. E. Angelo, N. R. Moody, and M. I. Baskes, "Trapping of hydrogen to lattice defects in nickel," *Modelling and Simulation in Materials Science and Engineering,* vol. 3, pp. 289-307, 1995.

[135] F. H. Stillinger and T. A. Weber, "Computer simulation of local order in condensed phases of silicon," *Physical Review B,* vol. 31, pp. 5262-5271, 1985.

[136] H. C. Andersen, "Molecular dynamics simulations at constant pressure and/or temperature," *The Journal of chemical physics,* vol. 72, pp. 2384-2393, 1980.

[137] H. Tanaka, K. Nakanishi, and N. Watanabe, "Constant temperature molecular dynamics calculation on Lennard-Jones fluid and its application to watera)," *The Journal of Chemical Physics,* vol. 78, pp. 2626-2634, 1983.

[138] S. Nosé, "A unified formulation of the constant temperature molecular dynamics methods," *The Journal of chemical physics,* vol. 81, pp. 511-519, 1984.

[139] F. Douarche, S. Joubaud, N. B. Garnier, A. Petrosyan, and S. Ciliberto, "Work fluctuation theorems for harmonic oscillators," *Physical Review Letters,* vol. 97, pp. 140603-1-140603-5, 2006.

[140] F. J. Harris, "On the use of windows for harmonic analysis with the discrete Fourier transform." *Proceedings of the IEEE*, vol. 66(1), pp. 51-83, 1978.

[141] J. J. Moré, "The Levenberg-Marquardt algorithm: implementation and theory," in *Numerical analysis*, ed: Springer, pp. 105-116, 1978.

[142] Q. Yu and P. Clancy, "Molecular dynamics simulation of the surface reconstruction and strain relief in Si1-xGex/Si(100) heterostructures," *Modelling and Simulation in Materials Science and Engineering,* vol. 2, pp. 829-844, 1994.

[143] X. Li, T. Ono, Y. Wang, and M. Esashi, "Ultrathin single-crystalline-silicon cantilever resonators: Fabrication technology and significant specimen size effect on Young's modulus," *Applied Physics Letters,* vol. 83, pp. 3081-3083, 2003.

[144] L. J. Porter, J. F. Justo, and S. Yip, "The importance of Grüneisen parameters in developing interatomic potentials," *Journal of Applied Physics,* vol. 82, pp. 5378-5381, 1997.

[145] J. V. Goicochea, M. Madrid, and C. Amon, "Thermal properties for bulk silicon based on the determination of relaxation times using molecular dynamics," *Journal of Heat Transfer,* vol. 132, pp. 1-11, 2010.

[146] D. P. Sellan, E. S. Landry, J. E. Turney, A. J. H. McGaughey, and C. H. Amon, "Size effects in molecular dynamics thermal conductivity predictions," *Physical Review B - Condensed Matter and Materials Physics,* vol. 81, pp. 214305-1-214305-10, 2010.

[147] S. G. Volz and G. Chen, "Molecular-dynamics simulation of thermal conductivity of silicon crystals," *Physical Review B,* vol. 61, pp. 2651-2656, 2000.

[148] S. Ryu and W. Cai, "Comparison of thermal properties predicted by interatomic potential models," *Modelling and Simulation in Materials Science and Engineering,* vol. 16, pp. 085005-1-085005-12, 2008.

[149] J. Marx and J. Sivertsen, "Temperature dependence of the elastic moduli and internal friction of silica and glass," *Journal of Applied Physics,* vol. 24, pp. 81-87, 1953.

[150] H. McSkimin, "Measurement of elastic constants at low temperatures by means of ultrasonic waves–data for silicon and germanium single crystals, and for fused silica," *Journal of Applied Physics,* vol. 24, pp. 988-997, 1953.

[151] O. Anderson and H. Bömmel, "Ultrasonic absorption in fused silica at low temperatures and high frequencies," *Journal of the American Ceramic Society,* vol. 38, pp. 125-131, 1955.

[152] X. Liu, B. E. White Jr, R. O. Pohl, E. Iwanizcko, K. M. Jones, A. H. Mahan, B. N. Nelson, R. S. Crandall and S. Veprek, "Amorphous solid without low energy excitations," *Physical Review Letters,* vol. 78, pp. 4418-4421, 1997.

[153] X. Liu, C. L. Spiel, R. D. Merithew, R. O. Pohl, B. P. Nelson, Q. Wang and R. S. Crandall, "Internal friction of amorphous and nanocrystalline silicon at low temperatures," *Materials Science and Engineering: A,* vol. 442, pp. 307-313, 2006.

[154] K. Gilroy and W. Phillips, "An asymmetric double-well potential model for structural relaxation processes in amorphous materials," *Philosophical Magazine B,* vol. 43, pp. 735-746, 1981.

[155] X. Liu and R. Pohl, "Low-energy excitations in amorphous films of silicon and germanium," *Physical Review B,* vol. 58, pp. 9067-9081, 1998.

[156] T. Zhu, H. J. Maris, and J. Tauc, "Attenuation of longitudinal-acoustic phonons in amorphous SiO 2 at frequencies up to 440 GHz," *Physical Review B,* vol. 44, pp. 4281-4289, 1991.

[157] D. Hondongwa, B. Daly, T. Norris, B. Yan, J. Yang, and S. Guha, "Ultrasonic attenuation in amorphous silicon at 50 and 100 GHz," *Physical Review B,* vol. 83, pp. 121303-1-121303-4, 2011.

[158] R. Vacher, E. Courtens, and M. Foret, "Anharmonic versus relaxational sound damping in glasses. II. Vitreous silica," *Physical Review B,* vol. 72, pp. 214205-1-214205-11, 2005.

[159] F. Wooten, K. Winer, and D. Weaire, "Computer Generation of Structural Models of Amorphous Si and Ge," *Physical Review Letters,* vol. 54, pp. 1392-1395, 1985.

[160] B. R. Djordjević, M. F. Thorpe, and F. Wooten, "Computer model of tetrahedral amorphous diamond," *Physical Review B,* vol. 52, pp. 5685-5689, 1995.

[161] G. T. Barkema and N. Mousseau, "Event-Based Relaxation of Continuous Disordered Systems," *Physical Review Letters,* vol. 77, pp. 4358-4361, 1996.

[162] R. L. C. Vink, G. T. Barkema, W. F. van der Weg, and N. Mousseau, "Fitting the Stillinger–Weber potential to amorphous silicon," *Journal of Non-Crystalline Solids,* vol. 282, pp. 248-255, 2001.

[163] W. D. Luedtke and U. Landman, "Preparation, structure, dynamics, and energetics of amorphous silicon: A molecular-dynamics study," *Physical Review B,* vol. 40, pp. 1164-1174, 1989.

[164] K. Vollmayr, W. Kob, and K. Binder, "Cooling-rate effects in amorphous silica: A computer-simulation study," *Physical Review B,* vol. 54, pp. 15808-15827, 1996.

[165] A. S. Argon and M. J. Demkowicz, "Atomistic simulation and analysis of plasticity in amorphous silicon," *Philosophical Magazine,* vol. 86, pp. 4153-4172, 2006.

[166] W. H. Zachariasen, "The atomic arrangement in glass," *Journal of the American Chemical Society,* vol. 54, pp. 3841-3851, 1932.

[167] M. J. Demkowicz, *Mechanisms of Plastic Deformation in Amorphous Silicon by Atomistic Simulation Using the Stillinger-Weber Potential*: Massachusetts Institute of Technology, Department of Mechanical Engineering, 2005.

[168] N. Mousseau and G. T. Barkema, "Fast bond-transposition algorithms for generating covalent amorphous structures," *Current Opinion in Solid State and Materials Science,* vol. 5, pp. 497-502, 2001.

[169] C. L. Allred, X. Yuan, M. Z. Bazant, and L. W. Hobbs, "Elastic constants of defected and amorphous silicon with the environment-dependent interatomic potential," *Physical Review B - Condensed Matter and Materials Physics,* vol. 70, pp. 134113-1-134113-13, 2004.

[170] G. Lucas, M. Bertolus, and L. Pizzagalli, "An environment-dependent interatomic potential for silicon carbide: calculation of bulk properties, high-pressure phases, point and extended defects, and amorphous structures," *Journal of Physics: Condensed Matter,* vol. 22, pp. 035802-1-035802-13, 2010.

[171] M. Z. Bazant, E. Kaxiras, and J. F. Justo, "Environment-dependent interatomic potential for bulk silicon," *Physical Review B,* vol. 56, pp. 8542-8552, 1997.

[172] B. Philippe and M. Normand, "Liquid–liquid phase transition in Stillinger–Weber silicon," *Journal of Physics: Condensed Matter,* vol. 17, pp. 2269-2279, 2005.

[173] S. Sastry and C. Austen Angell, "Liquid-liquid phase transition in supercooled silicon," *Nat Mater,* vol. 2, pp. 739-743, 2003.

[174] R. Biswas, G. S. Grest, and C. M. Soukoulis, "Generation of amorphous-silicon structures with use of molecular-dynamics simulations," *Physical Review B,* vol. 36, pp. 7437-7441, 1987.

[175] S. J. Cook and P. Clancy, "Comparison of semi-empirical potential functions for silicon and germanium," *Physical Review B,* vol. 47, pp. 7686-7699, 1993.

[176] J. M. Holender and G. J. Morgan, "Generation of a large structure (105atoms) of amorphous Si using molecular dynamics," *Journal of Physics: Condensed Matter,* vol. 3, pp. 7241-7254, 1991.

[177] D. Tielbürger, R. Merz, R. Ehrenfels, and S. Hunklinger, "Thermally activated relaxation processes in vitreous silica: An investigation by Brillouin scattering at high pressures," *Physical Review B,* vol. 45, pp. 2750-2760, 1992.

[178] D. C. Rapaport, *The Art of Molecular Dynamics Simulation*: Cambridge University Press., 2004.

[179] W. Humphrey, A. Dalke, and K. Schulten, "VMD: visual molecular dynamics," *Journal of Molecular Graphics,* vol. 14, pp. 33-38, 1996.

[180] M. Ishimaru, S. Munetoh, and T. Motooka, "Generation of amorphous silicon structures by rapid quenching: A molecular-dynamics study," *Physical Review B,* vol. 56, pp. 15133-15138, 1997.

[181] P. J. Steinhardt, D. R. Nelson, and M. Ronchetti, "Bond-orientational order in liquids and glasses," *Physical Review B,* vol. 28, pp. 784-805, 1983.

[182] U. Gasser, F. Ziese, and G. Maret, "Characterization of local structures with bond-order parameters and graphs of the nearest neighbors, a comparison," *The European Physical Journal Special Topics,* vol. 223, pp. 455-467, 2014.

[183] J. Song and D. J. Srolovitz, "Atomistic simulation of multicycle asperity contact," *Acta Materialia,* vol. 55, pp. 4759-4768, 2007.

[184] K. Zhang, H. Li, and Y. Y. Jiang, "Liquid-liquid phase transition in quasi-two-dimensional supercooled silicon," *Physical Chemistry Chemical Physics,* vol. 16, pp. 18023-18028, 2014.

[185] D. Tielbürger, R. Merz, R. Ehrenfels, and S. Hunklinger, "Thermally activated relaxation processes in vitreous silica: An investigation by Brillouin scattering at high pressures," *Physical Review B,* vol. 45, pp. 2750-2760, 1992.

[186] R. Vacher, J. Pelous, F. Plicque, and A. Zarembowitch, "Ultrasonic and Brillouin scattering study of the elastic properties of vitreous silica between 10 and 300 K," *Journal of Non-Crystalline Solids,* vol. 45, pp. 397-410, 1981.

[187] J. Fabian and P. B. Allen, "Theory of sound attenuation in glasses: the role of thermal vibrations," *Physical Review Letters,* vol. 82, pp. 1478-1481, 1999.

[188] J. Fabian and P. B. Allen, "Thermal expansion and Grüneisen parameters of amorphous silicon: A realistic model calculation," *Physical Review Letters,* vol. 79, pp. 1885-1888, 1997.

[189] X. Liu, D. R. Queen, T. H. Metcalf, J. E. Karel, and F. Hellman, "Hydrogen-free amorphous silicon with no tunneling states," *Physical Review Letters,* vol. 113, pp. 025503-1-025503-5, 2014.

[190] K. Bhatia, M. Haumeder, and S. Hunklinger, "Ultrasonic properties of amorphous SiH_x-films," *Solid State Communications,* vol. 37, pp. 943-948, 1981.

[191] X. Wei, L. Ruihong, and L. Shuang, "Resonance and bifurcation in a nonlinear Duffing system with cubic coupled terms," *Nonlinear Dynamics,* vol. 46, pp. 211-221, 2006.

[192] I. Kozinsky, "Nonlinear nanoelectromechanical systems," PhD thesis, Department of Physics, California Institute of Technology, 2007.

[193] H. C. Postma, I. Kozinsky, A. Husain, and M. Roukes, "Dynamic range of nanotube-and nanowire-based electromechanical systems," *Applied Physics Letters,* vol. 86, pp. 223105-1-223105-3, 2005.